

# Thermal Energy Harvesting based on Magnetic Shape Memory Alloys

zur Erlangung des akademischen Grades

**Doktor der Ingenieurwissenschaften**

der Fakultät Maschinenbau  
Karlsruher Institut für Technologie (KIT)

genehmigte

**Dissertation**

von

Dipl.-Ing. Marcel Gültig

Tag der mündlichen Prüfung: 12.05.2016

Hauptreferent: Prof. Dr. Manfred Kohl  
Korreferent: Prof. Dr. Chris Eberl

Karlsruher Institut für Technologie (KIT)  
Institut für Mikrostrukturtechnik  
H.-v.-Helmholtz Platz 1  
76344 Eggenstein-Leopoldshafen



This document is licensed under the Creative Commons Attribution 3.0 DE License  
(CC BY 3.0 DE): <http://creativecommons.org/licenses/by/3.0/de/>

For my wife and my parents.

# Preface

Working in the field of shape memory alloys and energy harvesting was a great pleasure for me. I primarily want to thank my supervisor Professor Dr. Manfred Kohl for introducing me to these topics. I am thankful for his ongoing support and guidance in my research, providing me with plenty of opportunities to learn and to increase my knowledge. I thank Professor Dr. Chris Eberl for being co-supervisor and taking the time to review my work.

Special thanks go to my colleague Hinnerk Oßmer, who, beside supporting me in DSC-Measurements and material characterization, always lend an ear to me if interesting topics needed to be discussed. For physical and mathematical discussions concerning simulations and the theory behind my work I want to thank Dr. Frank Wendler. For the last two years he also enriched the corridor atmosphere by introducing open doors. I want to thank Franziska Lambrecht for interesting discussions, proof-reading and improving the working atmosphere in our corridor. Many thanks also go to Christian Lay for proof-reading parts of my thesis. I also want to thank my colleagues of FuE1-SMD: Ruizhi Yin, Viktor Pinneker, Randy Fechner, Christof Megnin, Dr. Berthold Krevet, Mario Schmitt and Julian Hartbaum for making research and working a thoroughly enjoyable experience.

Special thanks go to my collaborators at Tohoku University in Japan for providing me with samples of magnetic shape memory alloys and thermomagnetic measurements. Without the material of exceptional quality, this work would not have been successful. Therefore, I want to thank Professor Takagi for supporting the collaborative work as leader of IFS, Professor Miki for discussions and supervision of student work, and Dr. Ohtsuka for fabrication of magnetic SMA films, discussions, and supervision of students. I also want to thank the students Koki Tsuchiya and Eijiro Abe for fabricating the magnetic SMA material and visiting Germany, supporting my research work.

For performing laser cutting of magnetic SMA films, I want to express my gratitude to Heino Besser from IAM (KIT). I thank Frieder Märkle for instructions in the laser handling for performing laser-heating experiments. Further proof-reading was performed by my friends Christoph and Uli - thank you for your time and effort.

Making lunch break a special pleasure I want to thank everyone who joined playing "Kicker" after lunch! I am also thankful to all other IMT staff, helping me through paperwork and all kinds of obstacles. Also my fellow PhD students made working at IMT a really interesting and enjoyable time.

Finally I want to thank my dear wife Franziska, my parents Kornelia and Werner, and my family for their ongoing support. You provide a quiet place I can always return to.

# Abstract

Thermal energy harvesting technologies like thermoelectrics or heat engines suffer from a number of difficulties on miniaturization, which is required for being competitive with small batteries. While heat engines cannot be miniaturized below a certain size limit, thermoelectric generators can be fabricated also as MEMS structures. However, at small size the demand for heat sinking beyond natural convection increases or large heat sinks become necessary. Also the power density, the most important measure for energy harvesting technologies, is limited. Thermomagnetic energy harvesting opens up a new approach to overcome the limitations of miniaturized thermal energy harvesting systems. While having a relatively low efficiency, the thermomagnetic conversion principle shows a large power density upon miniaturization. However, only little research on thermomagnetic energy harvesting at miniature scale has been performed and no competitive electrical output has been reported until now.

This work presents a series of novel thermomagnetic energy harvesting principles as well as developments of corresponding layouts and demonstrators based on magnetic shape memory alloys (SMA) belonging to the group of Heusler alloys. Sputter deposited ferromagnetic Ni-Mn-Ga and Ni-Co-Mn-Ga films, and metamagnetic Ni-Co-Mn-In films are characterized regarding their mechanical, thermal, and magnetic properties in order to identify suitable materials. Large magnetization changes of up to 3.1 and 2.3  $\text{emu}\cdot(\text{g K})^{-1}$  are found at the first order phase transformation and ferromagnetic transition, respectively. These films are used to develop and investigate energy harvesting demonstrators, based on self-actuated miniature cantilevers. A pick-up coil converts the mechanical oscillation to electricity according to Faraday's law.

Making use of an external pick-up coil and frequency up-conversion, first generation energy harvesting demonstrators achieve power densities of  $0.8 \mu\text{W}\cdot\text{cm}^{-3}$  at thermal frequencies below 6 Hz. By introducing micro-coils, fabricated from 15  $\mu\text{m}$  copper wire and attached to the cantilever tip, metamagnetic SMA energy harvesting with power densities of up to  $1.6 \mu\text{W}\cdot\text{cm}^{-3}$  is achieved. By reducing the thickness of magnetic SMA material at the cantilever tip, thermal actuation frequencies of above 80 Hz are reached. The matching of heat transfer times and eigenfrequency of the cantilever is identified as a key to boost the power density up to  $3 \text{mW}\cdot\text{cm}^{-3}$ . Further optimization in magnetic design and integration of the heat source to the external permanent magnet leads to considerable improvement in power density, reaching above  $100 \text{mW}\cdot\text{cm}^{-3}$  at an average power output of 2.34  $\mu\text{W}$ . This is an improvement of above 5 orders of magnitude compared to the first demonstrator. Thus, thermomagnetic energy harvesting competes for the first time with state-of-the-art thermoelectrics.

# Kurzfassung

Um mit Batterien konkurrieren zu können, müssen thermische Energy-Harvesting-Technologien wie z.B. Thermoelektrik oder Wärmekraftmaschinen verkleinert werden, was jedoch eine Reihe von Problemen mit sich bringt. Eine Verkleinerung von Wärmekraftmaschinen ist nur bis zu einer gewissen Untergrenze möglich, während thermoelektrische Generatoren auch als MEMS-Strukturen hergestellt werden. Diese Miniaturisierung hat jedoch zur Folge, dass ein Bedarf an Kühlung jenseits natürlicher Konvektion besteht, bzw. große Kühlkörper eingesetzt werden müssen, um eine ausreichend große Temperaturdifferenz zu gewährleisten. Auch die Leistungsdichte, die wichtigste Kennzahl für Energy-Harvesting-Technologien, ist begrenzt. Thermomagnetisches Energy-Harvesting bietet einen neuen Ansatz, um die Einschränkungen miniaturisierter thermische Energy-Harvesting-Systeme zu überwinden. Obwohl es eine relativ niedrige Effizienz aufweist, zeigt das thermomagnetische Prinzip bei Miniaturisierung eine hohe Leistungsdichte. Bislang wurde jedoch erst vergleichsweise wenig zum thermomagnetischen Energy-Harvesting auf der Miniaturskala geforscht und die berichteten elektrischen Ausgangsleistungen sind sehr gering.

Diese Arbeit präsentiert eine Reihe neuartiger thermomagnetischer Energy-Harvesting-Prinzipien sowie die Entwicklung entsprechender Entwürfe und Demonstratoren basierend auf magnetischen Formgedächtnislegierungen (FGL), die zur Gruppe der Heusler-Legierungen zählen. Mittels Kathodenerstäubung hergestellte ferromagnetische NiMnGa und NiCoMnGa-Schichten sowie metamagnetische NiCoMnIn-Schichten werden bezüglich ihrer mechanischen, thermischen und magnetischen Eigenschaften charakterisiert, um geeignete Materialien zu identifizieren. Große Magnetisierungsänderungen von bis zu  $3,1$  und  $2,3 \text{ emu} \cdot (\text{g K})^{-1}$  werden jeweils für die Phasenumwandlung erster Ordnung sowie die ferromagnetische Umwandlung gemessen. Diese Schichten werden genutzt, um Energy-Harvesting-Demonstratoren zu entwickeln und zu untersuchen, die auf sich selbst anregenden Miniatur-Biegebalken basieren. Eine Spule wandelt die mechanische Oszillationsbewegung in einen elektrischen Strom um.

Eine erste Generation der Energy-Harvesting-Demonstratoren, die auf eine externe Spule setzt und Frequenz-"Upconversion" nutzt, zeigt eine mittlere Leistungsdichte von etwa  $0,8 \text{ } \mu\text{W} \cdot \text{cm}^{-3}$  bei niedrigen Frequenzen für den thermischen Zyklus von unter  $6 \text{ Hz}$ . Mikrospulen, die mit  $15 \text{ } \mu\text{m}$  dickem Kupferdraht hergestellt und auf der Biegebalkenspitze angebracht werden, ermöglichen es, metamagnetische FGL-basierte Demonstratoren mit Leistungsdichten von bis zu  $1,6 \text{ } \mu\text{W} \cdot \text{cm}^{-3}$  herzustellen. Eine Reduzierung des magnetischen Materials auf der Balkenspitze führt zu thermischen Aktorzyklen von über  $80 \text{ Hz}$ . Hierbei wird die Übereinstimmung thermischer Übergangszeiten und der

mechanischen Eigenfrequenz als Schlüsselkriterium identifiziert, um die Leistungsdichte auf bis zu  $3 \text{ mW}\cdot\text{cm}^{-3}$  zu steigern. Eine weitere Optimierung des Magnetdesigns und die Kombination von Wärmequelle und Magnet führen zu einer weiteren erheblichen Steigerung der Leistungsdichte auf mehr als  $100 \text{ mW}\cdot\text{cm}^{-3}$  bei einer mittleren Ausgangsleistung von etwa  $2,34 \text{ }\mu\text{W}$ . Dies ist eine Verbesserung um mehr als fünf Größenordnungen gegenüber den ersten Demonstratoren. Mit diesem Ergebnis konkurrieren thermomagnetische Generatoren zum ersten Mal mit modernen miniaturisierten thermoelektrischen Generatoren.

# Publications

## Journal Papers

**M. Gueltig**, H. Ossmer, M. Ohtsuka, H. Miki, K. Tsuchiya, T. Takagi, and M. Kohl, "High Frequency Thermal Energy Harvesting Using Magnetic Shape Memory Films" *Adv. Energy Mater.*, vol. 4, no. 17, p. 1400751, **2014**.

**M. Gueltig**, H. Ossmer, M. Ohtsuka, H. Miki, K. Tsuchiya, T. Takagi, and M. Kohl, "Thermomagnetic Actuation by Low Hysteresis Metamagnetic Ni-Co-Mn-In Films" *Materials Today: Proceedings*, vol. 2, pp. S883–S886, **2015**.

**M. Gueltig**, F. Wendler, H. Ossmer, M. Ohtsuka, H. Miki, T. Takagi, and M. Kohl, "High Performance Thermomagnetic Generation based on Heusler Alloy Films" *Adv. Energy Mater.* accepted, **2016**.

**M. Gueltig**, E. Abe, H. Ossmer, H. Miki, M. Ohtsuka, T. Takagi, and M. Kohl, "Energy Harvesting with Metamagnetic Shape Memory Alloy Plates" *in Preparation*

V. Pinneker, **M. Gueltig**, A. Sozinov, and M. Kohl, "Single phase boundary actuation of a ferromagnetic shape memory foil" *Acta Mater.*, vol. 64, pp. 179–187, **2014**.

M. Kohl, **M. Gueltig**, V. Pinneker, R. Yin, F. Wendler, and B. Krevet, "Magnetic Shape Memory Microactuators" *Micromachines*, vol. 5, no. 4, pp. 1135–1160, **2014**.

H. Ossmer, F. Lambrecht, **M. Gültig**, C. Chluba, E. Quandt, and M. Kohl, "Evolution of temperature profiles in TiNi films for elastocaloric cooling" *Acta Mater.*, vol. 81, pp. 9–20, **2014**.

H. Ossmer, C. Chluba, **M. Gueltig**, E. Quandt, and M. Kohl, "Local Evolution of the Elastocaloric Effect in TiNi-Based Films" *Shap. Mem. Superelasticity*, vol. 1, no. 2, pp. 142–152, **2015**.

H. Ossmer, F. Wendler, **M. Gueltig**, F. Lambrecht, S. Miyazaki, M. Kohl, "Energy-efficient miniature-scale heat pumping based on shape memory alloys" *Smart Mater. Struct.*, vol. 25, 085037, **2016**

## Conference Contributions

**M. Gueltig**, B. Haefner, M. Ohtsuka, and M. Kohl, "Thermal energy harvesting based on ferromagnetic shape memory alloy microactuation" presented at the Transducers & Eurosensors XXVII, Barcelona, Spain, pp. 2803–2806, **2013**.

**M. Gueltig**, M. Ohtsuka, H. Miki, T. Takagi, and M. Kohl, "Development of Energy Harvesting Devices based on Magnetic Shape Memory Alloy Thin Films" Proc. Eleventh International Conference on Flow Dynamics (ICFD 2014), 280-281, Sendai, Japan, **2014**.

**M. Gueltig**, H. Miki, M. Ohtsuka, T. Takagi, and M. Kohl, "Thermal energy harvesting based on metamagnetic shape memory alloys" Proc. Int Conf. on Energy, Science and Technology EST'15, Karlsruhe, Germany, **2015**.

**M. Gueltig**, M. Ohtsuka, H. Miki, T. Takagi, and M. Kohl, "Thermal energy harvesting by high frequency actuation of magnetic shape memory alloy films" presented at the Transducers XVIII, Anchorage, USA, pp. 718–721, **2015**.

**M. Gültig**, M. Ohtsuka, H. Miki, T. Takagi und M. Kohl, "Thermisches Energy Harvesting mit magnetischen Formgedächtnis-Dünnschichten" Proc. Mikrosystemtechnik-Kongress'15, Karlsruhe, Germany, **2015**.

C. Megnin, H. Ossmer, **M. Gültig**, T. Hanemann, M. Kohl, "Formgedächtnis-Mikroventile für Fluidsysteme" Proc. Mikrosystemtechnik-Kongress'15, Karlsruhe, Germany, **2015**.

# Table of Contents

<b>1. Introduction</b> .....	<b>1</b>
1.1. Energy Harvesting .....	1
1.2. Smart Materials .....	1
1.3. Microsystems and Thin Films.....	2
1.4. Goal of this Work.....	3
<b>2. Basics and Fabrication</b> .....	<b>5</b>
2.1. Shape Memory Alloys.....	5
2.1.1 Shape Memory Effect (SME) .....	5
2.1.1.1 One-Way Effect .....	6
2.1.1.2 Two-Way Effect .....	7
2.1.1.3 Superelasticity .....	7
2.1.2 Ferromagnetic Shape Memory Alloys (FSMA) .....	8
2.1.3 Metamagnetic Shape Memory Alloys (MSMA).....	9
2.2. Pyroelectricity .....	9
2.3. Electromagnetism - Faraday's Law.....	10
2.4. Measurement Methods.....	11
2.4.1 Differential Scanning Calorimetry .....	11
2.4.2 Electrical Resistance Measurement.....	12
2.4.3 Tensile Measurements .....	13
2.4.4 Elastometer .....	14
2.4.5 Current Measurement.....	14
2.4.6 SQUID .....	14
2.4.7 X-Ray Diffraction Method (XRD) .....	15
2.4.8 Infrared Thermography .....	15
2.4.9 Image Tracking.....	15
2.4.10 Laser distance sensor.....	16
2.5. Fabrication .....	16
2.5.1 Magnetron Sputtering.....	16
2.5.2 Heat treatment .....	17
2.5.3 Lithography and Wet Etching.....	17
2.5.4 Laser Cutting.....	18

2.5.5 Microcoil Fabrication.....	19
<b>3. State of the Art of Thermal Energy Harvesting.....</b>	<b>21</b>
3.1. Kinetic Energy Harvesting .....	21
3.2. Thermal Energy Harvesting .....	23
3.2.1 Thermoelectric Generators .....	24
3.2.2 Pyroelectric Energy Harvesting .....	26
3.2.3 Other Thermal Energy Harvesting .....	26
3.3. Thermomagnetic Actuation and Energy Harvesting.....	26
3.3.1 Thermomagnetic Motors based on Ferromagnetic Transitions.....	27
3.3.2 Energy Harvesting by 1st Order Phase Transformation .....	28
3.3.3 Magnetic Shape Memory Actuation .....	29
<b>4. Material Characterization .....</b>	<b>31</b>
4.1. Ferromagnetic Shape Memory Alloys.....	31
4.1.1 Mechanical Characterization .....	32
4.1.2 Thermal Characterization.....	32
4.1.3 Thermo-Magnetic Characterization.....	34
4.1.4 Summary of FSMA Material Characterization .....	36
4.2. Metamagnetic Shape Memory Alloys.....	36
4.2.1 Mechanical Characterization.....	37
4.2.2 Thermal Characterization.....	37
4.2.3 Thermo-Magnetic Characterization.....	39
4.2.4 X-Ray Diffraction.....	41
4.2.5 Summary of MSMA Material Characterization .....	41
4.3. Influence of Heat Treatment on MSMA Films .....	42
<b>5. FSMA-based Energy Harvesting.....</b>	<b>45</b>
5.1. Basic Operation Principle of FSMA-based Energy Harvesting .....	45
5.2. FSMA-based Energy Harvesting using an External Pick-Up Coil .....	47
5.2.1 Operation Principle .....	47
5.2.2 Fabrication .....	47
5.2.3 Mechanical Characterization.....	48
5.2.4 Thermal Characterization.....	51
5.2.5 Electrical Output .....	52
5.2.6 Conclusions.....	54
5.3. FSMA-based Energy Harvesting using an Integrated Microcoil .....	55
5.3.1 Operation Principle .....	55

5.3.2 Fabrication .....	55
5.3.3 Mechanical Characterization .....	56
5.3.4 Thermal Characterization .....	58
5.3.5 Electrical Output .....	59
5.3.6 Energy Harvesting Array .....	61
5.3.7 Conclusions.....	62
5.4. FSMA-based Energy Harvesting using a Magnetic Heat Source .....	63
5.4.1 Operation Principle .....	63
5.4.2 Fabrication .....	63
5.4.3 Mechanical Characterization .....	64
5.4.4 Thermal Characterization .....	65
5.4.5 Electrical Output .....	66
5.4.6 Performance at Different Ambient Temperatures.....	67
5.4.7 Conclusion .....	68
<b>6. MSMA-based Energy Harvesting.....</b>	<b>69</b>
6.1. Basic Operation Principle of MSMA-based Energy Harvesting .....	69
6.2. MSMA-based Direct Energy Harvesting by Laser Heating.....	70
6.2.1 Operation Principle .....	70
6.2.2 Fabrication .....	71
6.2.3 Results .....	72
6.2.4 Conclusions.....	74
6.3. MSMA-based Direct Energy Harvesting by External Actuation .....	74
6.3.1 Operation Principle .....	74
6.3.2 Fabrication .....	74
6.3.3 Results .....	75
6.3.4 Conclusions.....	76
6.4. Self-Actuated MSMA-based Energy Harvesting.....	77
6.4.1 Operation Principle .....	77
6.4.2 Fabrication .....	77
6.4.3 Mechanical Characterization .....	78
6.4.4 Thermal Characterization .....	79
6.4.5 Electrical Output .....	80
6.4.6 Conclusions.....	81
6.5. Pyroelectric Energy Harvesting by MSMA-based Actuation .....	82
6.5.1 Operation Principle .....	82

6.5.2 Fabrication .....	82
6.5.3 Results .....	83
6.5.4 Conclusions.....	84
<b>7. Design Parameters and Theoretical Discussion .....</b>	<b>85</b>
7.1. Heat Transfer.....	85
7.2. Actuation Forces .....	87
7.3. Kinetic Energy and Resonance .....	89
7.4. Energy Conversion .....	91
7.5. Design Parameters .....	93
<b>8. Comparison and Discussion .....</b>	<b>95</b>
8.1. Comparison of Energy Harvesting Principles.....	95
8.2. Discussion.....	96
8.3. Comparison with Thermoelectrics.....	97
<b>9. Conclusion and Outlook.....</b>	<b>101</b>
9.1. Conclusion .....	101
9.2. Outlook .....	102
<b>10. Literature .....</b>	<b>105</b>
<b>11. Curriculum Vitae.....</b>	<b>114</b>



# 1. Introduction

## 1.1. Energy Harvesting

"Energy Harvesting" stands for the use of surrounding energy sources in order to harvest small amounts of energy and converting them to electricity. Possible energy sources can be vibrations, light, wind, and thermal gradients. This thesis addresses energy harvesting of temperature gradients, which can be found in a variety of places like a combustion engine, pipes and tanks with hot fluids in chemical or steel factories, radiators in private households, and more. Harvesting energy of these sources to generate small amounts of electricity is important to enable wireless sensor networks, as they are proposed for the internet of things [1, 2]. By avoiding batteries and thereby high maintenance costs, wireless sensor networks can be established in factories, civil structures, and in nature. The data obtained through these sensor networks, measuring, e.g. vibration, temperature, and humidity, enable the monitoring and understanding of complex systems. This leads to health monitoring of buildings [3], optimization of production parameters, better forecasts, and impact assessments.

Until now, research on thermal energy harvesting is focused mainly on thermoelectric energy conversion. However, thermoelectric generators (TEG) are limited in applicability because of their need for heat sinking beyond natural convection. Especially on miniaturization, the performance of TEG decreases strongly, making it necessary to look for alternatives. This work presents several novel thermomagnetic energy harvesting principles, based on using the intrinsic transducing capabilities of smart materials.

## 1.2. Smart Materials

The term "smart materials" describes materials that exhibit multifunctional properties, changing significantly when stimulated by an external (thermal, electric, magnetic, mechanical stress) field. A large group of smart materials are ferroic or even multiferroic materials, showing several ferroic properties such as ferroelectricity, ferromagnetism, or ferroelasticity. Multiferroic materials feature a coupling between primary order parameters as shown in Figure 1.1. By changing the magnetic field for instance, not only the magnetization of the material changes, but also the strain of the material can be controlled. These properties of multiferroic materials enable new and advanced actuation principles. Different from conventional actuators like electromagnetic motors, the multifunctional properties enable smart actuation, i.e. the "*Material is the Machine*" [4]. The setup of such actuators is very simple in comparison with conventional actuators, and therefore well suited for miniaturization. While it is very difficult to miniaturize the complexity of an electromagnetic motor, the fundamental mechanisms of multiferroic materials take place at the atom length scale, allowing down-scaling to the nano-regime.

Examples for couplings in multiferroics are the magnetic field induced reorientation (MIR) [5], the change of magnetization on external mechanical stress [6], or the change of temperature due to an external pressure or changing magnetic field [7, 8]. These couplings can be found in magnetic shape memory alloys, a part of the group of multiferroics. They show a strong coupling between thermal, magnetic, and mechanical properties. However, the couplings differ for each magnetic SMA material and depend strongly on the electronic and spin interactions on atomic scale. This can be influenced by tuning the chemical composition and microstructure of the alloys [9].

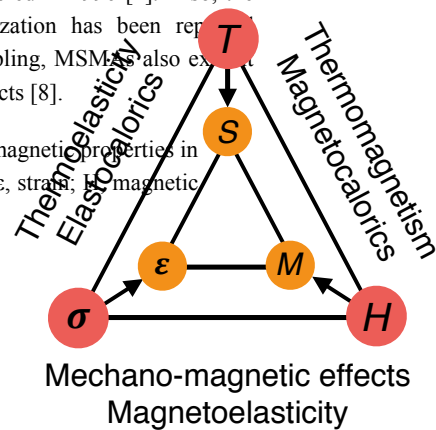


Figure 1.1: Coupling of thermal, magnetic, and mechanic properties in multiferroic materials.  $T$ , temperature;  $H$ , magnetic field;  $\sigma$ , stress;  $S$ , entropy;  $M$ , magnetization;  $\epsilon$ , strain.

### 1.3. Microsystems and Thin Films

In modern technology, miniaturization is an essential element for future development. It is driven by the desire for portability, light weight construction, decreasing costs, and integration density in novel high-tech products. While microelectronics have seen an extreme downsizing development over the last decades, this can also be registered for micro-electro-mechanical systems (MEMS). Silicon based inertial sensors and electrostatic mirror arrays are examples for MEMS in new mass-market applications as smartphones and projectors. Microsystems are essential for the development of such new product categories.

Thin films with transducing capability play an important role for microactuation because of limited actuation potential of silicon based MEMS devices like electrostatic or thermal microactuators. Especially shape memory alloy (SMA) based actuators like microvalves [10], microscanners [11], and microgrippers [12], benefit from the advantages of thin films. An overview of magnetic SMA microactuators is given in [13]. The high surface-to-volume ratio enables fast heat transfer and short actuation times. Thin films are easily structured using laser machining or MEMS processes like UV-lithography [14]. An easy assembly can also be realized, using a layer-based setup [15]. In order to fabricate thin films, physical vapor deposition methods as vacuum deposition or magnetron

sputtering are used. The fabrication mechanism of magnetic SMA thin films is described in detail in Chapter 2.5.1. However, the integration of SMA in MEMS technology is very challenging, as most silicon-processing steps are incompatible to SMA handling and vice versa. Therefore, most SMA actuators use packaging technologies to combine MEMS and SMA actuators.

#### 1.4. Goal of this Work

The goal of this work is the development of novel thermal energy harvesting devices based on magnetic SMA thin films. For this purpose, seven different magnetic SMA films are investigated and compared in detail, determining their mechanical, thermal, electrical, and magnetic properties. Choosing the best suited materials, concepts for ferromagnetic SMA (FSMA) and metamagnetic SMA (MSMA) based energy harvesting have to be developed. For each energy harvesting principle, the most important design parameters can be identified and first proof-of-principle demonstrator devices have to be build up. Based on the mechanical and electrical characterization of the demonstrators, the possibilities and the potential of using ferroic and multiferroic magnetic SMA thin films for energy harvesting are to be assessed. Finally, the results have to be compared to other miniature thermal energy harvesting technologies such as miniature thermoelectrics.



## 2. Basics and Fabrication

This chapter describes the most important basics of the materials used in this thesis as well as corresponding measurement and fabrication methods.

### 2.1. Shape Memory Alloys

As mentioned in Chapter 1.2, SMAs and magnetic SMAs are part of the ferroic material class, showing coupled physical properties. In this chapter, several coupling effects like the one-way and the magnetic shape memory effect are explained. Additionally, the ferromagnetic and metamagnetic SMAs are introduced and their main properties and differences are described.

#### 2.1.1 Shape Memory Effect (SME)

The shape memory effect (SME) was first discovered in the 1930s but interest remained low until the discovery of Ni-Ti. It was commercialized as Nitinol, in the 1960s [16], and shows remarkable properties like strains of up to 10%. Shape memory effects are observed not only in metal alloys, but also in polymers and ceramic materials. This description of the SME and its mechanism will only cover metal shape memory alloys.

The occurrence of the SME requires two solid phases, a low temperature phase, called martensite, and a high temperature parent phase, called austenite. The lattice structure of the austenite has a high symmetry and is, e.g., cubic, while the martensite lattice has a low symmetry with, e.g., tetragonal unit cells. In martensitic state the low symmetry unit cells arrange with different orientations, so called variants, forming twin boundaries in between. Generally, these twin boundaries may move easily, causing reorientation of the martensitic unit cells. Because of the cubic lattice structure of the austenite, only one variant and no twin boundaries exist, leading to just an elastic deformation below the yielding point. Reverse transformation to austenite from any combination of martensite variants results in the same variant and therefore only one shape exists in the high temperature state. The concept of different lattices and twin boundaries that form in martensite is shown in Figure 2.1. Starting from austenite, having cubic unit cells, self-accommodated martensite forms on cooling, which allows to retain the overall shape. On applying an external load to the SMA, the lattice can be easily deformed by reorientation of martensite unit cells and the mechanism of twin boundary motion. Depending on the lattice structure of the material, large deformations of up to 12% in Ni-Mn-Ga can be achieved by this effect [17]. On heating, the lattice transforms back to austenite, recovering the original shape, as just one variant and no twin boundaries exist in the high temperature phase.

Phase transformations take place at certain transformation temperatures, which are defined as martensite start and finish temperatures  $M_s$ ,  $M_f$ , and austenite start and finish temperatures  $A_s$ ,  $A_f$ , respectively. Due to elastic strains and material inhomogeneities, start and finish temperatures differ, particularly in polycrystalline materials. Because of the activation energy needed to initiate the transformation a hysteresis exists between the martensitic and the reverse transformation. This can be seen in Figure 2.9 and Figure 2.11, which show typical measurements to identify the transformation properties. The hysteresis width depends on the compatibility of martensite and austenite lattice structures [18].

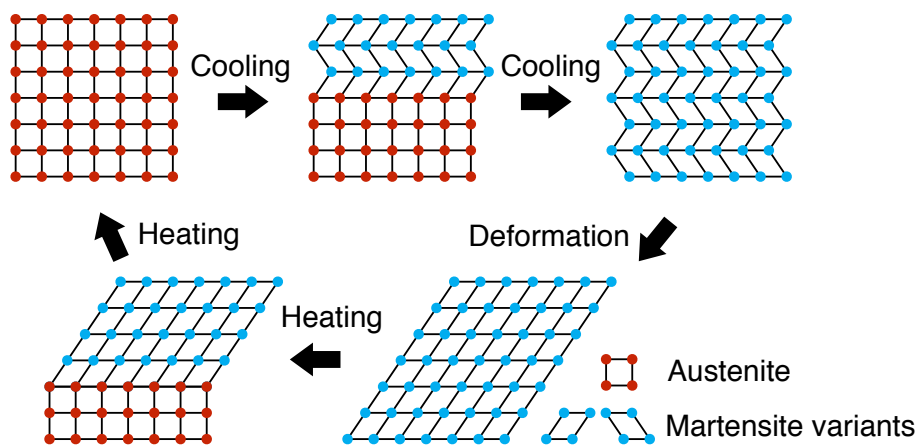


Figure 2.1: Schematic of shape memory alloy lattices on cooling, deformation, and heating.

### 2.1.1.1 One-Way Effect

The one-way effect of SMAs is based on a loading and heating cycle as shown in Figure 2.2. The original shape of the SMA is deformed under a mechanical load passing a stress-plateau where detwinning of martensite variants takes place. On unloading, this pseudo-plastic strain remains because of the detwinned martensite variants.

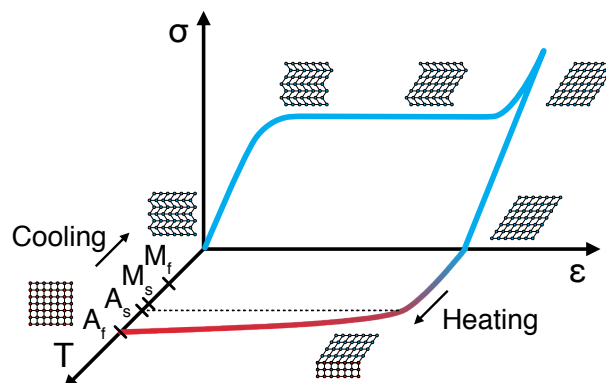


Figure 2.2: Stress-strain-temperature graph of the one-way effect in SMA. The change of lattice and re-orientation of martensite variants is depicted in the insets.

The SMA is then heated up above its austenite phase transformation start and finish temperatures  $A_s$  and  $A_f$ . Thereby, the original shape is recovered because of the transformation to the cubic austenite phase. Reducing the temperature again results in the

martensitic phase transformation, starting at martensite start temperature  $M_s$ , and ending at the finish temperature  $M_f$ . The overall shape is maintained, as the martensite variants form in a self-accommodated way.

### 2.1.1.2 Two-Way Effect

By training it is possible to induce lattice defects, which favor a certain orientation of the martensite variants at the martensitic transformation. Therefore, a full two-way shape memory effect can be triggered, as shown in Figure 2.3. On heating the original shape is recovered, while on cooling an induced second shape is regained. There must be no mechanical load on cooling, as this effect is not capable to deliver work output.

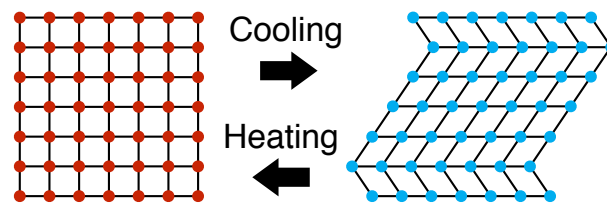


Figure 2.3: Lattice change in two-way shape memory effect. On cooling, a certain orientation of martensite variants is favored.

### 2.1.1.3 Superelasticity

The phase transformation temperatures of SMA materials depend on the free energy equilibrium of martensite and austenite. Therefore, the change of the external energy by a mechanical load shifts the transformation temperatures. This leads to the so called superelasticity. If a stress is applied to SMA material at a temperature above  $A_f$  in austenitic state, martensite is formed from a critical stress on, oriented with the short axis perpendicular to the load direction. This leads to a large stress-strain plateau, as shown in Figure 2.4. On unloading, the transformation back to austenite takes place, and the original shape is recovered.

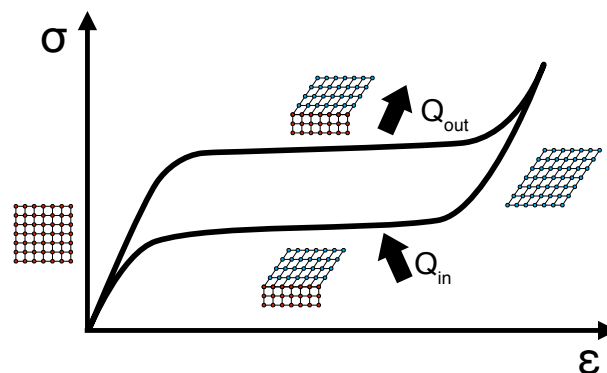


Figure 2.4: Stress-strain graph for the superelastic effect of SMA. By applying stress, a phase transformation is induced, releasing heat. On load removal, the reverse transformation takes place, absorbing heat.

As the stress-induced transformation releases heat, and the reverse transformation absorbs heat, this effect can also be used for cooling and heating. In [19] the elastocaloric

properties of Ni-Ti films are investigated in detail.

### 2.1.2 Ferromagnetic Shape Memory Alloys (FSMA)

As described in the introduction, magnetic SMA belong to the class of multiferroic materials, showing various couplings between their physical properties. Ferromagnetic SMA (FSMA) materials belong to the group of Heusler alloys, described in detail in [20]. In FSMA, both martensite and austenite phases are ferromagnetic, and a ferro- to paramagnetic transition takes place at the Curie temperature  $T_C$ .

The most popular FSMA material is Ni-Mn-Ga. As a bulk single crystal, it shows magnetic field-induced reorientation (MIR), first described in 1996 [5]. Recoverable strains of up to 21% are possible, depending on the modulation of martensite variants [21]. The MIR effect can be explained by the strong coupling of the short  $c$ -axis and the magnetic easy axis of Ni-Mn-Ga martensite unit cells (see Figure 2.5) due to magnetic anisotropy. Therefore, a reorientation of the martensite variants cannot only be induced by stress, but also by an external magnetic field. The magnetization of the FSMA material depends on the orientation of the magnetic easy axis and thereby on the orientation of the martensite variants. By reorienting them with an external load, a magnetization change can be induced [6].

Figure 2.5 shows the principle of the magnetic shape memory effect. In the initial single variant state all short axes are oriented in horizontal direction (a). On mechanically loading the sample, martensite variants start to reorient, and a twin boundary forms at a certain angle (b). By the external load a large part of the sample can be reoriented in a way that all short axes are in loading direction (c). Only a small rest of unit cells with horizontally oriented  $c$ -axes remains, due to the pinning of the twin boundary at the clamping. If a magnetic field is applied, the magnetic moments in the unit cells begins to rotate (d). When the anisotropy energy is overcome, the unit cells reorient by twin boundary motion (e). Thereby, their magnetic easy axes are aligned in the direction of the magnetic field, as indicated (f).

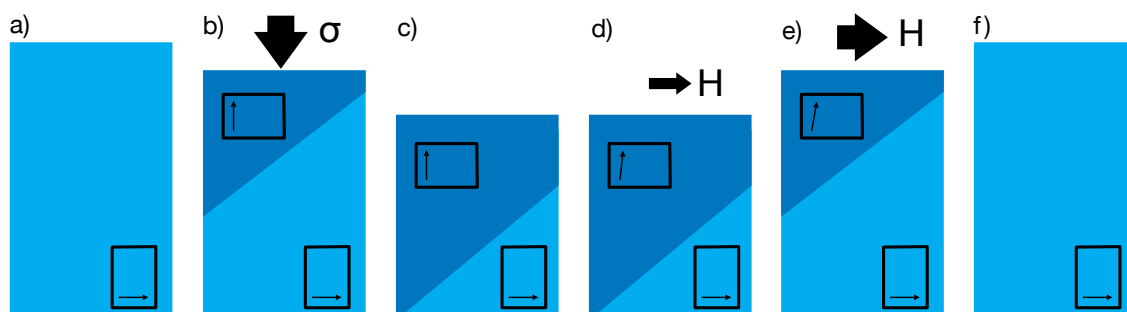


Figure 2.5: Schematic of the magnetic shape memory effect based on reorientation.

The MIR works best in bulk single crystals but recently it was found to work also in epitaxial thin films on a substrate [22]. Polycrystalline Ni-Mn-Ga material does not show

MIR, because of much higher detwinning stresses due to the grain boundaries. However, the thermomagnetic behavior remains very similar, and the sharpness of the ferro- to paramagnetic transition is only dependent on the homogeneity and the stoichiometry of the material. Besides the transformation temperatures, in FSMA also the Curie temperature can be tuned by changing the composition [23].

### 2.1.3 Metamagnetic Shape Memory Alloys (MSMA)

In addition to FSMA, there is another group of magnetic SMA Heusler Alloys, which are called metamagnetic shape memory alloys (MSMA). The most prominent representatives are Ni-Mn-X (X=In, Sn, Sb) alloys [24]. There are numerous other Heusler Alloys, showing a metamagnetic behavior. Characteristic for MSMA is a para- or antiferromagnetic martensitic phase, while the austenite is ferromagnetic. This leads to a rapid change of magnetization at the phase transformation, as can be seen in the thermo-magnetization curve of a Ni-Co-Mn-In sample in Figure 2.6. In contrast to the ferro- to paramagnetic transition of FSMA, the magnetization change of the first order phase transformation in MSMA shows a hysteresis. However, this hysteresis can be minimized by tuning the lattice parameters of martensite and austenite unit cells [25].

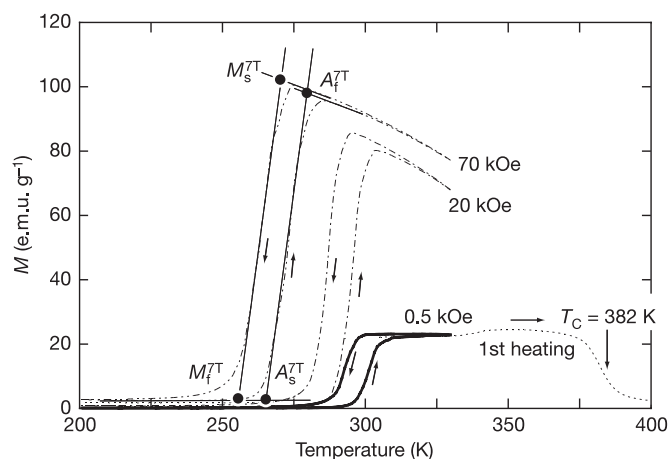


Figure 2.6: Typical thermo-magnetization measurements of MSMA material. In this graph the magnetization of a Ni-Co-Mn-In alloy is shown at different external magnetic fields. The transformation temperatures depend on the external magnetic field. [26] © 2006 npg

Besides the change of magnetization on heating or cooling, it is shown that an external magnetic field can influence the transformation temperatures of MSMA. This can be used to trigger a magnetic field induced phase transformation, which is especially interesting in the field of magnetocalorics [26].

## 2.2. Pyroelectricity

Pyroelectricity is the effect of changing electric polarization on heating or cooling of a pyroelectric material. The equation describing the effect shows a linear correlation of polarization change  $\Delta P$  and the temperature difference  $\Delta T$ :

$$\Delta P = p \cdot \Delta T . \quad (1)$$

$p$  is the pyroelectric coefficient. Pyroelectric materials have an intrinsic dipole moment, like piezoelectric materials. A simple explanation of the pyroelectric effect is given in Figure 2.7. On the left side, the crystal structure of a pyroelectric material is shown, including its polarization  $P$ . On the right side, the potential energy vs. the position  $d$  of the cation is given. The thermodynamically most favorable position for the cation is  $d_{eq}$  in the center of the potential well. At higher temperatures or potential energies,  $d_{eq}$  changes due to the asymmetric potential well. Thereby, the distance of the cation and anion increases and the overall polarization decreases. If the surfaces of a pyroelectric material are coated with metal electrodes, a surface charge is generated. On heating or cooling, this surface charge changes, leading to an electric current, which can be used for sensing or energy harvesting as described in Chapter 3.2.2. A more detailed description of the pyroelectric effect can be found in [27].

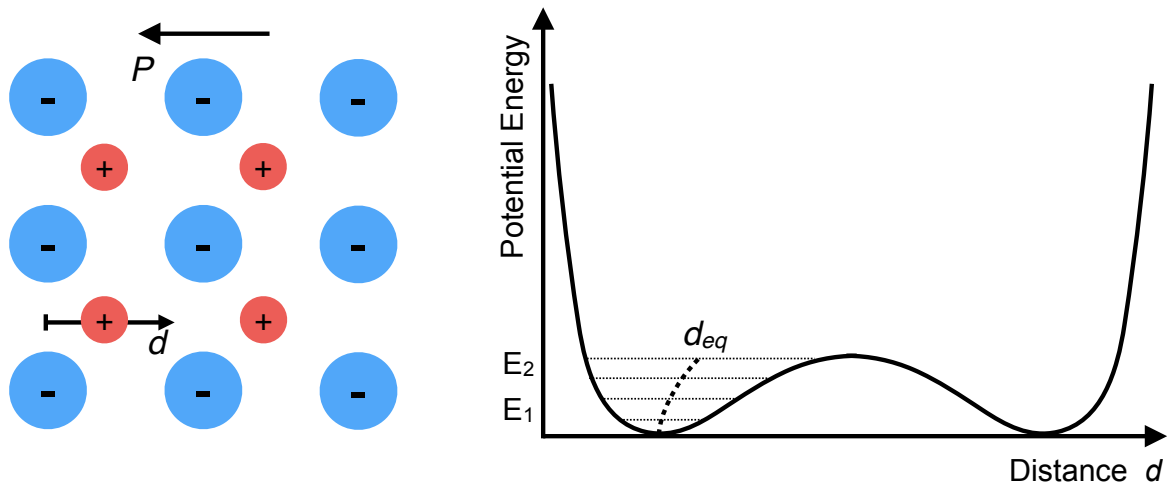


Figure 2.7: Schematic of the pyroelectric effect. The equilibrium position  $d_{eq}$  changes at higher potential energy.

### 2.3. Electromagnetism - Faraday's Law

Faraday's law, or the law of induction, discovered by Michael Faraday in 1831, describes the induction of an electromagnetic force upon a changing magnetic flux in a wire loop. The change of magnetic flux can be formulated by a surface integral on the time derivative of the flux density. Equation (2) shows the coupling of the induced electric field along the wire loop and a time-dependent change of the magnetic flux.

$$\oint_{\partial A} \vec{E} \cdot d\vec{s} = - \int_A \frac{\partial B}{\partial t} d\vec{A} \quad (2)$$

A more thorough description of Faraday's law and basic principles of electromagnetic energy harvesting can be found, e.g., in [28].

## 2.4. Measurement Methods

In this section the measurement methods used for characterizing the material properties and the performance of the energy harvesting devices are described. As most of the techniques are widely known, only a short introduction to each method is provided. Further information on material characterization can be found in [29].

### 2.4.1 Differential Scanning Calorimetry

Differential Scanning Calorimetry (DSC) is a thermoanalytical technique with the capability to characterize phase transformations in a variety of different materials. The principle is based on subjecting two cups, one with the material to investigate, the other a reference cup, to the same thermal sequence. Ideally, the reference cup has a perfectly linear response due to a constant heat capacity. This means that the amount of heat, which is absorbed from the reference material, increases linearly with the temperature. Phase transitions can be identified by a deviating heat flow to the second cup, containing 5 to 40 mg of the material to investigate. The differing heat flow is identified by comparing the measured temperature below the two cups. A schematic of the working principle is shown in Figure 2.8.  $T_{\text{Reference}}$  and  $T_{\text{Sample}}$  denote the temperatures measured below the reference cup and the sample cup.  $\Phi_{\text{H}}$  and  $\Phi_{\text{C}}$  denote the heat flux for heating and cooling, respectively, and  $\Phi_{\text{L}}$  the heat flux into the sample related to the latent heat.

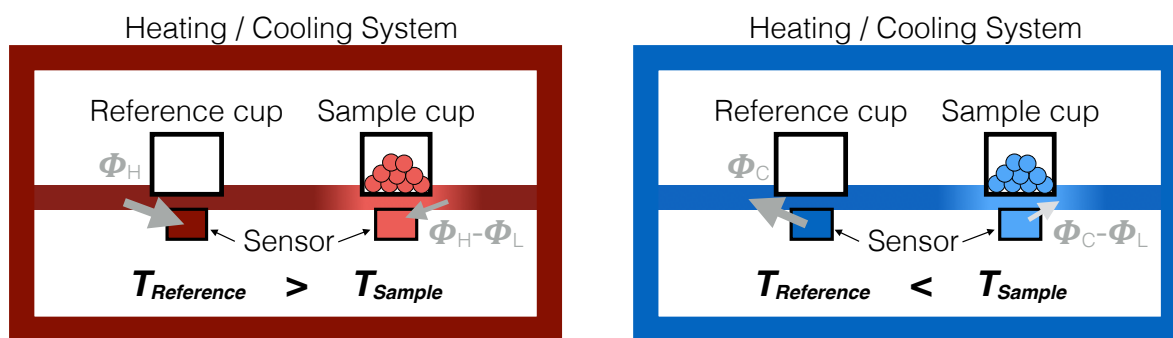


Figure 2.8: Schematic of DSC working principle on heating and cooling, respectively.

The temperatures  $T_{\text{Reference}}$  and  $T_{\text{Sample}}$  increase linearly until a phase transition takes place. If the phase transformation is endothermic, like the reverse martensitic transformation from martensite to austenite, latent heat is absorbed by the sample. This leads to a temperature difference, which is proportional to the absorbed heat. On cooling, the martensitic transformation, which is exothermic, takes place and the sample provides the latent heat as additional heat flux, which leads also to a temperature difference. Measuring this temperature difference, and therefore the heat flux into the sample versus a temperature sequence, leads to material specific DSC curves. A DSC measurement for the magnetic SMA thin film material Ni-Mn-In-Co is shown in Figure 2.9. The

beginning and ending of the peaks, determined by the tangent method, indicate the start and end temperatures of phase transformation. The latent heat can be calculated by calculating the area below the transformation peaks. Further information on how to perform and analyze DSC measurements is given in [30].

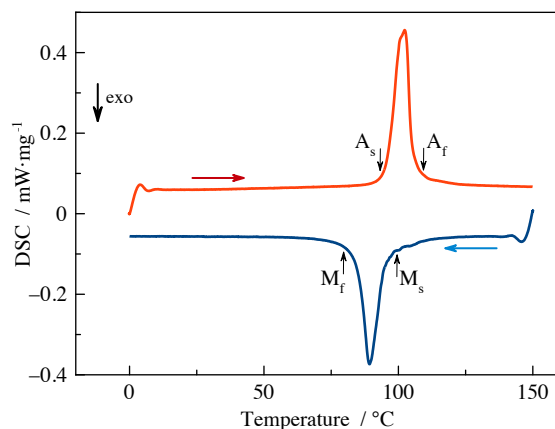


Figure 2.9: DSC curve of a magnetic SMA thin film material.

### 2.4.2 Electrical Resistance Measurement

The lattice parameters of SMA materials change strongly between austenitic and martensitic phase. This change in lattice parameters also influences the electrical conductivity of the material. Therefore, measuring the electrical resistance of a SMA sample at different temperatures, is a relatively easy means to check the transformation temperatures. In order to measure the resistance as function of the temperature, the SMA material is placed in a thermostat where it is connected according to the four-wire method as depicted in Figure 2.10.

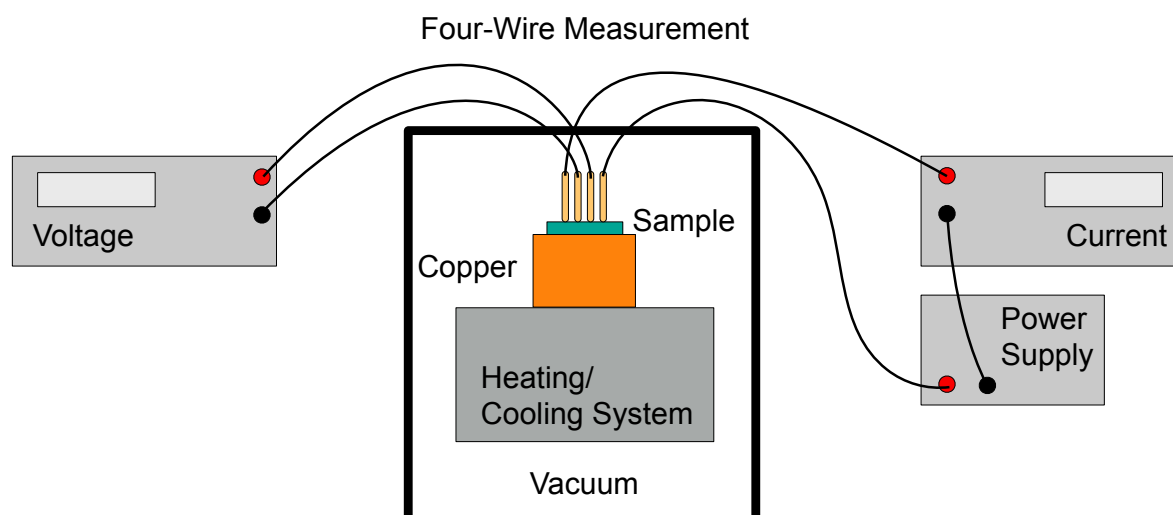


Figure 2.10: Schematic of electrical resistance measurement using the four-wire method.

The heating and cooling systems are controlled to hold a steady temperature, at which the resistance of the sample is measured. The whole thermostat is in vacuum to pre-

vent the SMA from oxidation at elevated temperatures.

Figure 2.11 shows a typical electrical resistance vs. temperature curve of a magnetic SMA thin film, showing first a linear increase of resistance in the martensitic phase, then a drop in resistance. In most cases, the austenitic phase has higher conductivity due to the higher symmetry of the lattice. Therefore, the transformation from martensite to austenite can be identified by a drop of resistance on heating. Further heating causes a linear increase in resistance of the austenitic sample. At about 80 °C, a second nonlinearity can be identified, which is due to the loss of magnetic ordering at the ferro- to paramagnetic transition.

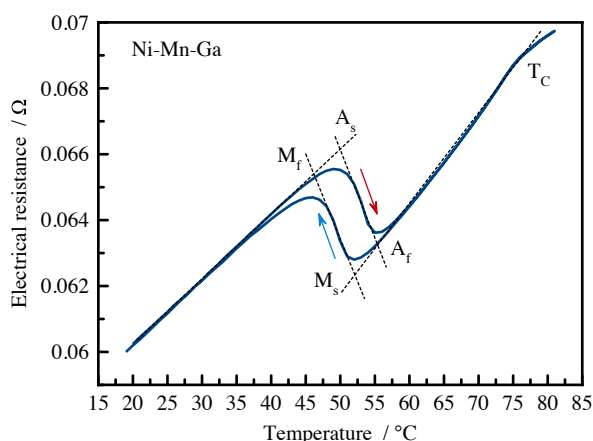


Figure 2.11: Electrical resistance versus temperature of a Ni-Mn-Ga sample.

On cooling, the increase of electrical resistance is at lower temperatures than the resistance drop, due to the hysteresis of the transformation. In martensite, the electrical resistance then decreases linearly. For evaluation of the measurement, the linear increase in resistance of the martensitic and austenitic phase, as well as the resistance drop during transformation, are fitted by tangents. The intersections of the tangents then denote the start and finish temperatures of the martensitic and reverse transformation, which are  $A_s$  and  $A_f$  for the transformation from martensite to austenite, and  $M_s$  and  $M_f$  for the reverse transformation. The hysteresis width is derived by the equation

$$\Delta T_{Hys} = \frac{1}{2} \cdot (A_f - M_s + A_s - M_f). \quad (3)$$

### 2.4.3 Tensile Measurements

Investigations of the mechanical properties of the SMA materials, as well as of other structural elements, are performed with a Zwicki-Line tensile test machine from Zwick Roell. It is equipped with a 50 and a 5 N load cell with an accuracy of 1%. Before the actual measurement of the samples, a rigid reference measurement has to be performed in order to compensate the error evoked by the intrinsic strain of the load cell. Figure 2.12 shows a photo of the tensile test machine. For the tensile test experiments the magnetic SMA films are structured by lithography to stripes of 2 mm width. The

specimens are then mounted by adhesive bonding to ceramic plates, which are fixed in the tensile test machine.



Figure 2.12: Photo of the Zwicki-Line tensile test machine.

#### 2.4.4 Elastometer

For small forces below 0.1 N, the tensile test machine is not suited very well. Therefore, measurements requiring a higher resolution are performed with an elastometer. The working principle of this machine is similar to a high precision balance, but with an inverse setup and a hook to apply forces on the specimens. The hook rests stationary, while a platform, upon which the specimen is fixed, can be moved up and down. The position of the platform is monitored by an electronic micrometer gauge with a resolution of 10  $\mu\text{m}$ .

#### 2.4.5 Current Measurement

The electric output of the energy harvesting system is measured using a low-noise current preamplifier Model SR570 of Stanford Research Systems. Depending on the electric signal, a sensitivity of  $10^{-7}$ ,  $10^{-5}$ , and  $10^{-4}$  A/V is chosen, having an input impedance of 10000, 100, and 1  $\Omega$ , respectively. The output of the current preamplifier is a voltage between  $\pm 5$  V, which is measured with an A/D card of National Instruments at a rate of 1000 to 5000 Hz.

#### 2.4.6 SQUID Measurement

Thermomagnetic measurements are performed at Tohoku University in Japan with a superconducting quantum interference device (SQUID), capable of measuring very

small magnetic fields. The used machine is an MPMS2 from Quantum Design, Inc. It measures the material magnetization of the magnetic SMA material at external magnetic fields of up to 1 T and in a temperature range between 1.8 and 400 K. The resolution is  $1 \cdot 10^{-11} \text{ A} \cdot \text{m}^{-2}$ .

#### 2.4.7 X-Ray Diffraction Method (XRD)

Using the X-ray diffraction method (XRD), it is possible to investigate the crystal structure of materials. Caused by Bragg-reflections, peaks appear at certain angles of X-ray irradiation. Thereby, it is possible to identify the lattice structure of austenite and different martensitic variants. The method is especially helpful to characterize the crystallization process taking place during the heat treatment of free-standing magnetic SMA films after sputtering (see Chapter 2.5.2).

#### 2.4.8 Infrared Thermography

Infrared thermography is performed using the FLIR A655 camera, equipped with a measurement system based on bolometers. The camera is able to record infrared videos with its full resolution of  $640 \times 480 \text{ px}$  at up to 50 fps. High speed videos at 200 fps are recorded with limited resolution. However, because of the physical limitations of the passively cooled bolometer, the dynamic range at high frame-rates is limited. To achieve a higher resolution of the investigated area, the camera is equipped with a macro lens, which allows to record infrared videos of an area of  $16 \times 9.5 \text{ mm}^2$  with a pixel resolution of approximately  $25 \text{ }\mu\text{m}$ . Figure 2.13 shows a picture of the camera model.



Figure 2.13: Infrared thermography camera FLIR A655.

#### 2.4.9 Image Tracking

The movements of the energy harvesting demonstrators are investigated with a high speed camera (Keyence VW-6000 Motion Analyzing Microscope) with 50x magnification optics, 250 fps and a shutter time of  $1/2000 \text{ s}$ . Using the built in image-tracking software, the x and y component of the movement can be measured. As the movements recorded during this work are sometimes quite fast, this method has limitations because of the blurring during movement. This leads to an insufficient detection of the

tracked object. However, in some cases image-tracking is the only feasible method, as the camera can be placed on the side and does not to be positioned in line of the movement as it is the case for, e.g., a laser distance sensor.

### 2.4.10 Laser distance sensor

For displacement measurements at high sample rates of up to 5000 Hz with a spatial resolution of 0.5  $\mu\text{m}$ , a laser triangulation sensor is used (Panasonic HL-G103). It measures in a range of 8 mm and can record 3000 samples. At 5000 Hz, the recorded time in the buffer is 0.6 s. The triangulation method is based on a reflection of the laser beam back to the sensor. By evaluating the arrival angle of the reflected light, the distance of the object can be tracked. This method is limited to applications in which the sensor can be aligned with respect to the (linear) movement.

## 2.5. Fabrication

The magnetic SMA films used in this work are all fabricated at Tohoku University, Japan. This section describes the sputtering process of the magnetic SMA films of 1 to 10  $\mu\text{m}$  thickness and presents the most important fabrication techniques used at IMT.

### 2.5.1 Magnetron Sputtering

The term sputtering describes a physical vapor deposition technology, used to either coat a substrate, or to fabricate free-standing thin films by releasing them afterwards. Particles like argon ions form a plasma and are accelerated towards a sputter target, consisting of the material which needs to be transmitted to the substrate. On impact, the particles break the atomic bonds and release atoms of the target, which then deposit on the substrate. A schematic of a sputtering chamber using the magnetron sputter technique is shown in Figure 2.14.

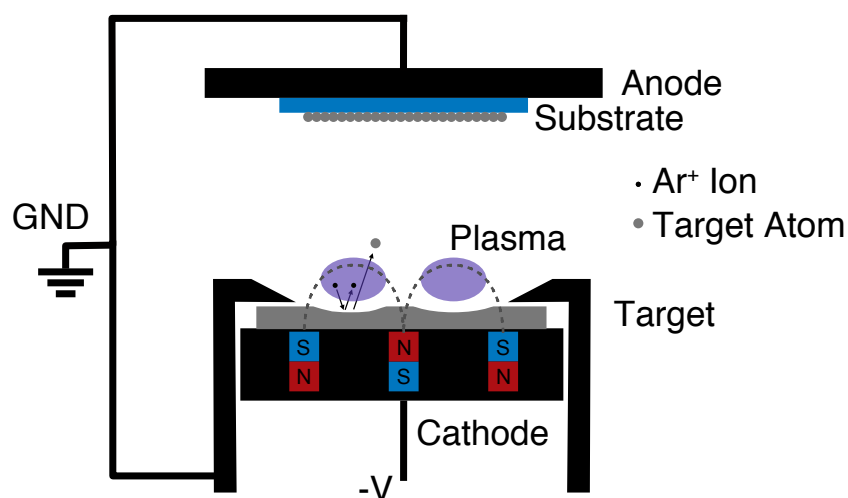


Figure 2.14: Schematic of magnetron sputtering process. Ions are accelerated towards the target, breaking atomic bonds and releasing target atoms, which deposit on the substrate.

The thin magnetic SMA films in this work are fabricated in a radio frequency (RF) mag-

neutron sputtering machine Shibaura CFS-4ES. Magnetron sputtering means that a magnetron is used to increase the ion density above the target, thereby increasing impact power and sputtering speed. The RF sputtering helps to prevent a charge build-up on the targets. As a speciality, the sputtering machine has an additional DC sputtering source, making dual magnetron sputtering with a second target possible. The RF sputter target is used to deposit the main component as Ni-Mn-Ga or Ni-Mn-In, and the DC sputter target is used to add small amounts of Co or Fe. PVA sheets are used as substrates, from which the sputtered films can be easily detached. The pressure in the chamber is  $2 \cdot 10^{-4}$  Pa. More data on the sputtering process is provided in [31].

### 2.5.2 Heat treatment

Heat treatment of as-deposited free-standing magnetic SMA films leads to a crystallization of the initially amorphous samples. Transformation properties like sharpness and hysteresis strongly depend on the heat treatment parameters, i.e. overall heating time and temperature. Generally, heat treatment takes place at 700 to 1000 °C for 1 to 10 hours. In [32], the correlation of microstructure and heat treatment is described. Figure 2.15 shows cross sections of Ni-Mn-Ga films, sputtered with 200 W in a RF magnetron sputtering apparatus, after different heat treatment.

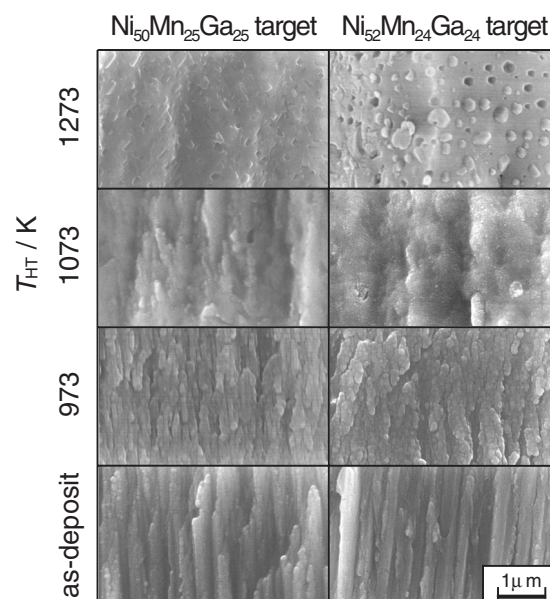


Figure 2.15: Changing microstructure of sputtered Ni-Mn-Ga films at different heat treatment temperatures. [32] © 2000 IOS press

### 2.5.3 Lithography and Wet Etching

Lithography is a basic and well established microstructuring technology. The process used in this work to structure magnetic SMA film cantilever is depicted in Figure 2.16. The magnetic SMA film is fixed on a substrate with a sacrificial layer in between. Using a spin coater, a thin layer of photosensitive "positive" resist is deposited on the sample. After soft baking at 90 °C for 5 minutes, which is a curing step for the resist, a printed

foil mask is put onto the resist layer. UV-light in a well defined dosage is used to selectively break the linkages in the resist polymer. The exposed resist dissolves in a development step with special developer solution, and a resist mask remains. The magnetic SMA thin film is structured with the fabricated resist mask by submerging the substrate in an etchant mixture of hydrofluoric acid, nitric acid, and deionized (DI) water. After 1 to 2 minutes, the magnetic SMA film in unprotected regions without resist is completely etched off, and the substrate is rinsed with DI water. Afterwards, the remaining resist is stripped away with Acetone, and the structured sample is released from the sacrificial layer. A detailed wet-etching process of Ni-Ti is described for instance in [33].

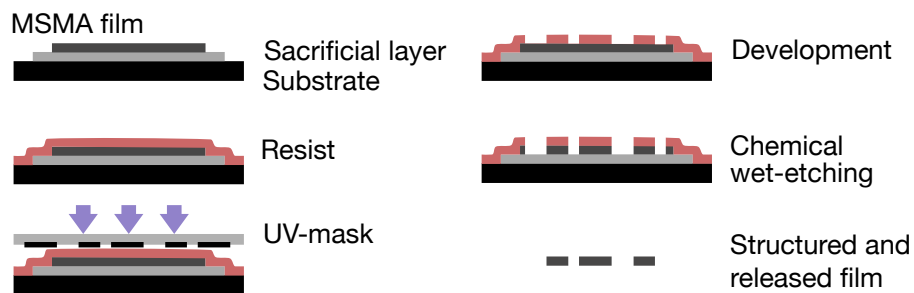


Figure 2.16: Schematic of the chemical wet-etching process.

#### 2.5.4 Laser Cutting

Besides the possibility to structure the free-standing magnetic SMA films by lithography and wet chemical etching, as described in Chapter 2.5.3, it is also possible to use a laser cutting technique. Figure 2.17 shows typical laser structured samples of a Ni-Co-Mn-In free-standing film of 5  $\mu\text{m}$  thickness.

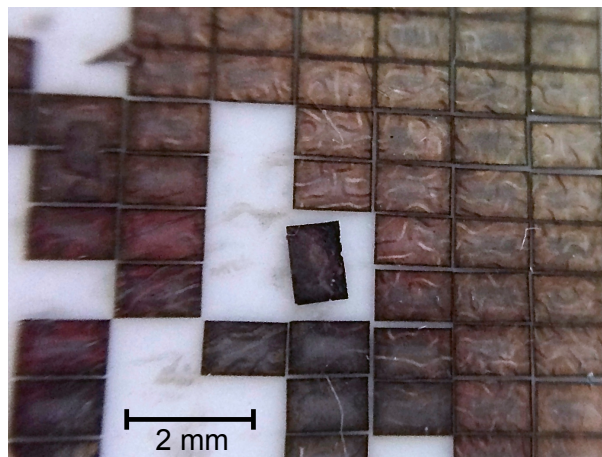


Figure 2.17: Laser-structured Ni-Co-Mn-In films on alumina substrate. The lengths of the rectangle sides are 1 and 1.5 mm, respectively.

At the Institute of Applied Materials (IAM), which is part of the KIT, it is possible to use the ACSYS Piranha II Multi F20. It is equipped with a 20 W Nd:YAG laser-source of 1064 nm, having a minimum beam width of 40  $\mu\text{m}$ , a pulse frequency of 20 - 80 Hz and a pulse length of 100 ns. The laser speed is between 1 and 3000  $\text{mm}\cdot\text{s}^{-1}$ . Because

this laser system makes use of the ablation method, some residuals of the melted material redeposit at the edges.

### 2.5.5 Microcoil Fabrication

For the electromagnetic conversion of mechanical motion to electricity, a miniature coil is needed. The set-up for fabrication of this coil is shown in Figure 2.18.

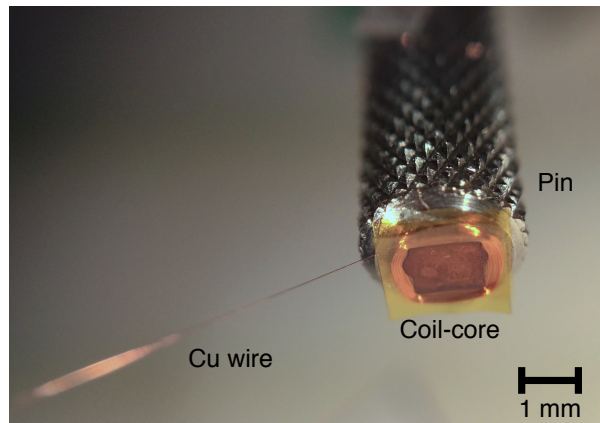


Figure 2.18: Set-up for fabrication of microcoil, using a  $2 \times 2 \text{ mm}^2$  coil core on a rotating pin and a  $15 \mu\text{m}$  thick copper wire.

In order to maximize efficiency and power output, a high number of coil windings is desired. The goal of maintaining a small size is achieved using a very thin copper wire of only  $15 \mu\text{m}$  diameter. The microcoils are fabricated manually. An individual coil-core is made from polyimide or polyester foils, consisting of an inner core and outer, limiting sheets. The thicknesses of the foils are  $25 \mu\text{m}$  for the outer sheets and  $200$  to  $500 \mu\text{m}$  for the core. The parts are assembled by stacking and using an epoxy adhesive. Afterwards, the coil-core is mounted to a rotating pin. By careful manual rotation, the coil-core is filled with thin copper wire windings in between the outer limiting sheets, as can be seen in Figure 2.18. Generally, microcoils with 100 or 200 windings are fabricated in such a manner. The overall size of a typical microcoil is  $2 \times 1.5 \times 0.4 \text{ mm}^3$ .



## 3. State of the Art of Thermal Energy Harvesting

Large scale energy harvesting from light and wind, using solar cells and wind turbines, is widely used today and competitive to other on-grid electric power generation. Apart from this large scale energy harvesting, off-grid systems, powering smaller isolated applications, also often use light, wind or small thermal power plants in combination with batteries to guarantee full service time.

Micro-energy harvesting for systems with low energy need is an essential part of future extensive wireless sensor networks [1, 34]. As batteries have only a limited lifespan, alternative energy supply becomes important, especially at places difficult to reach, where a replacement of batteries is not possible. This can be achieved by harvesting energy from light, vibration, and temperature differences in the environment [35]. As this work has its focus on thermo-magneto-mechanical energy harvesting using magnetic SMA film devices, first a short introduction to kinetic (mechanical) energy harvesting is given, followed by an overview of different thermal energy harvesting principles. In the second part the state-of-the-art of research on thermomagnetic energy harvesting and magnetic SMA actuation is presented.

### 3.1. Kinetic Energy Harvesting

Research on vibrational energy harvesting has been performed extensively in the last decade. Piezoelectric [36], electromagnetic [37], electrostatic [38], and triboelectric [39] principles are the most important ones, and they are already very close to application in energy harvesting systems. The principles are mostly based on a mass-spring system and exist from MEMS size up to macro scale. Figure 3.1 shows a typical piezoelectric energy harvesting principle based on a bimorph cantilever. Cantilever designs are favorable for piezoceramics, as only small strains are possible. The proof mass leads to a deflection of the cantilever if the anchor is accelerated. Thereby, a voltage is induced in the piezoelectric layer.

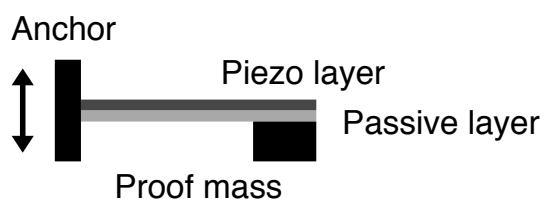


Figure 3.1: Typical piezoelectric energy harvesting principle.

Electromagnetic energy harvesters are mainly based on linear movements of a mass-

spring system, e.g., a permanent magnet moving with respect to a pick-up coil. Also moving (planar) coils are fabricated to oscillate in the magnetic field of a fixed permanent magnet. An example for a MEMS based electromagnetic energy harvesting device with a moving magnet and electroplated planar coils is shown in Figure 3.2 [40].

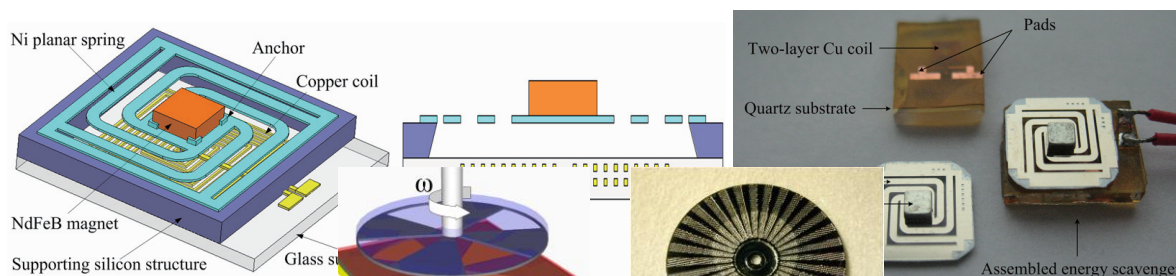


Figure 3.2: Schematic and picture of a MEMS based electromagnetic energy harvesting device with electroplated Cu coils. The magnet has a dimension of  $2 \times 2 \times 1 \text{ mm}^3$ . [40] © 2010 IEEE

Electrostatic energy harvesting is based on the relative movement of the electrodes of a capacitor. One elastically supported electrode is the mass, moving in relation to the fixed plate. Figure 3.3 shows the principle of an electrostatic energy harvester. A detailed overview of different principles and their theoretical description thereof can be found in [38].

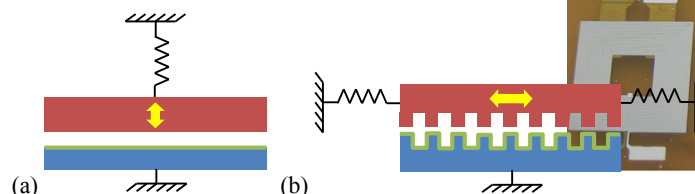


Figure 3.3: Schematic of electrostatic energy harvesting devices. [38] CC BY 3.0 © 2012 The Authors

All these systems, but especially the piezoelectric harvesters, have in common that they work best in resonance. This limits their application potential. Research is ongoing to overcome this problem, e.g., by introducing self-adjusting vibrational energy harvesting systems, suitable for a broad range of stimulation frequencies [41].

Besides conventional kinetic energy harvesting, numerous exceptional principles can be found. One of these, the FSMA based kinetic energy harvesting method, is of special interest, as the used FSMA material is very similar to the material investigated in this work. Because of the high anisotropy of magnetization along the magnetic easy axis and magnetic hard axis of single crystalline Ni-Mn-Ga, also described in Chapter 2.1.2, it is possible to use a mechanically induced reorientation to change the magnetic flux in a magnetic circuit. If the mechanical load is coupled to an external vibration source, an energy harvesting device with remarkable energy density can be build, as is shown in [42-44].

### 3.2. Thermal Energy Harvesting

Thermal energy sources in the environment can be categorized into high grade and low grade heat sources. High grade heat sources at temperatures above 250 °C are available in aluminum, iron, and cement production facilities, amongst others. However, most of the available heat energy comes from low grade heat sources like waste heat of power plants, air conditioning, process heat from chemical industry, and human body heat. As the accessible energy is limited by the Carnot efficiency, the number of available heat sources should be multiplied by their maximum Carnot efficiency. The result shows that the maximum of accessible thermal energy can be found at heat sources of about 100 °C [45]. For this reason, thermal energy harvesting with low grade heat sources at 100 °C is a very convenient way to supply low power systems like wireless sensor nodes at unaccessible places.

The absolute efficiency  $\eta_{abs}$  is defined by the electrical output  $W_{out}$  and the thermal input energy  $Q_{in}$ :

$$\eta_{abs} = \frac{W_{out}}{Q_{in}}. \quad (4)$$

For evaluating different thermal energy harvesting concepts the efficiency is compared to the thermoelectric maximum of the Carnot cycle, resulting in the relative efficiency  $\eta_{rel}$ , as shown in Equation (5).

$$\eta_{rel} = \frac{\eta_{abs}}{\eta_{Carnot}} \quad (5)$$

However, in many cases it does not make sense to only look at the efficiency, especially if the available heat is abundant. In these cases, the power density of the energy harvesting devices is of much more interest, as it defines the overall package size of a system, e.g., a self powered sensor node. Energy harvesting devices in general have to compete with batteries and are therefore required to have a maximum power density to gain an advantage over a battery of the same size, but with only a limited energy reservoir. The power density can be given either relative to the surface or the volume. This work mainly focuses on the power density  $p_v$ . The definition is dependent on the electrical power  $P$  and the volume  $v$ :

$$p_v = \frac{P}{v}. \quad (6)$$

Until now, the main focus of thermal energy harvesting research is on thermoelectric generators. Only little research is performed on pyroelectric, shape memory, thermomagnetic harvesting, and miniature heat engines. Therefore, in this chapter only the state-of-the-art of the most common thermal energy harvesting principles will be discussed, with a focus on thermoelectrics. Thermomagnetic energy harvesting, as the

main focus of this work, will be discussed in Chapter 3.3.

### 3.2.1 Thermoelectric Generators

The thermoelectric effect was discovered by Thomas Johann Seebeck in 1821 and describes the occurrence of a voltage in an electric circuit of two different conductors if the links between the conductors are held at different temperatures, as shown in Figure 3.4.

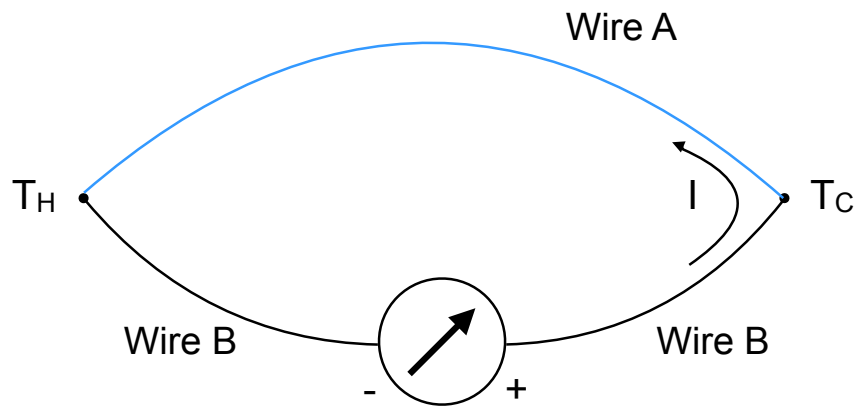


Figure 3.4: Generation of a voltage if the electric circuit, consisting of wires of different conductors, is exposed to a hot temperature  $T_H$  at the left, and a cold temperature  $T_C$  at the right link.

This effect can be explained by the principle of thermodiffusion. The charge carriers at the hot side have a longer free path, caused by their higher energy compared to the charge carriers on the cold side. This difference leads to an accumulation of charge carriers at the cold side by diffusion. Resulting from that, an electric field forms along the material, as depicted in Figure 3.5. A more detailed explanation of this effect includes the temperature-dependent change of the Fermi-function of the material [46].

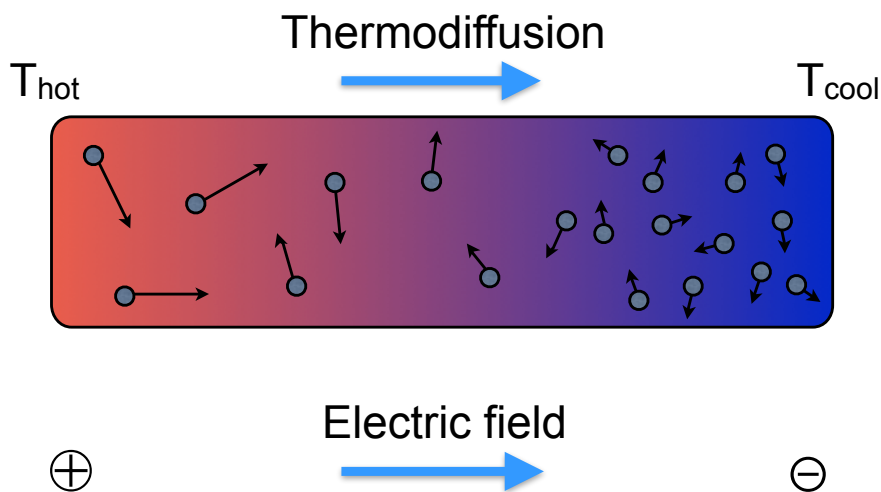


Figure 3.5: Principle of thermodiffusion: hot charge carriers have a longer length of run. Therefore, diffusion towards the cold side takes place. An electric field is generated in the material.

The Seebeck coefficient describes the materials capability to generate an electric field when submitted to a thermal gradient. While pure metals only show very low Seebeck coefficients, semiconductors can show much larger values. The voltage  $V$ , generated in a thermoelectric material, is dependent on the temperature difference  $\Delta T$  and the Seebeck coefficient  $S$ :

$$V = S \cdot \Delta T . \quad (7)$$

A thermocouple, basis of thermoelectric generators (TEG), comprises two thermoelectric materials with Seebeck coefficients of opposite signs. These materials are electrically connected in series, as shown in Figure 3.6. Because of the opposite sign of the charge carriers, the diffusion induces an increased voltage, consisting of the contributions of both thermoelectric materials. The voltage can be raised linearly by just connecting more thermocouples in series.

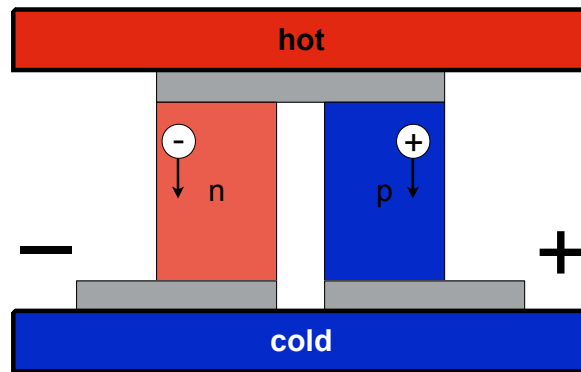


Figure 3.6: Thermocouple of a thermoelectric generator. A hot and cold reservoir are connected. Because of different Seebeck coefficients, a voltage is generated in the thermocouple.

A figure of merit  $ZT$  was introduced in order to evaluate and compare different thermoelectric materials and devices. It comprises the electric conductivity  $\sigma$ , the Seebeck coefficient  $S$ , the thermal conductivity  $\lambda$ , and the mean temperature  $T$ :

$$ZT = \frac{\sigma \cdot S^2}{\lambda} \cdot T . \quad (8)$$

The figure of merit can be used to calculate the maximum conversion efficiency in dependence of the Carnot efficiency  $\eta_c$  (see [47])

$$\eta_{max} = \eta_c \cdot \frac{\sqrt{ZT + 1} - 1}{\sqrt{ZT + 1} + \frac{T_c}{T_H}} . \quad (9)$$

The maximum power output correlates directly with the heat flux through a thermoelectric generator. As the thermal conductivity of a thermoelectric device is often relatively low, the main drawback for thermoelectric energy harvesting is the need for heat sinking beyond natural convection [48]. Usually, a large heat sink, several times the size of the harvester itself, is necessary to achieve a sufficient thermal gradient of several de-

degrees Celsius and a large heat flux.

Another problem of thermoelectrics is the challenge to develop new materials with a higher efficiency than conventional thermoelectric materials showing  $ZT$  values of about 1 in a limited temperature range. After extensive research in the field of thermoelectrics, the highest  $ZT$  value, found at 900 K in a SnSe single crystal, is 2.6 [49]. At room temperature even nanostructured material does not exceed a  $ZT$  value of 1.5 [50]. Another approach to make thermoelectrics interesting for applications, despite their relatively low efficiencies, is to make them very cheap by printing organic thermoelectric material on a thin foil in a roll-to-roll process [51]. Nonetheless, the limited power density remains a flaw, making it interesting to search for alternatives.

### 3.2.2 Pyroelectric Energy Harvesting

The pyroelectric effect, described in Chapter 2.2, was first described scientifically in the early eighteenth century [27]. For a long time, it was only an interesting phenomenon. It became important for application after it was proposed to use pyroelectric tourmaline crystals as IR sensors in spectroscopy [52]. This is still the most important use of pyroelectric material today. As pyroelectric materials are closely related to piezoelectric materials, it is obvious to investigate also the energy harvesting capabilities of the pyroelectric principle, as the pyroelectric effect is inherent to a lot of piezoelectric materials, already used for energy harvesting. In [53], the theoretical competitiveness of pyroelectrics compared to thermoelectrics is described, but a practical device to verify the potential of the pyroelectric energy conversion is still missing. This is probably also due to the difficulty to provide a changing temperature instead of a stationary temperature gradient in order to generate electricity. However, several proof-of-principles were presented, making use of small heat engines, moving the pyroelectric material between a heat source and a heat sink [54-56].

### 3.2.3 Other Thermal Energy Harvesting

Besides thermoelectric and pyroelectric energy harvesting there exist numerous other possibilities to convert heat to electricity in small dimensions. A collection of MEMS based and miniature thermal energy harvesting systems and micro-heat engines can be found in [45]. The field of thermomagnetic energy harvesting will be discussed in detail in Chapter 3.3.

## 3.3. Thermomagnetic Actuation and Energy Harvesting

It is possible to use the thermomagnetic effect of a changing magnetization on heating or cooling of a material due to a 1st or 2nd order phase transformation to drive a motor and generate mechanical energy. The second option of using the changing magnetization at the ferromagnetic transition has been first proposed 1889 by Nicola Tesla in his US patent "Thermo Magnetic Motor" [57]. A patent drawing is shown in Figure 3.7,

comprising a permanent magnet (N), ferromagnetic material (A), and a heat source (H). In this chapter, the previous work on thermomagnetic motors will be summarized and an overview of thermomagnetic actuation based on magnetic SMA will be given.

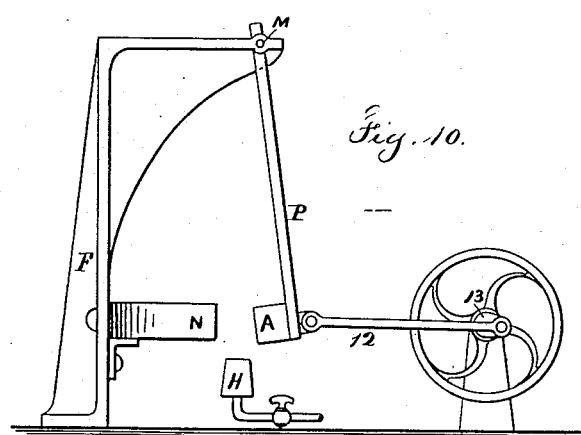


Figure 3.7: Thermomagnetic motor, patented by Nicola Tesla in 1889. [57]

### 3.3.1 Thermomagnetic Motors based on Ferromagnetic Transitions

Research on thermomagnetic motors has been very slow during the last century because of the very low efficiencies achievable by the available materials. In 1949, Brillouin did some theoretical estimates on the efficiency [58]. Further research was then conducted mostly by taking Gadolinium into account as active material, as it became more readily available [59-61]. Gadolinium has a Curie temperature close to room temperature and is therefore interesting for experimental work [62]. Different concepts based on fluidic heating and cooling of this thermomagnetic material were proposed by Kirol [63]. In 1988, Solomon did further calculations and optimizations and developed a general model [64]. In recent years, new models and investigations of the thermomagnetic motor, also called Curie machine, were build up, making use of the finite element method (FEM) and multiphysics simulation to optimize the design [65-68]. A solely theoretical and very general study on efficiencies of thermomagnetic motors is presented in [69].

Researchers at UCLA presented a miniature energy harvesting prototype based on the change of magnetization of Gadolinium. A piezoelectric spring structure moves the material between a hot and cold reservoir, as shown in Figure 3.8 [70, 71]. The results of this work comprise a characterization of the mechanical energy available in the system and an analytical approach to estimate a potential electrical output. A maximum area density of power of  $3.6 \text{ mW}\cdot\text{cm}^{-2}$  is claimed to be achievable, using high efficiency piezoelectric energy conversion. The system design was analyzed theoretically in subsequent work with regard to power output and efficiency, stating that with optimizations an average power output of more than  $250 \text{ }\mu\text{W}$  is achievable, corresponding to a power density of up to  $1 \text{ mW}\cdot\text{cm}^{-3}$  [72]. Also, a study on improved material was conducted showing maximum relative efficiencies of up to 20% of Carnot. A need of mate-

rials with large  $\Delta M/\Delta T$  and very homogeneous magnetization, found in single crystals for instance, was identified as well [73]. Sandoval et al. investigated the use of Nickel nanofilms and the change of thermodynamic efficiencies [74].

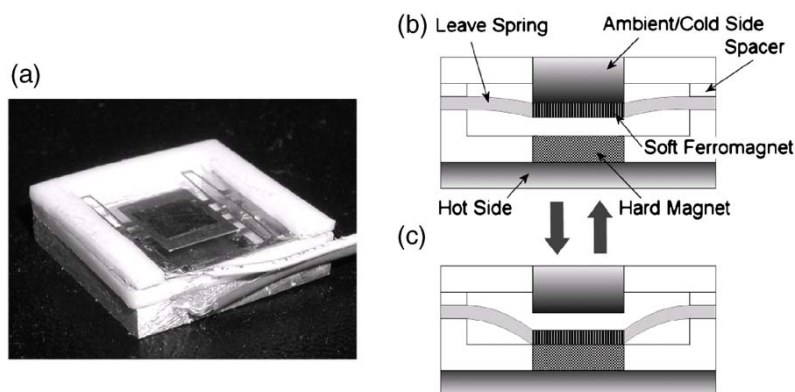


Figure 3.8: Demonstrator device of a miniature thermomagnetic energy harvester. [70] © 2007 AIP Publishing LLC

Further work on miniaturized thermomagnetic energy harvesting includes the modeling of a harvester based on a thermomagnetic fluid [75], another model of a Gadolinium based harvester with piezoelectric transduction [76], and two demonstrator devices, using Gadolinium as well as piezoelectric material to generate electric energy [77, 78]. These demonstrators showed very low frequencies ( $<0.6$  Hz) and therefore an extremely low power output.

This previous work on thermomagnetic harvesting and the numerous models of efficiency and power output give some very important clues on further development of thermomagnetic energy conversion systems.

- The thermomagnetic energy conversion is interesting for small temperature differences  $\Delta T$ . The overall efficiencies are low because of the small  $\Delta T$  but the relative efficiency compared to the Carnot cycle can get as high as 50%.
- Thermomagnetic energy harvesting is very suitable for small scale and thin films as the reduction of mass and large surface to volume ratios enable high cycling frequencies. This allows for high power densities.
- In order to achieve high relative efficiencies  $\eta_{rel}$ , materials should show a large change of magnetization  $\Delta M$  in a small temperature interval  $\Delta T$ .

### 3.3.2 Energy Harvesting by 1st Order Phase Transformation

Besides using the ferromagnetic transition in order to create electricity, magnetization changes of the material due to first order phase transformations can be used. Metamagnetic materials such as MSMA, having a nonmagnetic martensite and a ferromagnetic austenite phase, show very abrupt changes in magnetization [25]. This is due to a large change in lattice parameters on phase transformation. For energy harvesting at small temperature differences, the hysteresis of the phase transformation has to be

close to zero. In order to obtain zero-hysteresis material, the lattices of martensite and austenite have to be tuned to a good compatibility, which can be expressed by the  $\lambda_2$  parameter [79].  $\lambda_2 = 1$  gives a perfect match of the lattices, leading to zero hysteresis material [80]. At  $\lambda_2$  values close to 1, with a deviation below 0.0032, the hysteresis of most SMA is below 10 K [80], enabling abrupt changes of physical properties like magnetization on heating or cooling. Besides narrow hysteresis, a good compatibility of martensite and austenite phase also ensures a low functional fatigue [81], as a good reversibility of the first order phase transformation is ensured. Srivastava et al. present in ref. [25] the quaternary Heusler alloy  $\text{Ni}_{45}\text{Co}_5\text{Mn}_{40}\text{Sn}_{10}$  with  $\lambda_2 = 1.0032$ , showing a hysteresis of just 6 K and additionally very sharp transformations.

Based on the strong magnetization change and narrow hysteresis, Srivastava et al. propose an energy harvesting principle which directly converts a temperature change into electricity [82]. This is achieved by heating and cooling a bulk sample of the metamagnetic Ni-Co-Mn-Sn material, placed inside a pick-up coil and magnetized by an external permanent magnet as shown in Figure 3.9. The changing magnetization on first order phase transformation leads to an induced current in the pick-up coil, according to Faraday's law. The energy harvesting principle is explained in detail in Chapter 6.

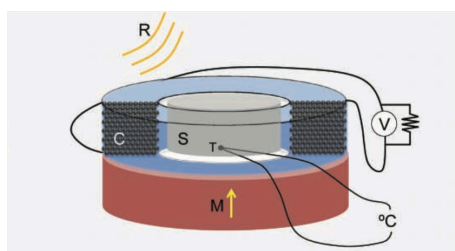


Figure 3.9: Energy harvesting principle based on the direct conversion of heat to electricity, using the first order phase transformation of MSMA. [82] © 2011 WILEY-VCH

The experimental efficiencies are very low, however, a high power density is proclaimed, competing with state-of-the-art thermoelectric energy harvesting devices. A theoretical model of the efficiency is presented in ref. [83], and ref. [84] introduces a simulation of an energy harvesting principle, similar to the thermomagnetic actuator presented in [70].

### 3.3.3 Magnetic Shape Memory Actuation

Thermomagnetic conversion principles are not limited to generate electricity from heat, they also can be used for thermal actuation. An overview of miniature magnetic SMA based actuators can be found in [13]. A more detailed description shall be given on the magnetic SMA microscanner, proposed and shown in [85].

A double beam cantilever, made from free-standing Ni-Mn-Ga thin films, is fixed on a substrate on one end and a mirror is attached to its front end. The double-beam cantilever is electrically contacted and can be heated by periodic electric heating puls-

es. Above the cantilever, a magnet is positioned, deflecting it in its initial state, as can be seen in Figure 3.10. On heating, the magnetic force decreases and the shape memory force occurs, setting the cantilever back to a horizontal position.

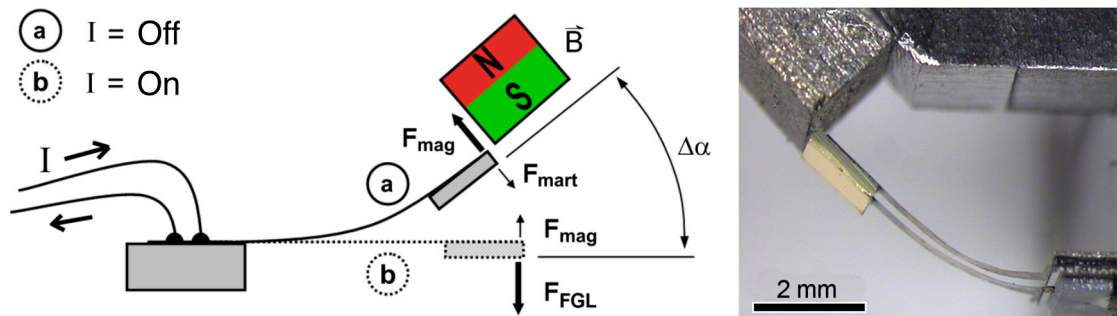


Figure 3.10: Principle of magnetic SMA based microscanner and a picture of the actual demonstrator device. [86] © 2006 IOS press

By pulsing the electric current in order to periodically heat the cantilever, very high actuation frequencies of up to 200 Hz are achievable. The high deflection angle of the cantilever makes it possible to use it for optical scanning applications, e.g., detection of obstacles in driving assistance systems [86].

## 4. Material Characterization

The material systems used in this work are ferromagnetic SMA (FSMA) based on Ni-Mn-Ga, and metamagnetic SMAs (MSMA) based on Ni-Mn-In. The fabrication and optimization of these materials has been done at the Tohoku University in Sendai, Japan. Thin films of 5  $\mu\text{m}$  thickness are fabricated by dual magnetron sputtering, described in Chapter 2.5.1. Co is added to these base systems to increase the magnetization and adjust the Curie-temperatures  $T_C$ .

Four FSMA and three MSMA films are investigated in detail, listed in Table 4.1 and Table 4.3. Measurements of mechanical, thermal, electrical, and magnetic properties are performed to identify the samples that are most suited for actuation. These samples can be differentiated by desired properties like:

- large deformation before crack,
- narrow hysteresis,
- sharp martensitic and reverse transformations,
- large change of magnetization  $\Delta M/\Delta T$  in a small temperature window,
- large maximum magnetization.

By identifying FSMA and MSMA films showing these properties, first steps towards material optimization are taken by tailoring the composition of sputtered films and applying a suitable heat treatment.

### 4.1. Ferromagnetic Shape Memory Alloys

Table 4.1 shows an overview of the Ni-Mn-Ga and Ni-Mn-Ga-Co films, which are characterized in this chapter.  $P_{\text{Sputt-1}}$  is the RF sputtering power, used for target 1,  $P_{\text{Sputt-2}}$  is the DC sputtering power for target 2. The heat treatment is described by the heat treatment temperature  $T_{\text{Heat}}$  and the heat treatment time given by  $t_{\text{Heat}}$ .

Table 4.1: Overview of the investigated FSMA films.

Target 1	$P_{\text{Sputt-1}}$ (W)	Target 2	$P_{\text{Sputt-2}}$ (W)	Composition	$T_{\text{Heat}}$ ( $^{\circ}\text{C}$ )	$t_{\text{Heat}}$ (s)
$\text{Ni}_{49.5}\text{Mn}_{28}\text{Ga}_{22.5}$	200	-	-	$\text{Ni}_{51.4}\text{Mn}_{28.3}\text{Ga}_{20.3}$	800 + 400	3600 + 3600
$\text{Ni}_{52}\text{Mn}_{24}\text{Ga}_{24}$	200	Co	5	$\text{Ni}_{51.6}\text{Mn}_{22.2}\text{Ga}_{23.9}\text{Co}_{2.3}$	900	3600
$\text{Ni}_{49.5}\text{Mn}_{28}\text{Ga}_{22.5}$	200	Co	5	$\text{Ni}_{49.3}\text{Mn}_{26.3}\text{Ga}_{22.4}\text{Co}_{2.0}$	900	3600
$\text{Ni}_{49.5}\text{Mn}_{28}\text{Ga}_{22.5}$	200	Co	12	$\text{Ni}_{47.3}\text{Mn}_{26.2}\text{Ga}_{21.8}\text{Co}_{4.7}$	900	3600

### 4.1.1 Mechanical Characterization

The mechanical characterization is performed by tensile tests. The principle and the measurement setup are described in Chapter 2.4.3. The results of the tensile tests are shown in Figure 4.1. The sample  $\text{Ni}_{51.6}\text{Mn}_{22.2}\text{Ga}_{23.9}\text{Co}_{2.3}$  with the highest Ni content is very brittle and reaches a comparatively low maximum strain of 0.4%. However, it also shows a relatively high Young's modulus of about 64.3 GPa. The  $\text{Ni}_{49.3}\text{Mn}_{26.3}\text{Ga}_{22.4}\text{Co}_{2.0}$  sample shows a larger maximum strain of up to 0.73%, having a Young's modulus of 38.3 GPa. The third sample ( $\text{Ni}_{47.3}\text{Mn}_{26.2}\text{Ga}_{21.8}\text{Co}_{4.7}$ ), shows a much larger maximum strain of up to 1.23%, and a significantly lower Young's modulus of 14.3 GPa.

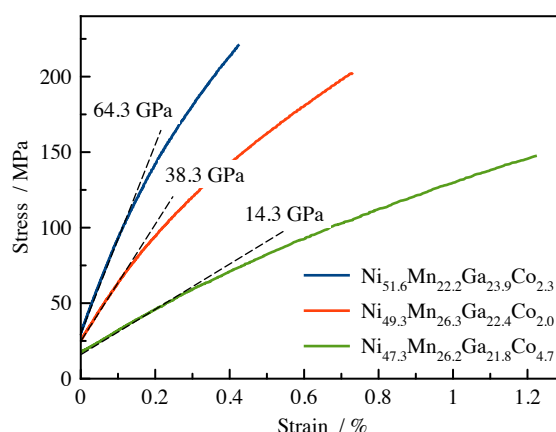


Figure 4.1: Tensile test of Ni-Co-Mn-Ga samples. The Young's modulus is marked in the graph.

### 4.1.2 Thermal Characterization

The thermal characteristics, such as transformation width and hysteresis of the FSMA films, are measured with DSC and electrical resistance measurements, as described in detail in Chapter 2.4.1 and Chapter 2.4.2. Figure 4.2 shows the temperature dependent electrical resistance of the four FSMA film samples. The transformation start and finish temperatures  $A_s$ ,  $A_f$ ,  $M_s$ ,  $M_f$ , as well as the Curie temperature  $T_C$ , are indicated in the graphs. It can be observed that the transformation temperatures are spread over a wide range and differ strongly between the different samples. This indicates that the composition and especially the Co content strongly affects the transformation.

The  $\text{Ni}_{47.3}\text{Mn}_{26.2}\text{Ga}_{21.8}\text{Co}_{4.7}$  film sample with the highest Co content also shows the highest transformation temperatures between 120 and 190 °C. The  $\text{Ni}_{51.6}\text{Mn}_{22.2}\text{Ga}_{23.9}\text{Co}_{2.3}$  film shows a similar course of electrical resistance vs. temperature with transformation temperatures between 97 and 145 °C. Different from the  $\text{Ni}_{49.3}\text{Mn}_{26.3}\text{Ga}_{22.4}\text{Co}_{2.0}$  and  $\text{Ni}_{51.4}\text{Mn}_{28.3}\text{Ga}_{20.3}$  samples, no kink, indicating the Curie temperature  $T_C$ , is observed. This is due to the relatively high transformation temperatures above  $T_C$ . The changing lattice structure from martensite to austenite has a larger effect on the electrical resistance change and covers the effect of the ferro- to paramagnetic transition. The  $T_C$  of  $\text{Ni}_{49.3}\text{Mn}_{26.3}\text{Ga}_{22.4}\text{Co}_{2.0}$  is clearly visible in the electrical resistance measurement, as the

transformation temperatures are much lower in the range from 56 to 78 °C. A narrow hysteresis of just 9 K width is seen and the sample shows sharp martensitic and reverse transformations. This indicates that a very homogeneous composition is achieved by heat treatment. As discussed in Chapter 3.3.2, the narrow hysteresis is a sign for a good matching of martensite and austenite lattice, leading to near zero hysteresis and very low fatigue, making this material interesting for cyclic actuation.

The  $\text{Ni}_{51.4}\text{Mn}_{28.3}\text{Ga}_{20.3}$  sample shows even lower transformation temperatures below room temperature, and also a lower  $T_C$  of 95 °C.

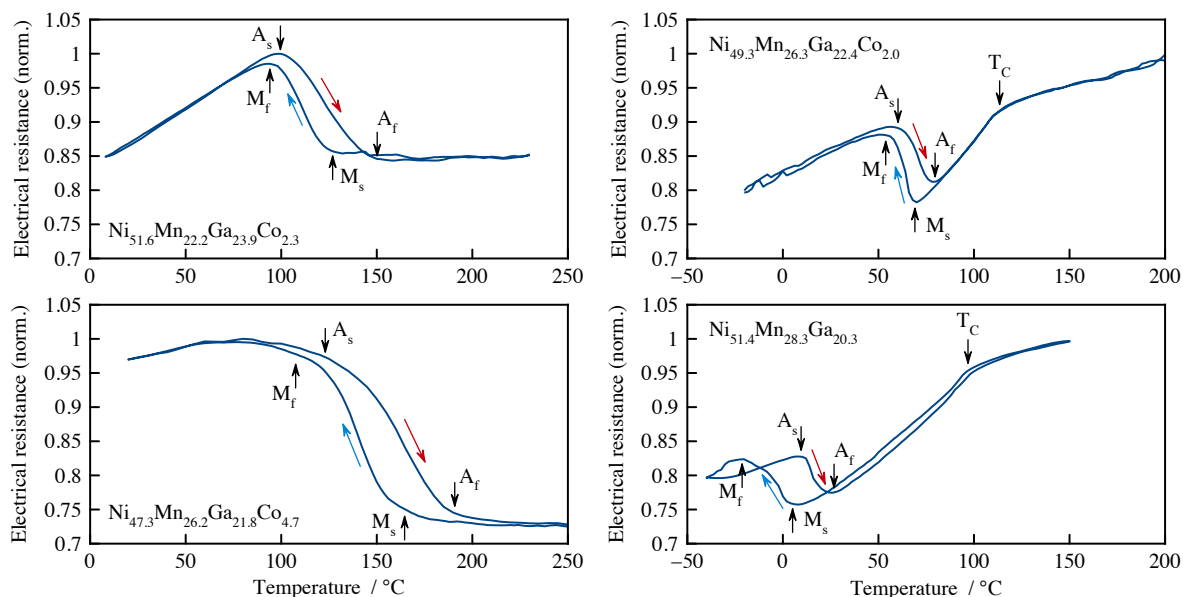


Figure 4.2: Temperature dependent electrical resistance measurement (normalized) of FSMA samples, the exact composition of the samples is marked in the graphs.

The correlation of the electrical resistance vs. temperature curve with the thermo-magnetization measurement is shown in Figure 4.3 for the  $\text{Ni}_{49.3}\text{Mn}_{26.3}\text{Ga}_{22.4}\text{Co}_{2.0}$  sample. The ferro- to paramagnetic transition at  $T_C$  matches the kink in the electrical resistance at about 115 °C.

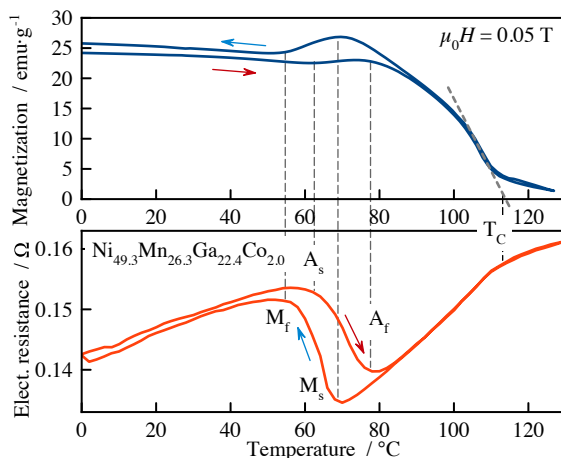


Figure 4.3: Correlation of temperature dependent resistance and magnetization measurement.

As mentioned before,  $T_C$  is not visible in the temperature dependent electric resistance measurement of the  $\text{Ni}_{47.3}\text{Mn}_{26.2}\text{Ga}_{21.8}\text{Co}_{4.7}$  and  $\text{Ni}_{51.6}\text{Mn}_{22.2}\text{Ga}_{23.9}\text{Co}_{2.3}$  samples, as the magnetic transition and the phase transformation merge to a mixed transition with a transformation from a ferromagnetic martensite to a paramagnetic austenite.

Figure 4.4 shows the DSC measurements of the FSMA film samples. A heating rate of  $10 \text{ K}\cdot\text{min}^{-1}$  is used. The transformation temperatures correlate with the ones calculated from the temperature dependent electrical resistance measurements. They are indicated in the figure, as well as  $T_C$ , which is recognizable as step. The heat capacity, which can be calculated from these measurements by dividing the specific heating power with the heating rate, is approximately  $0.6 \text{ J}\cdot(\text{K g})^{-1}$  for the samples  $\text{Ni}_{47.3}\text{Mn}_{26.2}\text{Ga}_{21.8}\text{Co}_{4.7}$ ,  $\text{Ni}_{51.6}\text{Mn}_{22.2}\text{Ga}_{23.9}\text{Co}_{2.3}$ , and  $\text{Ni}_{49.3}\text{Mn}_{26.3}\text{Ga}_{22.4}\text{Co}_{2.0}$ . The  $\text{Ni}_{51.4}\text{Mn}_{28.3}\text{Ga}_{20.3}$  sample shows a higher heat capacity which can not clearly be determined from the measurement data.

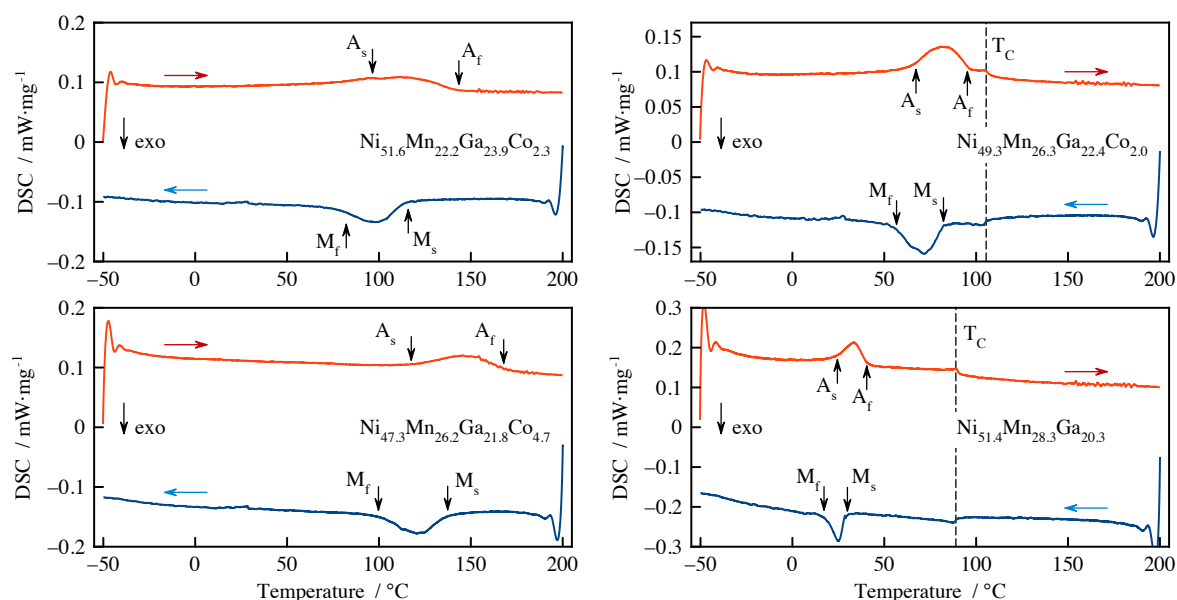


Figure 4.4: DSC measurements of the FSMA materials.

### 4.1.3 Thermo-Magnetic Characterization

Figure 4.5 shows the thermo-magnetization measurements of  $\text{Ni}_{51.6}\text{Mn}_{22.2}\text{Ga}_{23.9}\text{Co}_{2.3}$  and  $\text{Ni}_{49.3}\text{Mn}_{26.3}\text{Ga}_{22.4}\text{Co}_{2.0}$  films. The experiment is performed at an external magnetic field of 0.05 T. The highest magnetization for the Ni-Mn-Ga-Co samples is found to be approximately  $26 \text{ emu}\cdot\text{g}^{-1}$ . The maximum rate of magnetization change is found close to the Curie temperature  $T_C$  with  $0.8$  and  $1.17 \text{ emu}\cdot(\text{g K})^{-1}$ , respectively.

The thermo-magnetization measurement of the  $\text{Ni}_{51.4}\text{Mn}_{28.3}\text{Ga}_{20.3}$  sample is shown in Figure 4.6. A very sharp change of magnetization due to the ferro- to paramagnetic transition at  $T_C$  with  $\Delta M/\Delta T$  of  $2.33 \text{ emu}\cdot(\text{g K})^{-1}$  can be identified. However, further thermo-magnetization measurements at higher external magnetic fields of up to 0.5 T show that the magnetization change decreases with higher magnetic fields, as can be seen in Figure 4.6.

The magnetization vs. magnetic field of the  $\text{Ni}_{51.4}\text{Mn}_{28.3}\text{Ga}_{20.3}$  sample is presented in Figure 4.7 for different temperatures before and after the first order phase transformation.

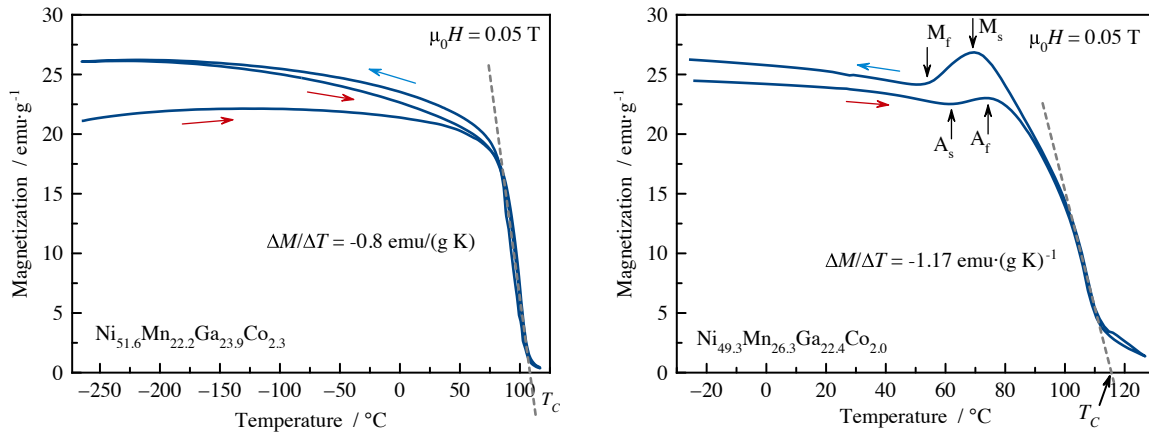


Figure 4.5: Thermo-magnetization measurements of Ni-Mn-Ga-Co films. [87] © 2015 IEEE

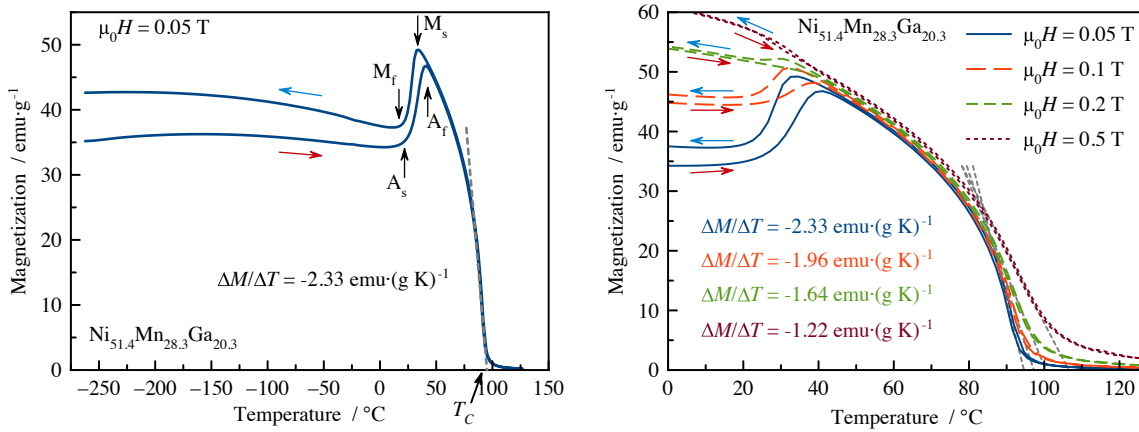


Figure 4.6: Thermo-magnetization measurements of the  $\text{Ni}_{51.4}\text{Mn}_{28.3}\text{Ga}_{20.3}$  sample at an external magnetic field of 0.05 T and at different external fields from 0.05 to 0.5 T, showing a changing slope  $\Delta M/\Delta T$ .

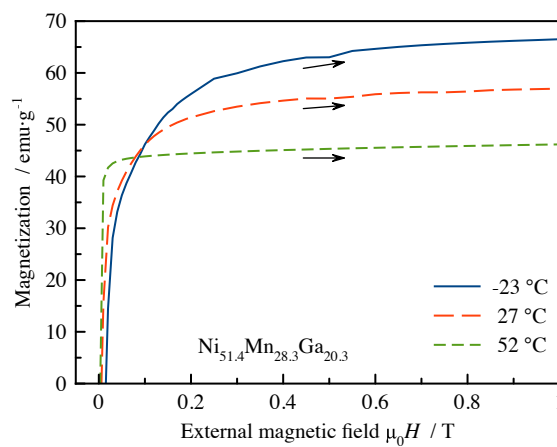


Figure 4.7: Magnetization vs. external magnetic field of the  $\text{Ni}_{51.4}\text{Mn}_{28.3}\text{Ga}_{20.3}$  sample at different temperatures.

It can be noted that the susceptibility is similar for very low magnetic fields in the austenitic state at 52 °C and in the martensitic state at 27 and -23 °C. However, the saturation is much more distinct and very sharp at 0.03 T for the austenite. This leads to an advantageous magnetization behavior at higher temperatures for low magnetic fields. Especially in the range up to 0.08 T, the austenitic state has a superior actuation capability. Low magnetic fields are sufficient to access the maximum magnetization available at the given temperature.

#### 4.1.4 Summary of FSMA Material Characterization

Table 4.2 gives an overview of the thermal properties of the FSMA films. The transformation temperatures  $A_s$ ,  $A_f$ ,  $M_s$ ,  $M_f$ , and  $T_C$  are given in °C. The hysteresis width  $\Delta T_{\text{Hys}}$  and the sharpness of the reverse and martensitic transformation,  $\Delta T_{\text{M} \rightarrow \text{A}}$  and  $\Delta T_{\text{A} \rightarrow \text{M}}$ , respectively, are displayed in K. Additionally, the maximum magnetization  $M_{\text{max}}$  in  $\text{emu} \cdot \text{g}^{-1}$  and the maximum slope of the magnetization change  $\Delta M / \Delta T$  in  $\text{emu} \cdot (\text{g K})^{-1}$  are given for an external magnetic field of 0.05 T.

Table 4.2: Summary of thermal properties of investigated FSMA films.

Composition	$A_s$	$A_f$	$M_s$	$M_f$	$T_C$	$\Delta T_{\text{Hys}}$	$\Delta T_{\text{M} \rightarrow \text{A}}$	$\Delta T_{\text{A} \rightarrow \text{M}}$	$M_{\text{max}}$	$\Delta M / \Delta T$
$\text{Ni}_{51.4}\text{Mn}_{28.3}\text{Ga}_{20.3}$	17	39	33	18	95	9.5	22	15	50	<b>2.33</b>
$\text{Ni}_{51.6}\text{Mn}_{22.2}\text{Ga}_{23.9}\text{Co}_{2.3}$	101	145	123	97	107	22	44	26	26	0.8
$\text{Ni}_{49.3}\text{Mn}_{26.3}\text{Ga}_{22.4}\text{Co}_{2.0}$	62	78	69	56	115	<b>9</b>	<b>16</b>	<b>13</b>	27	1.17
$\text{Ni}_{47.3}\text{Mn}_{26.2}\text{Ga}_{21.8}\text{Co}_{4.7}$	135	186	152	122	-	34	51	30	-	-

Based on these results the  $\text{Ni}_{49.3}\text{Mn}_{26.3}\text{Ga}_{22.4}\text{Co}_{2.0}$  and  $\text{Ni}_{51.4}\text{Mn}_{28.3}\text{Ga}_{20.3}$  films are identified for implementation in demonstrator devices. The sharp transformations of only 16 and 13 K width in  $\text{Ni}_{49.3}\text{Mn}_{26.3}\text{Ga}_{22.4}\text{Co}_{2.0}$  due to a homogenous composition make it the most suitable for thermal actuation using the shape memory effect. The narrow hysteresis of only 9 K is probably due to a  $\lambda_2$  value close to one and indicates low fatigue.

The large magnetization change  $\Delta M / \Delta T$  of  $\text{Ni}_{51.4}\text{Mn}_{28.3}\text{Ga}_{20.3}$  of  $2.33 \text{ emu} \cdot (\text{g K})^{-1}$  allows for efficient thermomagnetic actuation and energy conversion, challenging single crystalline gadolinium, showing a magnetization change of approximately  $3 \text{ emu} \cdot (\text{g K})^{-1}$  [62].

## 4.2. Metamagnetic Shape Memory Alloys

The investigated Ni-Co-Mn-In films are listed in Table 4.3.  $P_{\text{Sputt-1}}$  is the RF sputtering power, used for target 1,  $P_{\text{Sputt-2}}$  is the DC sputtering power for target 2. The heat treatment is described by the heat treatment temperature  $T_{\text{Heat}}$  and the heat treatment time given by  $t_{\text{Heat}}$ . Three Ni-Mn-In based films fabricated from a  $\text{Ni}_{45}\text{Mn}_{40}\text{In}_{15}$  and a Co target with varying Co sputtering powers are examined.

Table 4.3: Overview of the investigated MSMA films.

Target 1	$P_{\text{Sputt-1}}$ (W)	Target 2	$P_{\text{Sputt-2}}$ (W)	Composition	$T_{\text{Heat}}$ ( $^{\circ}\text{C}$ )	$t_{\text{Heat}}$ (s)
Ni <sub>45</sub> Mn <sub>40</sub> In <sub>15</sub>	200	Co	12	Ni <sub>46.5</sub> Co <sub>5.2</sub> Mn <sub>37.2</sub> In <sub>11.1</sub>	850	3600
Ni <sub>45</sub> Mn <sub>40</sub> In <sub>15</sub>	200	Co	5	Ni <sub>48.7</sub> Co <sub>1.9</sub> Mn <sub>36.3</sub> In <sub>13.1</sub>	900	3600
Ni <sub>45</sub> Mn <sub>40</sub> In <sub>15</sub>	200	Co	8	Ni <sub>50.4</sub> Co <sub>3.7</sub> Mn <sub>32.8</sub> In <sub>13.1</sub>	900	3600

### 4.2.1 Mechanical Characterization

Similar to the Ni-Mn-Ga based FSMA material, the Ni-Mn-In based MSMA films are very brittle. Figure 4.8 shows the tensile test of the Ni<sub>46.5</sub>Co<sub>5.2</sub>Mn<sub>37.2</sub>In<sub>11.1</sub>, Ni<sub>48.7</sub>Co<sub>1.9</sub>Mn<sub>36.3</sub>In<sub>13.1</sub>, and Ni<sub>50.4</sub>Co<sub>3.7</sub>Mn<sub>32.8</sub>In<sub>13.1</sub> samples. The Ni<sub>46.5</sub>Co<sub>5.2</sub>Mn<sub>37.2</sub>In<sub>11.1</sub> and Ni<sub>50.4</sub>Co<sub>3.7</sub>Mn<sub>32.8</sub>In<sub>13.1</sub> samples show relatively large critical strains for fracture of about 0.5% and 0.38%, respectively. As the Ni<sub>48.7</sub>Co<sub>1.9</sub>Mn<sub>36.3</sub>In<sub>13.1</sub> sample only shows a small critical strain of 0.17% this indicates that a higher Co amount leads to larger critical strains. The Young's moduli of 56.4 and 49.8 GPa for the Ni<sub>46.5</sub>Co<sub>5.2</sub>Mn<sub>37.2</sub>In<sub>11.1</sub> and Ni<sub>48.7</sub>Co<sub>1.9</sub>Mn<sub>36.3</sub>In<sub>13.1</sub>, show no clear correlation to the Co content. As the Ni<sub>50.4</sub>Co<sub>3.7</sub>Mn<sub>32.8</sub>In<sub>13.1</sub> film shows an even lower Young's modulus of only 28.5 GPa, the Ni content could be correlated with the Young's moduli. The results indicate that the MSMA films are more brittle than the investigated FSMA films. Therefore, a direct actuation of the material is very difficult as a cantilever would easily break on large deflection.

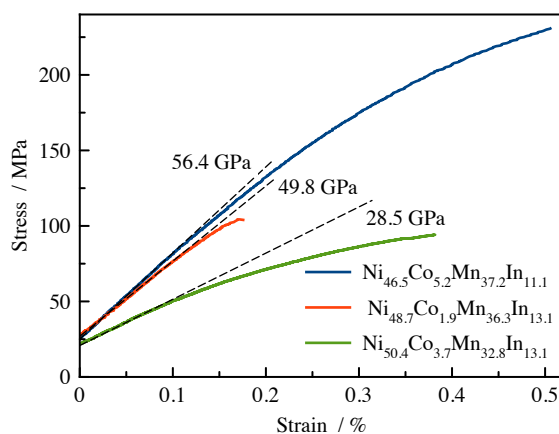


Figure 4.8: Tensile tests of Ni-Co-Mn-In samples. Young's modulus is indicated in the graph.

### 4.2.2 Thermal Characterization

The temperature dependent electrical resistance measurements, allowing the determination of the transformation temperatures, are shown in Figure 4.9. The Ni<sub>48.7</sub>Co<sub>1.9</sub>Mn<sub>36.3</sub>In<sub>13.1</sub>, and Ni<sub>50.4</sub>Co<sub>3.7</sub>Mn<sub>32.8</sub>In<sub>13.1</sub> films show a similar course of electrical resistance versus temperature, starting from a high electrical resistance, which is strongly decreasing to about 40% of the original value during phase transformation. This is different for the Ni<sub>46.5</sub>Co<sub>5.2</sub>Mn<sub>37.2</sub>In<sub>11.1</sub> film, which shows a steadily increasing electrical resistance until the transformation, when it decreases by about 10%. Afterwards

the increase of the electrical resistance compares to the increase observed before the transformation, while the other films show only a slight increase. The  $\text{Ni}_{46.5}\text{Co}_{5.2}\text{Mn}_{37.2}\text{In}_{11.1}$  film has a very large hysteresis of 64 K. In contrary, the  $\text{Ni}_{50.4}\text{Co}_{3.7}\text{Mn}_{32.8}\text{In}_{13.1}$  film shows an exceptional small hysteresis of only 6 K. This small hysteresis is comparable to the Ni-Co-Mn-Sn alloy presented in [25]. It is supposed that the compatibility of martensite and austenite lattice parameters lead to these near zero-hysteresis as discussed in Chapter 3.3.2. Additionally, also the martensitic and reverse transformation take place in small temperature intervals of only 11 and 9 K, respectively. This is due to a very homogeneous composition of the sample because of good crystallization at heat treatment. The influence of heat treatment on the sharpness of the transformation is discussed in more detail in Chapter 4.3.

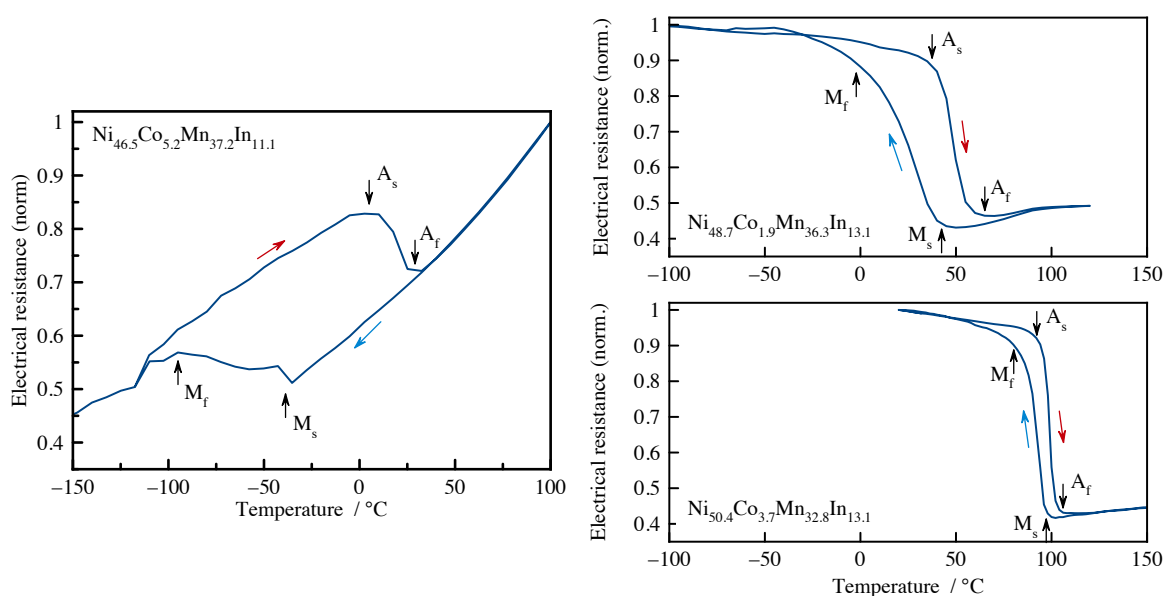


Figure 4.9: Temperature-dependent electrical resistance measurements of the MSMA film specimens, the exact composition is marked in the graphs.

The DSC measurements shown in Figure 4.10 confirm the transformation temperatures identified by the temperature-dependent electrical resistance measurements. The transformation temperatures are marked in the corresponding graph. For the DSC measurement of  $\text{Ni}_{46.5}\text{Co}_{5.2}\text{Mn}_{37.2}\text{In}_{11.1}$ , no distinct transformations can be identified, which is because of the incomplete martensitic transformation, which starts only at about  $-50\text{ }^{\circ}\text{C}$ . In the DSC curve of  $\text{Ni}_{48.7}\text{Co}_{1.9}\text{Mn}_{36.3}\text{In}_{13.1}$  also  $T_C$  can be identified. The measurement of  $\text{Ni}_{50.4}\text{Co}_{3.7}\text{Mn}_{32.8}\text{In}_{13.1}$  shows very sharp and distinct transformations, indicating a very homogeneous material composition and a good compatibility of martensite and austenite phase. From the integration of the transformation peaks the latent heat of  $\text{Ni}_{50.4}\text{Co}_{3.7}\text{Mn}_{32.8}\text{In}_{13.1}$  is determined to be  $17\text{ J}\cdot\text{g}^{-1}$ . The amount of latent heat also makes the material interesting for application in magnetocalorics, as already proposed by [88]. The heat capacity of the three investigated specimens is about  $0.6\text{ J}\cdot(\text{K g})^{-1}$  but

would have to be measured in a separate experiment to get reliable and exact values.

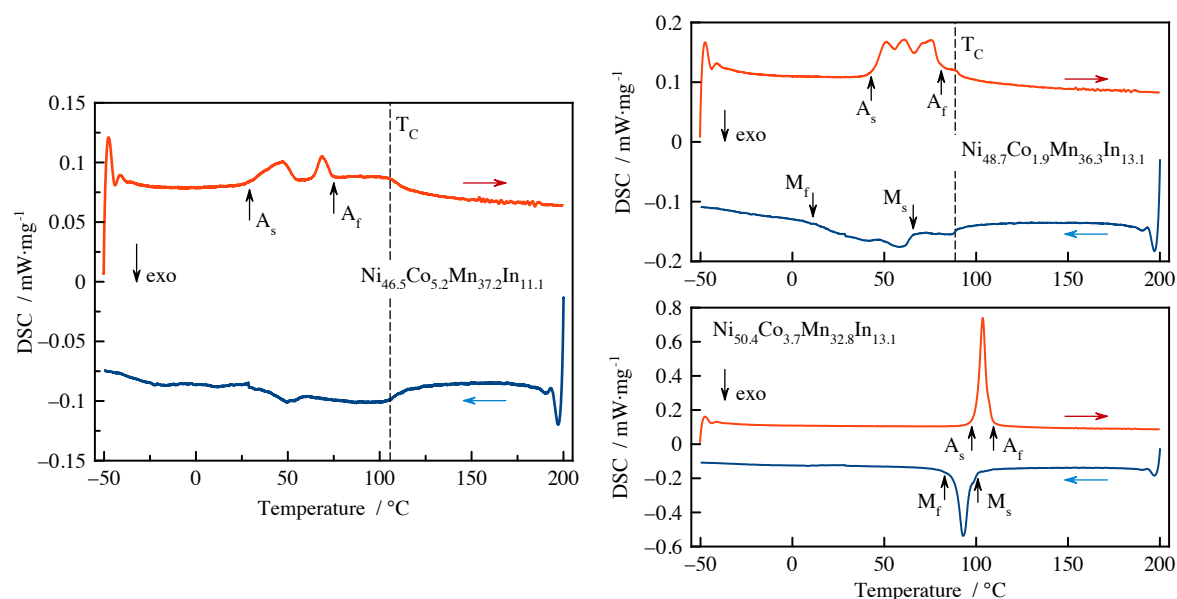


Figure 4.10: DSC measurements of the MSMA film specimens.

### 4.2.3 Thermo-Magnetic Characterization

The magnetic properties are characterized by thermo-magnetization measurements of the Ni-Co-Mn-In films. Figure 4.11 shows that the  $\text{Ni}_{46.5}\text{Co}_{5.2}\text{Mn}_{37.2}\text{In}_{11.1}$  film, having a very high Co content, reveals a ferromagnetic characteristic similar to the Ni-Mn-Ga and Ni-Mn-Ga-Co films. This is different from the thermomagnetic properties of the  $\text{Ni}_{48.7}\text{Co}_{1.9}\text{Mn}_{36.3}\text{In}_{13.1}$  and  $\text{Ni}_{50.4}\text{Co}_{3.7}\text{Mn}_{32.8}\text{In}_{13.1}$  films (Figure 4.12), showing a metamagnetic characteristic. The results correlate with the resistance measurements, shown in Figure 4.9, where also the  $\text{Ni}_{46.5}\text{Co}_{5.2}\text{Mn}_{37.2}\text{In}_{11.1}$  resistance differs strongly from the other MSMA films. Besides the ferromagnetic characteristic it shows a very high maximum magnetization of above  $90 \text{ emu}\cdot\text{g}^{-1}$  and slope of magnetization change of about  $2 \text{ emu}\cdot(\text{g K})^{-1}$ .

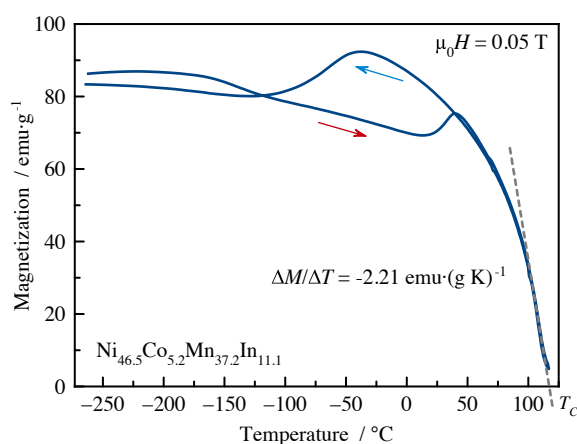


Figure 4.11: Thermo-magnetization measurements of the  $\text{Ni}_{46.5}\text{Co}_{5.2}\text{Mn}_{37.2}\text{In}_{11.1}$  film.

The thermo-magnetization measurement of the  $\text{Ni}_{50.4}\text{Co}_{3.7}\text{Mn}_{32.8}\text{In}_{13.1}$  film is shown in Fig-

ure 4.12. In martensitic phase the magnetization is close to zero. This is most probably due to an antiferromagnetic state below  $M_s$  [89]. Upon heating from martensite to austenite, the magnetization increases sharply, followed by a decrease when the film is fully transformed to the austenitic state due to the ferro- to paramagnetic transition at  $T_C$ . Cooling from the paramagnetic state leads to a strongly increasing magnetization and a maximum peak of  $25 \text{ emu}\cdot\text{g}^{-1}$  at  $0.05 \text{ T}$  external magnetic field or  $50 \text{ emu}\cdot\text{g}^{-1}$  at  $3 \text{ T}$ . When the martensitic transformation begins, the magnetization drops quickly to  $0.1 \text{ emu}\cdot\text{g}^{-1}$  in a  $0.05 \text{ T}$  external magnetic field. The magnetization changes  $\Delta M/\Delta T$  are up to  $3.17 \text{ emu}\cdot(\text{g K})^{-1}$  at the martensitic transformation, as indicated in Figure 4.12.

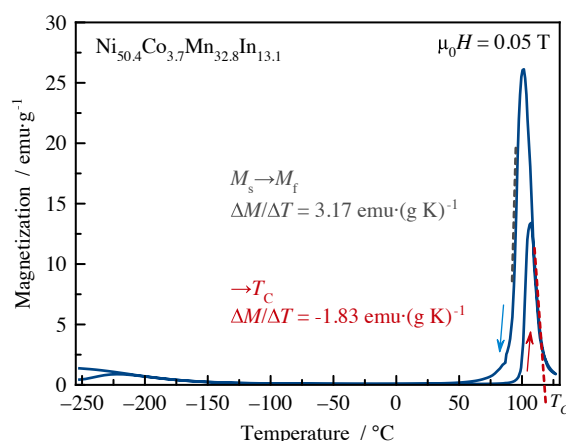


Figure 4.12: Thermo-magnetization measurement of the  $\text{Ni}_{50.4}\text{Co}_{3.7}\text{Mn}_{32.8}\text{In}_{13.1}$  film.

The magnetization versus magnetic field characteristic of the  $\text{Ni}_{50.4}\text{Co}_{3.7}\text{Mn}_{32.8}\text{In}_{13.1}$  film is shown in Figure 4.13. At room temperature, the magnetization is almost zero, even for high magnetic fields up to  $4 \text{ T}$ . When measuring the magnetization upon cooling at  $107 \text{ °C}$ , which is just before the start of martensitic transformation at  $M_s$ , a high susceptibility of the film can be seen. Saturation occurs at magnetic fields larger than  $100 \text{ mT}$ . Also a small magnetic hysteresis of the magnetization can be identified for the measurement at  $107 \text{ °C}$ .

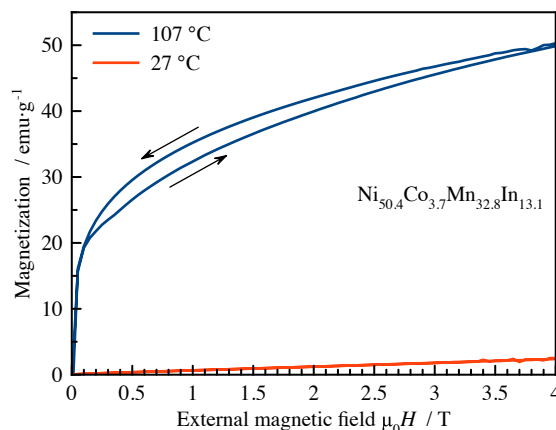


Figure 4.13: Magnetization characteristic of the  $\text{Ni}_{50.4}\text{Co}_{3.7}\text{Mn}_{32.8}\text{In}_{13.1}$  film at  $27$  and  $107 \text{ °C}$ .

#### 4.2.4 X-Ray Diffraction

XRD measurements are performed to investigate the  $\text{Ni}_{50.4}\text{Co}_{3.7}\text{Mn}_{32.8}\text{In}_{13.1}$  film at room temperature before and after heat treatment. The results are shown in Figure 4.14.

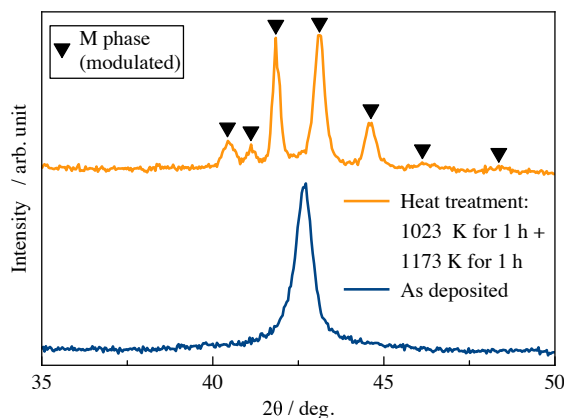


Figure 4.14: XRD measurement of  $\text{Ni}_{50.4}\text{Co}_{3.7}\text{Mn}_{32.8}\text{In}_{13.1}$  before and after heat treatment. [90]

© 2014 WILEY-VCH

Before heat treatment, no martensitic or austenitic phase can be identified, as the material is not yet crystallized. Afterwards, the peaks indicate the modulated martensitic phase, which has formed similar to other MSMA films with  $L2_1$  Heusler-type structure [31].

#### 4.2.5 Summary of MSMA Material Characterization

In Table 4.4 the results of the thermal and magnetic properties are summarized. The transformation temperatures  $A_s$ ,  $A_f$ ,  $M_s$ ,  $M_f$ , and  $T_C$  are given in °C. The hysteresis width  $\Delta T_{\text{Hys}}$  and sharpness of the reverse and martensitic transformation,  $\Delta T_{M \rightarrow A}$  and  $\Delta T_{A \rightarrow M}$ , are displayed in K. Additionally, the maximum magnetization  $M_{\text{max}}$  in  $\text{emu} \cdot \text{g}^{-1}$  and the maximum slope of the magnetization change  $\Delta M / \Delta T$  in  $\text{emu} \cdot (\text{g K})^{-1}$  are given for an external magnetic field of 0.05 T.

The  $\text{Ni}_{50.4}\text{Co}_{3.7}\text{Mn}_{32.8}\text{In}_{13.1}$  film stands out because of its very small hysteresis of only 6 K, large magnetization changes  $\Delta M / \Delta T$  of  $3.17 \text{ emu} \cdot (\text{g K})^{-1}$ , and sharp transformations below 11 K. Therefore, this is the most suitable MSMA material for thermomagnetic energy harvesting in this investigation, showing thermomagnetic characteristics similar to bulk material, e.g., shown in Ref. [25].

Table 4.4: Overview of the thermal and magnetic properties of the MSMA films.

Composition	$A_s$	$A_f$	$M_s$	$M_f$	$T_C$	$\Delta T_{\text{Hys}}$	$\Delta T_{M \rightarrow A}$	$\Delta T_{A \rightarrow M}$	$M_{\text{max}}$	$\Delta M / \Delta T$
$\text{Ni}_{46.5}\text{Co}_{5.2}\text{Mn}_{37.2}\text{In}_{11.1}$	6	36	-28	-92	116	64	30	64	92	2.21
$\text{Ni}_{48.7}\text{Co}_{1.9}\text{Mn}_{36.3}\text{In}_{13.1}$	35	58	42	2	-	16	23	40	-	-
$\text{Ni}_{50.4}\text{Co}_{3.7}\text{Mn}_{32.8}\text{In}_{13.1}$	94	103	97	86	115	<b>6</b>	<b>9</b>	<b>11</b>	26	<b>3.17</b>

### 4.3. Influence of Heat Treatment on MSMA Films

The heat treatment conditions play an important role in tailoring transformation temperatures as well as adjusting the sharpness of transformations and hysteresis width. Figure 4.15 illustrates how large the influence of heat treatment on the hysteresis can be.

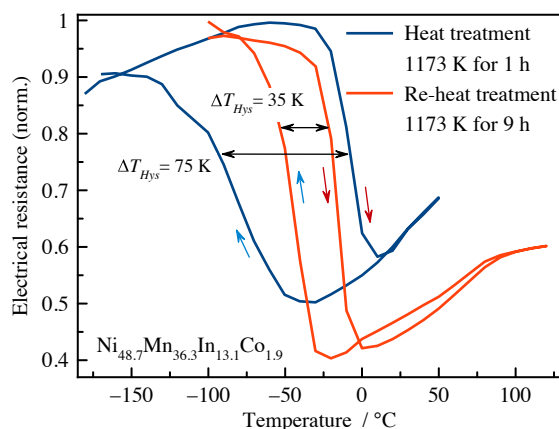


Figure 4.15: Temperature dependent electrical resistance of  $\text{Ni}_{48.7}\text{Mn}_{36.3}\text{In}_{13.1}\text{Co}_{1.9}$  sputtered film with the initial and a second heat treatment as indicated.

While the initial Ni-Co-Mn-In based film shows a hysteresis of above 70 K, a second heat treatment at 900 °C for 9 h decreases the hysteresis to about 30 K. The sharpness of the martensitic transformation  $\Delta T_{M \rightarrow A}$ , which extends to almost 75 K for the initial heat treated film reduces to approximately 25 K. Such improvements indicate, that the crystallization of the film was not complete after the first heat treatment.

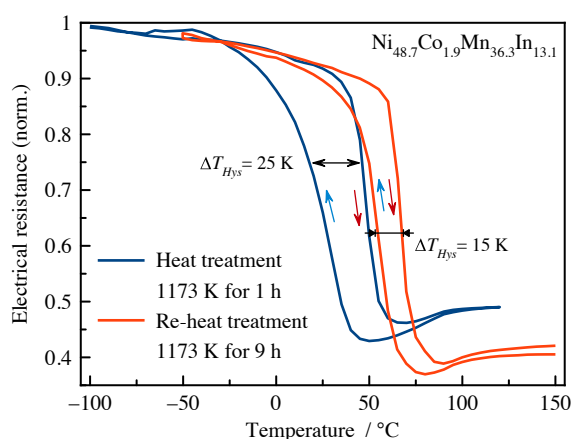


Figure 4.16: Temperature dependent electrical resistance of the initial and re-heat treated  $\text{Ni}_{48.7}\text{Co}_{1.9}\text{Mn}_{36.3}\text{In}_{13.1}$  films.

Figure 4.16 shows the initial and re-heat treated  $\text{Ni}_{48.7}\text{Co}_{1.9}\text{Mn}_{36.3}\text{In}_{13.1}$  film. After the second heat treatment at 900 °C for 9 h, the transformation temperatures increased by about 20 K and the sharpness especially of the martensitic transformation is improved by 5 K. Also the hysteresis decreased by 10 K, which is very useful for actuation of the

film, as will be explained in Chapter 6.

Figure 4.17 shows the influence of the heat treatment time on the  $\text{Ni}_{50.4}\text{Co}_{3.7}\text{Mn}_{32.8}\text{In}_{13.1}$  film. When re-heated for another 9 h after an initial heat treatment at 900 °C for 1 h, the transformation temperatures decrease by about 10 K. The hysteresis and also the sharpness of the transformations increase by 5 K and 2 K, respectively, but stay very similar to the initial film. This indicates that the initial heat treatment was sufficient to generate a well crystallized and homogeneous film structure.

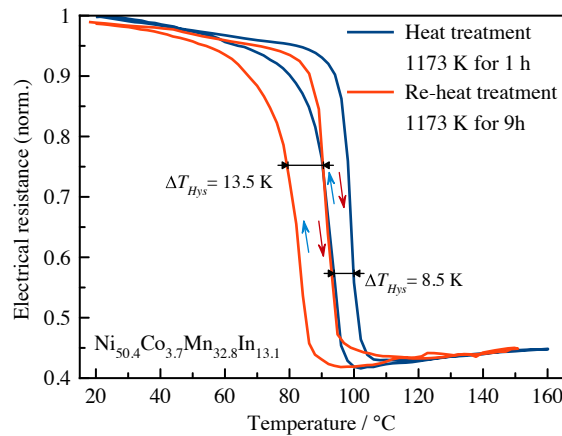


Figure 4.17: Temperature dependent electrical resistance of initial and re-heat treated  $\text{Ni}_{50.4}\text{Co}_{3.7}\text{Mn}_{32.8}\text{In}_{13.1}$  films.



## 5. FSMA-based Energy Harvesting

The aim of this chapter is to present the options of FSMA based thermal energy harvesting, making use of the materials intrinsic actuation capabilities and the thermomagnetic characteristics. The FSMA-based energy harvesting principles, validated in this work, are presented in detail. Table 5.1 lists the options, which are available to create FSMA-based thermal energy harvesting systems. Three categories can be distinguished for the design:

- thermal actuation principle to provide periodic heating/cooling,
- thermo- or mechanomagnetic transducing effect,
- method of energy conversion.

Table 5.1: Summary of actuation mechanisms, effects, and methods of energy conversion of FSMA-based energy harvesting. [90] © 2014 WILEY-VCH

Material	Thermal actuation / reset mechanism	Transducing effect	Method of energy conversion
FSMA films	Magnetostatic attraction / one-way SME	T-induced change of magnetic anisotropy	Faraday's law
	Magnetostatic attraction / elastic resetting	T-induced ferromagnetic transition	
	One-way SME / elastic resetting	Actuation induced induction	
	Two-way SME		

For FSMA harvesting, the first two thermal actuation mechanisms, shown in Table 5.1, are investigated in this work, combined with the transducing effect of actuation induced induction. The operation principles of these different energy harvesting systems, are explained in this chapter as well as the fabrication and properties of the energy harvesting demonstrators. They are characterized by their mechanical and thermal properties as well as their electrical output. Mechanical properties comprise the actuation frequency, displacement, stiffness, and actuation forces. Heating and cooling times, as well as thermal profiles, are described in thermal characterization sections. The electrical output chapters cover the induced current as well as the average and peak power output.

### 5.1. Basic Operation Principle of FSMA-based Energy Harvesting

Besides the one-way SME, described in Chapter 2.1.1.1, FSMA materials show a ferromagnetic transition, leading to thermomagnetic characteristics similar to the schematic curve depicted in Figure 5.1. This behavior is also shown in the material characteriza-

tion in Chapter 4.1. The material is ferromagnetic in martensitic and austenitic state, with slight changes in magnetization, up to the Curie temperature  $T_C$ . When approaching  $T_C$ , the magnetization drops to zero in a temperature interval  $\Delta T$ . This results in a large change of magnetization  $\Delta M$ . Because of the 2<sup>nd</sup> order ferro- to paramagnetic transition, the magnetization increases on cooling without any hysteresis.

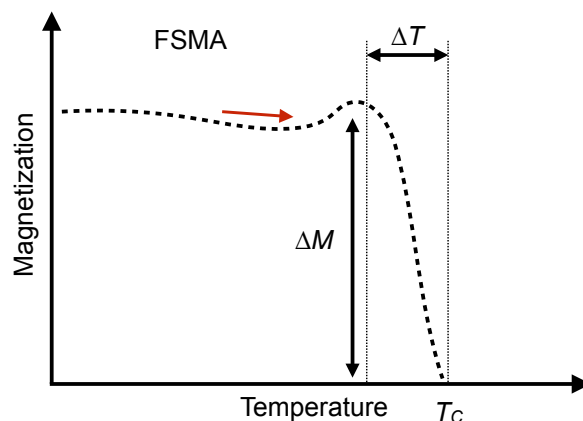


Figure 5.1: Schematic thermomagnetic characteristic of FSMA material. For clarity only the heating is shown.

This change in magnetization, combined with the one-way SME, can be used for actuation similar to the microscanner presented in Chapter 3.3.3. Figure 5.2 shows the basic principle of self-actuated thermal FSMA actuation, using temperature dependent magnetostatic attraction and resetting due to the one-way SME.

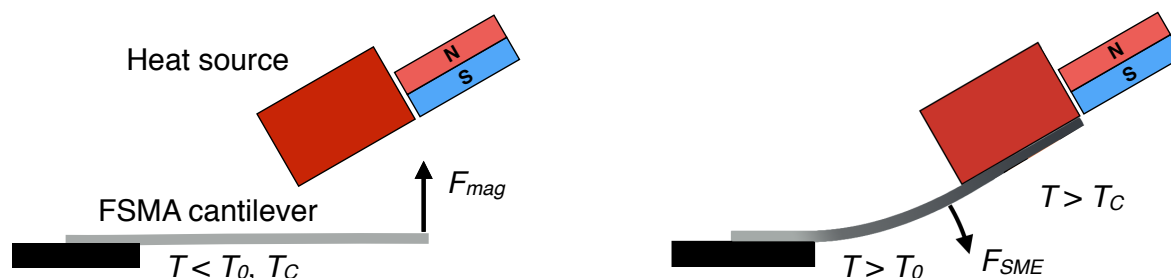


Figure 5.2: Schematic of FSMA based actuation.

In initial state, a FSMA cantilever, fixed on one end to a substrate, is in martensitic state below the transformation temperature  $T_0$  and below  $T_C$ . A permanent magnet, positioned above the cantilever, induces a magnetic attraction force  $F_{mag}$  on the cantilever, deflecting it towards a heat source which is located next to the magnet. On touching the heat source, the FSMA cantilever heats above  $T_0$  and  $T_C$ , leading to an increased reset Force  $F_{SME}$ , due to the one-way SME, and at the same time to a strong decrease of  $F_{mag}$ . These effects result in a reset movement of the FSMA cantilever. When the cantilever is in non-deflected position again, it cools below  $T_0$  and  $T_C$ , and a periodic bi-directional actuation is evoked. The following sections present several variations of this

basic self-actuation mechanism, including different methods for energy conversion.

## 5.2. FSMA-based Energy Harvesting using an External Pick-Up Coil

### 5.2.1 Operation Principle

The basic FSMA actuation principle is varied by attaching additional FSMA material on the front end of the FSMA-film cantilever. For energy conversion, a pick-up coil is placed around the FSMA-tip in initial state, as depicted in Figure 5.3. Self-actuation of the cantilever leads to a periodic movement of the FSMA-tip in and out of the pick-up coil, inducing a current according to Faraday's law.

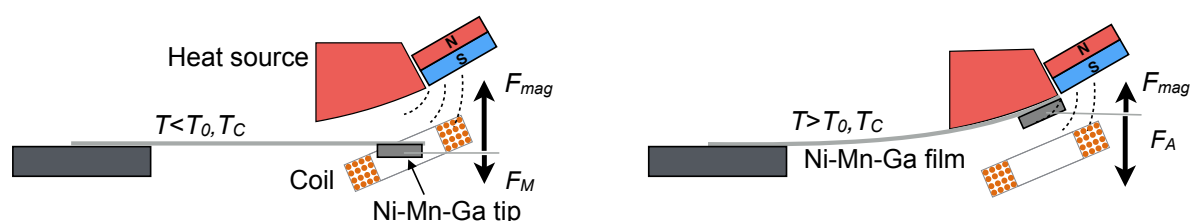


Figure 5.3: Schematic of a FSMA-based energy harvesting device using a stationary pick-up coil.

In this concept, the magnetic attraction force and the reset force can be adjusted separately by tailoring the thickness of the cantilever and the tip individually. Increasing the thickness of the FSMA-tip increases the magnetic attraction force, but also decreases the actuation frequency as the heating and cooling times increase. Besides FSMA also other ferromagnetic materials, showing a strong decrease of magnetization at  $T_C$  like ferrite, can be used as tip material.

### 5.2.2 Fabrication

In order to fabricate a demonstrator for FSMA-based energy harvesting, a setup consisting of a substrate holder, a regulated heat source, and a permanent magnet is build up. The cantilever is structured by lithography and wet-etching from Ni-Mn-Ga films using the fabrication method described in Chapter 2.5.3.

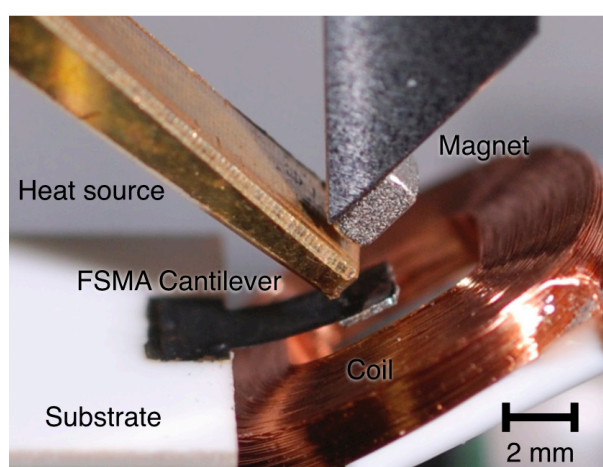


Figure 5.4: Picture of a first demonstrator for FSMA energy harvesting by using an external pick-up coil.

The thickness of the Ni-Mn-Ga films is 10  $\mu\text{m}$ . The investigated cantilever sizes are 4 x 2  $\text{mm}^2$  and 1.5 x 3  $\text{mm}^2$ . The pick-up coil, placed around the cantilever, is manufactured commercially (Jelonnek Transformatoren und Wickelgut GmbH). The wire diameter is 40  $\mu\text{m}$ . The number of windings is varied between 250 and 1000 and the inner size of the coil is 2.1 x 2.5  $\text{mm}^2$ . Different ferromagnetic materials are mounted on the tip of the cantilever. Sawed ferrite samples of 100 to 500  $\mu\text{m}$  thickness and single crystalline Ni-Mn-Ga foils of 200  $\mu\text{m}$  thickness with a size of approximately 1.5 x 2  $\text{mm}^2$  are used. Figure 5.4 shows a demonstrator device with all components. The different parts as heat source, magnet, coil, and substrate can be adjusted separately with respect to each other to find the best arrangement.

### 5.2.3 Mechanical Characterization

The demonstrator is first characterized by measuring stationary forces using the elastometer described in Chapter 2.4.4. In order to understand the bi-directional actuation, the magnetic attraction forces in ferromagnetic state ( $T < T_C$ )  $F_{ferro}$  and paramagnetic state ( $T > T_C$ )  $F_{para}$ , as well as the reset forces of the cantilever in both states ( $T < M_f$  and  $T > A_f$ ), have to be known. Figure 5.5 shows the experimental results of the force measurements and the calculated net force, dependent on the cantilever deflection.

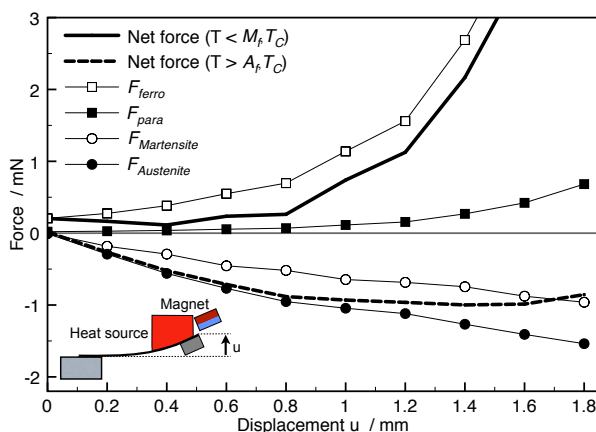


Figure 5.5: Experimental force-displacement characteristics for the FSMA harvesting device with an external pick-up coil under stationary conditions. [91] © 2013 IEEE

The net force is positive for temperatures below  $M_f$  and  $T_C$ , and is negative for temperatures above  $A_f$  and  $T_C$ . This guarantees a deflection of the cantilever towards the magnet in the cold state and a reset motion when it is heated above  $A_f$  and  $T_C$ .

Besides the stationary measurements, in-situ measurements of the displacement are performed by image tracking, described in Chapter 2.4.9. The heat source temperature is varied between 110 and 160  $^{\circ}\text{C}$  to investigate the working temperature range and temperature dependencies. For each temperature, the time-dependent deflection is measured, and the oscillation frequency is calculated as shown in the lower graph of Figure 5.6. For a heat source temperature of 130  $^{\circ}\text{C}$ , the deflection is exemplarily shown in the upper graph of Figure 5.6.

At a deflection of 0.5 mm, the cantilever tip touches the heat source and heats up for about 100 ms. After leaving the heat source the cantilever tip oscillates at a deflection of 1.2 mm, cooling down for about 400 ms. The stroke of the oscillation decreases from 800  $\mu\text{m}$  to about 100  $\mu\text{m}$  due to air damping. The resulting thermal frequency is about 2 Hz, while the measured oscillation frequency at this temperature is about 82 Hz, which is the maximum for an investigated temperature range of 110 to 160  $^{\circ}\text{C}$ . The frequency up-conversion of a low thermal frequency to a higher mechanical oscillation frequency leads to a much higher mechanical actuation duty cycle.

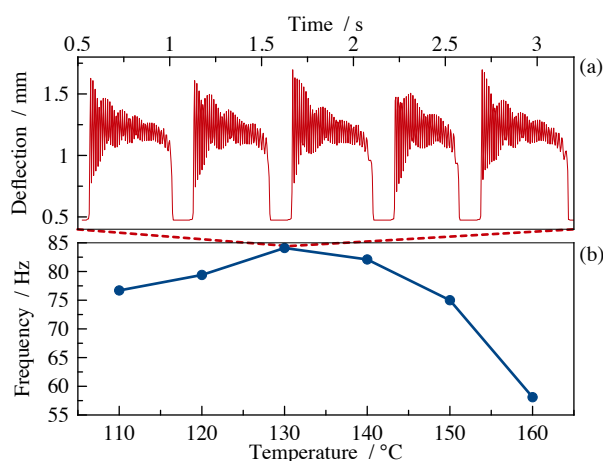


Figure 5.6: a) Time-dependent deflection for a heat source temperature of 130  $^{\circ}\text{C}$ . b) Operation frequencies of the FSMA harvesting device for different heat source temperatures.

The waviness of the declining oscillation amplitude that can be seen in the upper graph of Figure 5.6 is probably due to the nonlinearity of the magnetic attraction force and a limited time resolution of the high speed camera. Because of the changing temperature of the cantilever tip during oscillation, the magnetic attraction force increases while still being too small to fully deflect the cantilever tip again, resulting in a changing neutral position of the oscillation. Additionally, the time resolution of the image tracking is limited by the high speed camera shutter speed of 1/2000 s, leading to incomplete tracking.

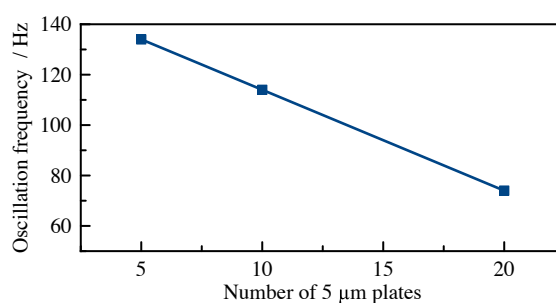


Figure 5.7: Oscillation frequency dependent on the number of FSMA plates at the cantilever tip.

The oscillation frequency is mainly determined by the eigenfrequency of the cantilever. This is revealed in Figure 5.7, showing the measurement of oscillation frequencies, which are derived from the frequency of the induced current, of three FSMA cantilevers

with a different amount of FSMA material attached to the cantilever front end.

Stacks of 5, 10, and 20 5  $\mu\text{m}$  thick FSMA films are applied on the tip of 5  $\mu\text{m}$  thick cantilevers with a 3 x 1.5  $\text{mm}^2$  size. The measured oscillation frequencies of these demonstrators decline from 134 Hz for the smallest stack to only 74 Hz for the stack of 20 films. This is expected from the dependence of the eigenfrequency on the tip mass, shown in Equation (28) in Chapter 7.3. The stiffness of the cantilever remains the same, while the mass increases with the stack size. However, a dependency proportional to  $\sqrt{1/m}$  is not clearly visible due to limited data and the additional dependence on magnetic attraction forces.

In order to examine the influence of the position of the magnet on the performance of the overall system, a measurement for five different magnet positions at a magnet orientation of about  $45^\circ$  is performed. At each position, the heat source temperature is varied between the lowest and highest value at which periodic actuation can be achieved. The different magnet positions M1 to M4 are depicted in the schematic of Figure 5.8. The magnet position  $M_{\text{opt}}$  is between the positions M2 and M3, which is found by experiment. Figure 5.8 shows the results of the thermal operation frequency of the overall heating and cooling cycles as well as the mechanical oscillation frequency. The mechanical oscillation frequency is derived from the alternating movement of the cantilever inside the pick-up coil, which is proportional to the frequency of the generated current.

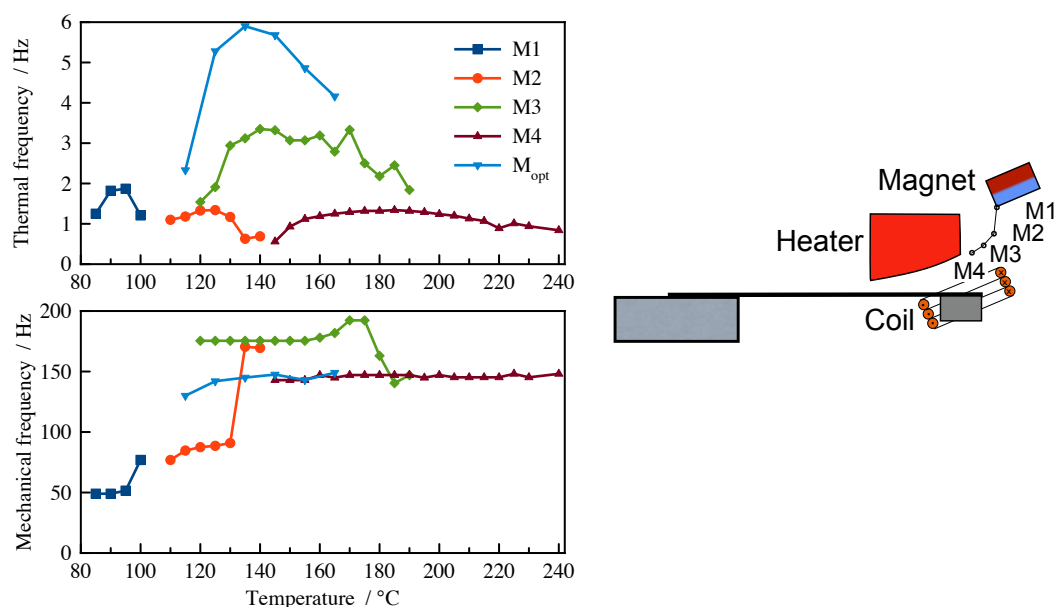


Figure 5.8: Influence of different magnet positions M1 to M4 (indicated in schematic) and heat source temperatures on operation and oscillation frequencies.  $M_{\text{opt}}$  is between M2 and M3.

The upper graph, depicting the thermal operation frequency, shows that the temperature operating-range varies for each magnet position. At position M1, actuation can only be achieved in a small range from 85 to 100  $^\circ\text{C}$ , close to the Curie temperature  $T_C$

of the Ni-Mn-Ga tip. The actuation temperature range, as well as the minimum working temperature, increase with a closer position of the magnet to the cantilever tip. At M4, the minimum temperature for actuation is 145 °C, but the working temperature range is very large, up to 240 °C. Additionally, for every position of the magnet an optimal heat source temperature can be identified, at which the operation frequency is at maximum. For position M1 to M4 it increases step-wise as follows: 95 °C, 125 °C, 135 °C (for  $M_{opt}$ ), 140 °C, and 180 °C. The overall trend of the thermal operation frequencies shows that for positions of the magnet far from the cantilever tip as well as very close to it, frequencies are relatively low, between 1 and 2 Hz. For the magnet position  $M_{opt}$ , located between M2 and M3, the thermal frequency is at a maximum of almost 6 Hz at a heat source temperature of 135 °C. This is probably due to a good match of cooling and heating times needed for a sufficient change in magnetization and reset forces. The lower graph of Figure 5.8, showing the mechanical oscillation frequency, indicates that the frequency is not only influenced by the eigenfrequency of the cantilever, but also by the position of the magnet and therefore the magnetic attraction forces and slightly by the temperature of the heat source. Especially in the temperature range of 80 to 150 °C, the oscillation frequency increases steadily. This could be due to a larger part of the cantilever transforming to the austenitic phase, which has a higher Young's modulus than the martensitic phase, affecting the cantilever stiffness. The abrupt change of oscillation frequency at position M2 and 130 °C is likely induced by a higher oscillation amplitude of the cantilever, leading to a periodic contact of the cantilever with the edge of the pick-up coil. This evokes a higher eigenfrequency, as the length of the oscillating part of the cantilever is reduced. The changes of the oscillation frequency at position M3 is presumably due to a small change of position of the pick-up coil, leading to a different active length of the oscillating cantilever, and therefore to a change in the frequency. At the position M4, the frequency stays constant at about 150 Hz.

These results show the applicability of frequency up-conversion from a relatively low thermal operation frequency of only a few Herz to a mechanical oscillation frequency, suitable for electromagnetic energy conversion.

#### 5.2.4 Thermal Characterization

In-situ thermography is performed using an infrared camera system in order to investigate the time-dependent temperature evolution in ferrite and Ni-Mn-Ga tips. The temperature of the ferrite tip changes from about 130 °C at the heat source to 110 °C when oscillating in the air, as can be seen in Figure 5.9 (left). This temperature change matches the Curie temperature of the ferrite at 125 °C very well. In order to have the best actuation, the heat source is heated to 150 °C during the investigation of the ferrite tip. The Ni-Mn-Ga single crystalline tip has a lower Curie temperature of only about 95 °C. Therefore, a lower heat source temperature of 130 °C is sufficient to achieve good actuation. The measurement of the temperature change of the Ni-Mn-Ga tip is

only reliable when in contact to the heat source, as the very thin tip of 200  $\mu\text{m}$  moves too quickly when oscillating. Therefore, the infrared camera cannot measure the absolute temperature change because the images are too blurred, as can be seen in Figure 5.9 (right).

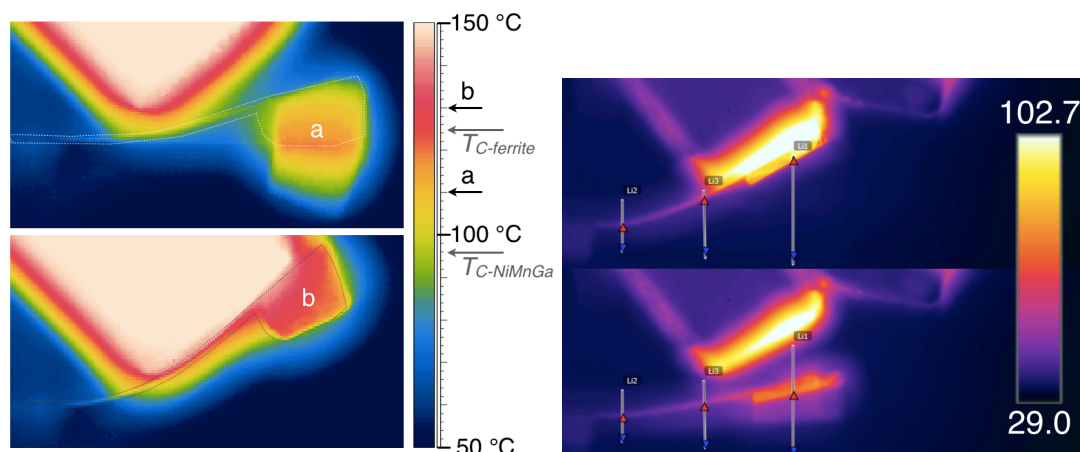


Figure 5.9: Time-resolved in-situ infrared thermography of a demonstrator device with ferrite tip (left) and Ni-Mn-Ga tip (right) during oscillation. The cantilever size is 2 x 4 mm<sup>2</sup>. [91] © 2013 IEEE

### 5.2.5 Electrical Output

The electrical output is characterized by connecting the external pick-up coil to a current amplifier as described in Chapter 2.4.5. The moving ferromagnetic tip induces a current in the external pick-up coil according to Faraday's law. Figure 5.10 shows a typical time-resolved current signal of a 10  $\mu\text{m}$  thick Ni-Mn-Ga cantilever with a size of 2 x 4 mm<sup>2</sup> and a Ni-Mn-Ga tip.

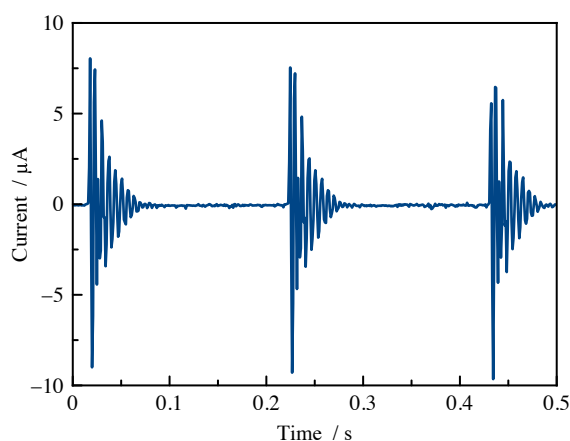


Figure 5.10: Time-resolved electrical current signal in the pick-up coil for a cantilever of 2 x 4 mm<sup>2</sup> size with a Ni-Mn-Ga tip. [91] © 2013 IEEE

The current signal corresponds to the deflection course shown in Figure 5.6. During heating, no current signal is induced. Only when moving away from the heat source, the mechanical oscillation of the magnetic material with respect to the pick-up coil leads to generation of an electric current. The induced current shows peaks of about

10  $\mu\text{A}$ , corresponding to an average power of 0.54 nW and a power density of about  $0.8 \mu\text{W}\cdot\text{cm}^{-3}$ .

Investigating the influence of different pick-up coils, measurements with 200, 500, and 1000 windings coils are performed. Two different cantilevers consisting of Ni-Mn-Ga films produced with a sputtering power of 50 W and 200 W are used. A single crystalline Ni-Mn-Ga foil of 200  $\mu\text{m}$  thickness is mounted on each cantilever tip. For each pick-up coil a load resistor matching the internal resistance is used to insure optimal power output. Figure 5.11 summarizes the measurement results, showing only a small decrease of the induced current for coils with less turns, but increasing power for coils with a higher number of windings. This is due to the higher load resistance.

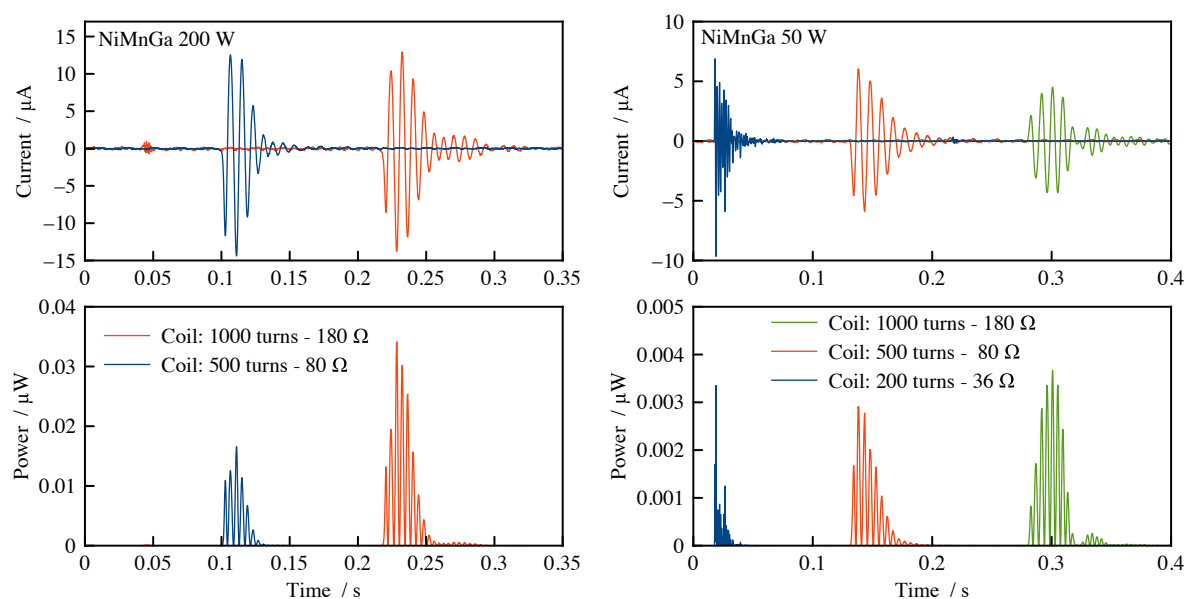


Figure 5.11: Current and power output of two cantilevers consisting of Ni-Mn-Ga films (sputtered with 200 W and 50 W power). Mounted on the tip is a  $2 \times 1 \text{ mm}^2 \times 200 \mu\text{m}$  single crystalline Ni-Mn-Ga foil. The heat source temperature is  $140 \text{ }^\circ\text{C}$ .

Regarding the time-dependent current and power signals, as shown in Figure 5.11, it can be seen that the current amplitude first increases and then decreases. As the amplitude of the cantilever deflection only decreases, this effect is not due to the mechanical movement, but due to a combination of the magnetization change in the material and the mechanical oscillation. When the material cools down due to air cooling, its magnetization increases, and therefore the effect of inducing a current in the pick-up coil according to Faraday's law increases. Further mechanical oscillating is damped by the air and the non-elastic parts of the FSMA cantilever, and the amplitude decreases, leading to a decreased velocity of the ferromagnetic tip movement in the pick-up coil. This leads to a decreasing induced current. Therefore, the induced signal is a superposition of the increasing magnetization and the decreasing amplitude, leading to first an increase of induced current and then a decrease.

As already shown in Chapter 5.2.3, the overall system performance is strongly depen-

dependent on the position of the magnet. Figure 5.12 shows the maximum induced currents for five different magnet positions. The graph shows a large increase of the maximum current if the magnet is positioned closer to the cantilever tip. This is due to a higher magnetic field in the pick-up coil, and thereby a higher magnetization change induced by the ferromagnetic tip, oscillating inside the coil. The data corresponds to the frequency measurements in Figure 5.8. It can be seen, that the optimal magnet position  $M_{opt}$  is very favorable for high thermal operation frequencies, but has only a relatively low maximum current output compared to the magnet positions M3 and M4, closer to the magnet. The proximity to the magnet provides larger magnetizations in the FSMA tip, and thereby increases the electromagnetic induction effect.

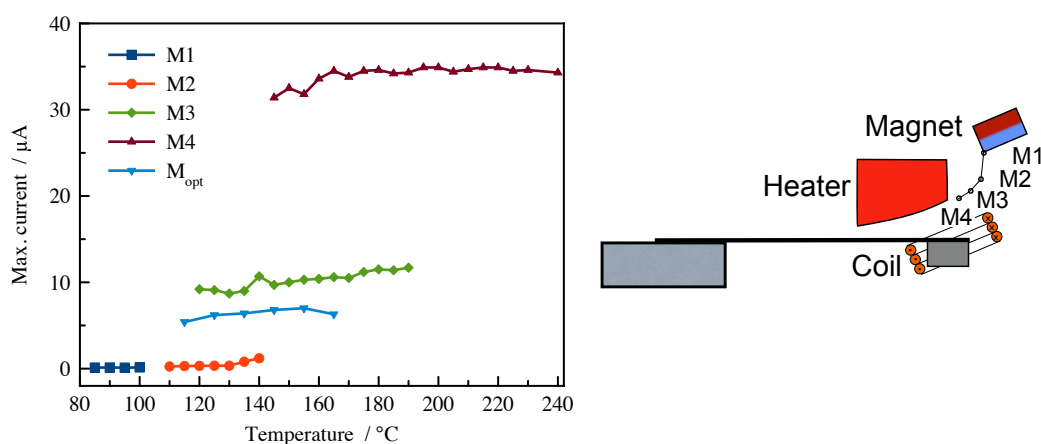


Figure 5.12: Maximum induced current for different magnet positions M1 - M4 (indicated in the schematic).  $M_{opt}$  is located between M2 and M3.

### 5.2.6 Conclusions

The results of the FSMA-based energy harvesting device using an external pick-up coil provides important insights. The principle of frequency up-conversion of low thermal operation frequencies allows to harvest electrical energy from a temperature gradient using ferromagnetic transitions. However, the duty cycle of the electrical power output is limited. This is mainly because the heating and cooling times do not match the actuation frequency, leading to time periods in which the cantilever rests at the heat source to heat, or in initial position to cool.

Another important result is the limited suitability of an external pick-up coil. On the one hand, the magnetization of ferromagnetic material, moving in the coil, is far from its maximum, due to the proximity to its  $T_C$ . On the other hand, the magnetic field cannot be maximized because of the distance of the permanent magnet to the pick-up coil. Also the difficulties in the setup - positioning the pick-up coil and allowing for a free actuation of the cantilever - suggest to think on alternatives to the external pick-up coil.

### 5.3. FSMA-based Energy Harvesting using an Integrated Microcoil

#### 5.3.1 Operation Principle

The new design described here comprises the FSMA-cantilever, a heat source, a permanent magnet, and a microcoil attached to the front end of the cantilever, as depicted in Figure 5.13. The actuation principle is the same as for the basic bi-directional FSMA actuation principle. In order to decrease the heating and cooling time constants to enable faster actuation compared to the energy harvesting demonstrator described in Chapter 5.2, no additional FSMA-material is attached to the FSMA-cantilever tip.

A new energy-transducing mechanism is introduced, based on Faraday's law as well. Instead of inducing a current by moving magnetic material inside an external pick-up coil, the new energy transducing mechanism is based on a microcoil moving in the magnetic field gradient of the external permanent magnet. This overcomes the problem of low magnetization of FSMA material due to its proximity to  $T_C$ . The electrical contact of the microcoil is done either by using a double beam structure of the cantilever as electrical conduction lines, or by using thin copper wires, fixed to the substrate.

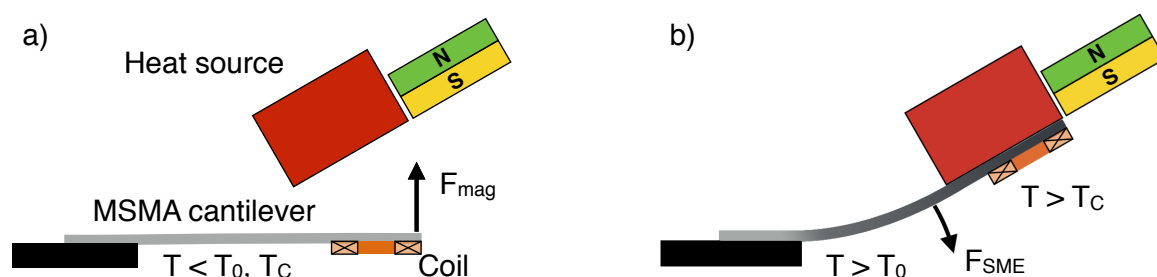


Figure 5.13: FSMA-based Harvesting principle using an integrated microcoil attached to the tip of the FSMA-cantilever. [87] © 2015 IEEE

#### 5.3.2 Fabrication

Wet-etched Ni-Co-Mn-Ga cantilevers with a size of  $2 \times 4 \text{ mm}^2$  are fabricated by lithography and wet-chemical etching. They are mounted by adhesive bonding at one end to a  $500 \text{ }\mu\text{m}$  thick  $\text{Al}_2\text{O}_3$  substrate. The thickness of the sputtered Ni-Co-Mn-Ga (FSMA-material) is about  $5 \text{ }\mu\text{m}$ . A manually fabricated microcoil with a wire diameter of  $15 \text{ }\mu\text{m}$  is fixed on the tip of the cantilever by adhesive bonding. The fabrication of the coils is described in Chapter 2.5.5. The wires are then electrically connected to the substrate with an electrically conductive adhesive. From the substrate they are connected to the load resistance and the measurement setup. The number of turns of the microcoil is varied between 100 and 400. The size of the coil with 100 turns is approximately  $2 \times 1.5 \text{ mm}^2$ , with a thickness of about  $200 \text{ }\mu\text{m}$ . The external setup, including substrate holder, heat source, and magnet, is the same as for the FSMA harvesting device with an external pick-up coil. Figure 5.14 shows a first demonstrator without heat source and magnet, comprising the FSMA cantilever and the microcoil, mounted

on its tip. The thin copper wires are the electrical interconnections between coil and substrate.

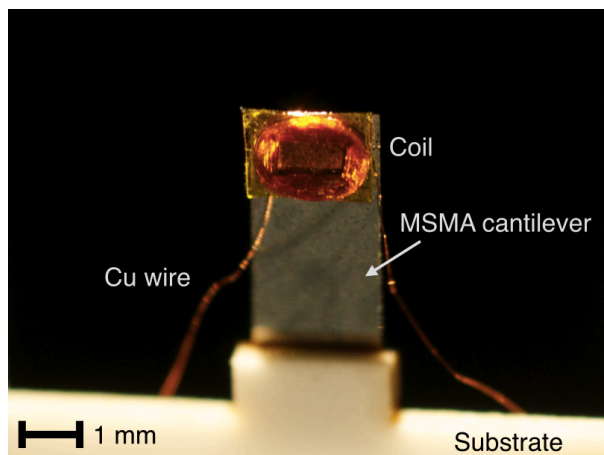


Figure 5.14: FSMA-based energy harvesting demonstrator using an integrated microcoil. [87] © 2015 IEEE

### 5.3.3 Mechanical Characterization

A laser triangulation sensor, described in Chapter 2.4.10, is used to measure the mechanical movement of the FSMA-based energy harvesting device with integrated microcoil. The sensor is placed in line of the cantilever-tip movement. Figure 5.15 shows the time-resolved displacement of the device for a heat source temperature of 170 °C.

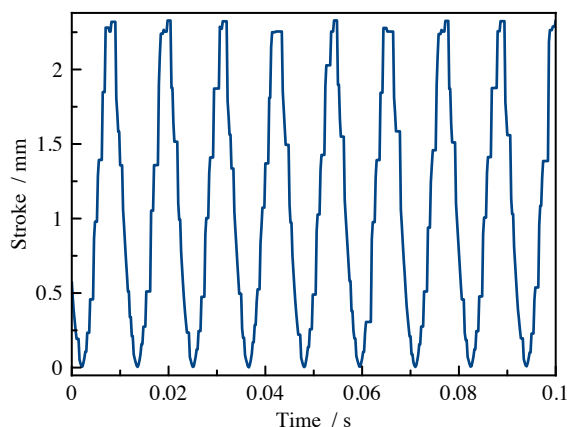


Figure 5.15: Time-dependent displacement measurement of the FSMA-based energy harvesting device using an integrated microcoil.

The maximum stroke is about 2.3 mm at a frequency of approximately 87 Hz. Most importantly, the oscillation amplitude is not declining, as it has been observed for the FSMA-based energy harvesting device using an external pick-up coil. The duty cycle of actuation is therefore almost 100%. Heating of the Ni-Co-Mn-Ga cantilever happens when approaching the heat source, while elsewhere the cantilever cools by convection and heat conduction through the cantilever. The resulting high thermal oscillation frequency is mainly due to strongly reduced heating and cooling times, as only material of

5  $\mu\text{m}$  thickness needs to heat up and cool down. This has to be compared to ferromagnetic tips of 50 to 500  $\mu\text{m}$  thickness in the FSMA-based energy harvesting devices using an external pick-up coil. Equation (15) in Chapter 7.1 shows the linear correlation of the thermal mass of the active material and the heating-/cooling time. As the thermal mass is linearly dependent on the thickness of the FSMA film, 10 to 100 times shorter heating and cooling times are expected than before. For the FSMA-based energy harvesting device using an external pick-up coil they are 100 and 400 ms, respectively. Therefore, it can be assumed that the thermal operation frequency matches the mechanical oscillation frequency. Besides the thermal operation frequency also the amplitudes are higher than in devices based on an external coil. This is due to the thinner cantilever films, enabling larger deflections at slightly smaller magnetic attraction forces because of a reduced cantilever stiffness (see Chapter 7.2).

Figure 5.16 shows the correlation of temperature-dependent operation frequency and stroke. Both, the operation frequency as well as the maximum stroke, are dependent on the heat source temperature. The operation frequency, shown in the upper graph, starts with approximately 125 Hz at 120 °C, and decreases rapidly to below 90 Hz at 140 °C, settling down to 82 Hz for 160 to 220 °C. The stroke of the cantilever tip increases steadily up to a heat source temperature of 200 °C. From 210 °C onwards, the actuation is not stable anymore, and periods of actuation with only small or decreasing amplitudes occur. This leads to decreasing maximum displacements.

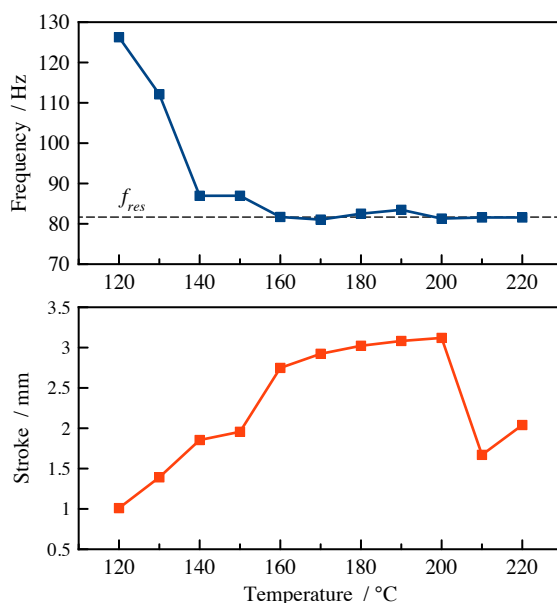


Figure 5.16: Operation frequency and stroke of the FSMA-based energy harvesting device using an integrated microcoil as a function of the heat source temperature.

The high frequency at lower heat-source temperatures correlates with a small stroke of only 1 mm. Probably, the magnetization change of the cantilever, and therefore the nonlinear magnetic attraction force, is predominant in the range of heat-source temper-

ature of 120 to 140 °C. From 140 °C on, the operating frequency stays almost constant. This frequency matches approximately the eigenfrequency of the cantilever. However, the stroke increases further until a heat source temperature of 200 °C is reached. As will be explained in Chapter 5.3.4, this is due to the need for sufficient cooling by forced convection. By optimizing the magnet and heat source positions, higher resonance frequencies of above 90 Hz can be achieved. However, the corresponding amplitudes are lower as will be described below.

### 5.3.4 Thermal Characterization

Figure 5.17 shows the temperature profile, measured by infrared thermography, along a self-actuated cantilever without an attached microcoil. The heat source temperature is set to approximately 140 °C. The variable  $x$  describes the position along the cantilever, starting from the tip at 0 mm until 3.25 mm, which is close to the fixation of the cantilever at 4 mm. The temperature drop between 0 and 0.5 mm is due to oscillation of the cantilever tip, causing a blurred thermography image. Between 0.5 and 2 mm, the temperature is almost constant at 105 °C. This area is almost identical to the part of the cantilever which is in contact to the heat source and where the microcoil would be attached. From 2 mm on, the temperature decreases towards the fixation of the cantilever due to heat conduction through the fixation. During oscillation, the measured temperature of the cantilever back only varies in a small range, not visible in the measurement setup. This is on the one hand because the measurement method of the used infrared camera system is not optimal for tracking fast temperature changes. On the other hand, it also has to be considered that the overall change of temperature in the cantilever tip is small, and only a partial transition from the ferro- to paramagnetic state provides sufficient magnetization change for actuation. It is assumed from the oscillation time that the temperature change is in the range of 2 K.

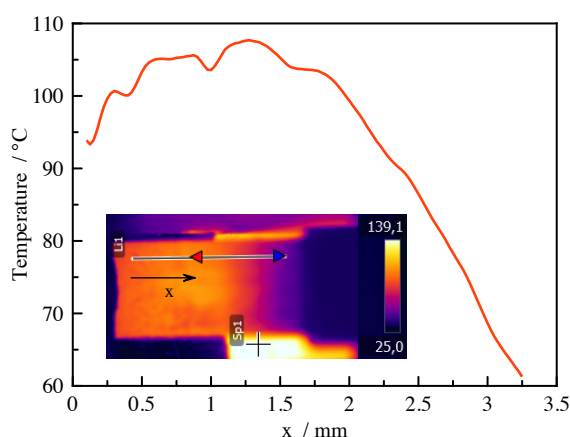


Figure 5.17: Temperature profile along the cantilever at a heat source temperature of about 140 °C.

An additional measurement of the average tip temperature, dependent on the heat source temperature, is performed to further characterize the thermal behavior of the

FSMA-based energy harvesting device using an integrated microcoil. The results are shown in Figure 5.18. Starting at a heat source temperature of 50 °C, the tip temperature follows the heat source temperature almost exactly, as the cantilever tip is in direct contact to the heat source. At approximately 100 °C, the tip temperature saturates and increases only slightly. Observations indicate that this is due to a partial release of the tip from the heat source, decreasing the thermal contact. Starting from 120 °C, the cantilever tip moves away from the heat source and starts oscillating. During oscillation, the average tip temperature stays almost constant at 105 °C. The inset of Figure 5.18 shows the infrared image at a heat source temperature of 145 °C.

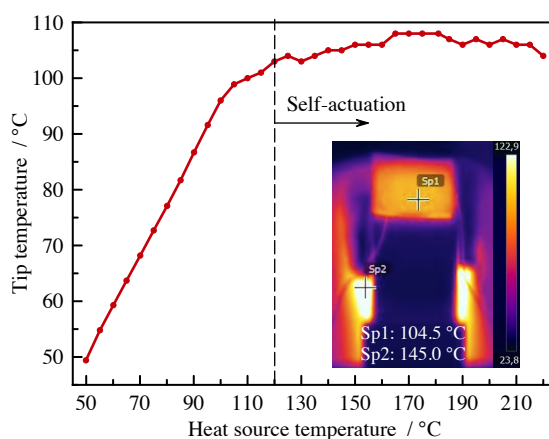


Figure 5.18: Thermography of the average tip temperature at different heat source temperatures.

The tip temperature stays almost constant below 110 °C for increasing heat source temperatures up to 220 °C. This significant cooling effect is achieved due to self-actuation with increasing oscillation amplitudes, as was already shown in Chapter 5.3.3, and a change of the oscillation center position away from the heat source. For a larger stroke the active cooling by air convection increases. This self-tuning allows a broad temperature operation range, keeping the tip-temperature at an almost constant level.

### 5.3.5 Electrical Output

Due to the large amplitudes and the high frequency of the FSMA cantilever, the induced current of the FSMA-based energy harvesting system using an integrated microcoil is much higher than in devices with an external pick-up coil. Additionally, the microcoil is passing directly in the magnetic field gradient of the permanent magnet. This is favorable compared to a ferromagnetic tip oscillating in an external pick-up coil. The magnetic field gradient in this setup provides a similar maximum changing magnetic field in the microcoil as the magnetized cantilever tip in the external pick-up coil, however the losses due to the air gap of the external pick-up coil are smaller. Additionally, this setup enables electromagnetic induction throughout the whole cantilever-tip movement, compared to the limited immersion in the pick-up coil of the magnetic cantilever tip. This leads to induced currents of approximately 100  $\mu\text{A}$  as shown in Figure 5.19.

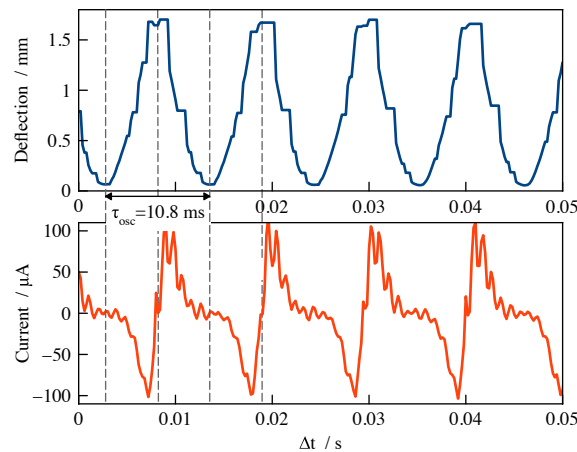


Figure 5.19: Deflection and corresponding induced current of the FSMA harvesting system with a microcoil.

The induced current corresponds well to the displacement measurements, as indicated by dashed lines. At zero and maximum deflection, the induced current is zero, as there is no movement of the coil at the turning points. When the cantilever is closest to the heat source and the external magnet, the induced current is at its maximum just before and after the maximum deflection. This is because the magnetic field gradient, which the microcoil experiences, is higher close to the external magnet. Near zero deflection, the induced current is relatively small due to the distance of the microcoil to the magnet and the smaller magnetic field gradient.

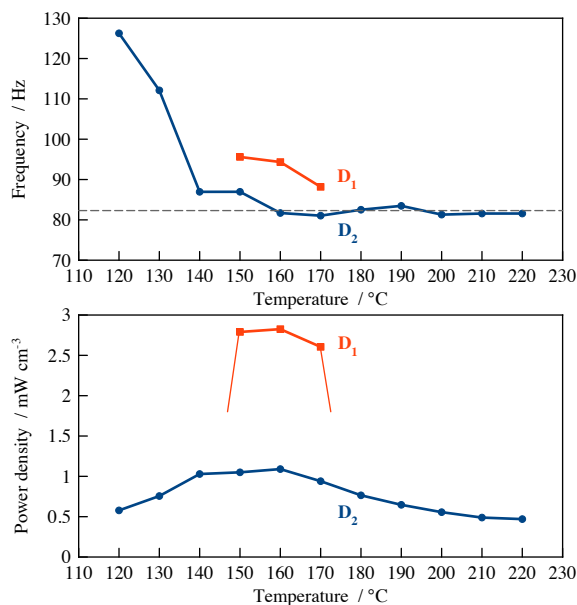


Figure 5.20: Correlation of the average power output and the operation frequency of the FSMA harvesting device with microcoil.  $D_1$  and  $D_2$  indicate two magnet positions optimized for maximum power and large actuation temperature range, respectively.

Figure 5.20 shows the correlation of the average power density of the FSMA harvesting device with the operation frequency, dependent of the heat source temperature. For a

magnet and heat source position ( $D_2$ ), optimized for a large actuation temperature range from 120 to 220 °C, a maximum of about  $1 \text{ mW}\cdot\text{cm}^{-3}$  at a heat source temperature of 160 °C is found. This is three orders of magnitude higher than the average power density of the FSMA-based energy harvesting device using an external pick-up coil.

The increase of power in the temperature interval of 120 to 150 °C despite the decrease of frequency can be explained by increasing oscillation amplitudes. This leads to a higher velocity of the microcoil in the magnetic field gradient, resulting in higher induced currents. After reaching a maximum at 160 °C, the power output decreases again even though the frequency stays the same. This can be explained by the shifting of the oscillation center position further away from the heat source and thereby from the magnet. The almost constant amplitudes of the cantilever and the constant tip temperature shown in Figure 5.16 and Figure 5.18 affirm this explanation.

By optimizing the heat source and external magnet position ( $D_1$ ) the output power can even be increased to almost  $3 \text{ mW}\cdot\text{cm}^{-3}$ . However, the optimized positioning of the heat source and magnet leads to a limited actuation temperature range of only 150 to 170 °C. At the optimum heat source temperature of 160 °C with the optimum setup, the average electrical power output is calculated to be  $0.12 \text{ }\mu\text{W}$ .

### 5.3.6 Energy Harvesting Array

As described in Chapter 5.3.2, the electrical contact to the microcoil is established with a  $15 \text{ }\mu\text{m}$  thick copper wire between microcoil and substrate. This leads to a fairly complicated setup if several energy harvesting devices should be build up side by side. Therefore, a different fabrication method is evaluated, using the beams of a double beam cantilever as the electrical contact. Figure 5.21 shows a  $3 \times 1.5 \text{ mm}^2$  Ni-Co-Mn-Ga double beam cantilever on which the microcoil is electrically contacted to the beams by an epoxy silver glue. This setup facilitates larger arrays of FSMA-based energy harvesting devices using an integrated microcoil, as the harvesting device does not need any further interconnection to the substrate besides the cantilever itself.

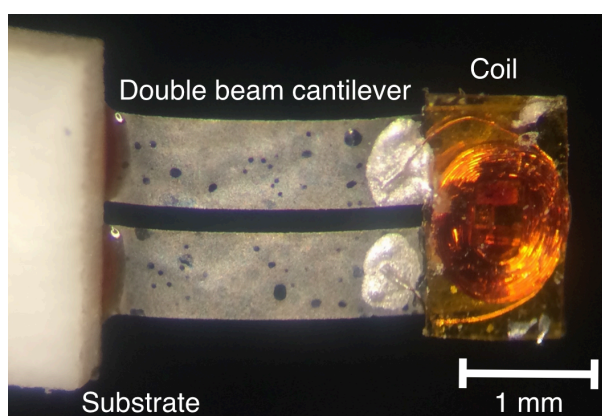


Figure 5.21: Double beam cantilever with a microcoil electrically contacted to the legs of the cantilever.

Figure 5.22 shows an array of six  $2 \times 4 \text{ mm}^2$  Ni-Co-Mn-Ga cantilevers, all with microcoils connected to the cantilever beams. Experiments with a heat source and an external magnet, suitable for simultaneous actuation of three cantilevers in a row, show that this scaling up is possible in principle. Challenges are the difference between the mechanical properties of the cantilevers and therefore differing optimal heat source and magnet positions. This can be overcome by an automated instead of manual fabrication of the harvesting devices. Actuating all six cantilevers and electrically connecting them could already lead to interesting power outputs of almost  $1 \text{ }\mu\text{W}$ , suitable for a variety of ultra low power applications.

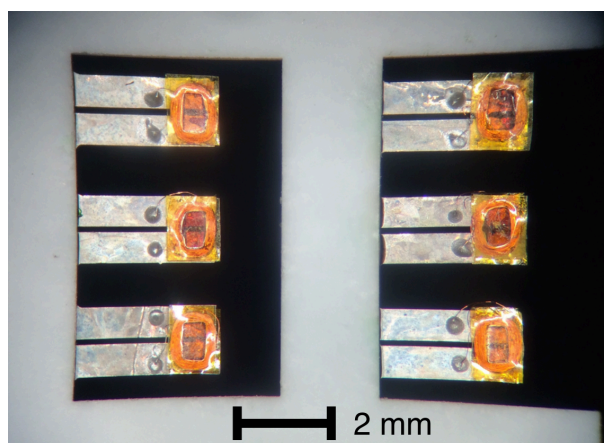


Figure 5.22: An array of six FSMA harvesting devices, each with a microcoil electrically connected via double beam cantilevers. [87] © 2015 IEEE

### 5.3.7 Conclusions

The results of the experiments with the FSMA-based energy harvesting device using an integrated microcoil show significant improvements, especially concerning operation frequency and power output. The reduction of active material leads to much faster heat transfer times. By matching the heat transfer times to the mechanical oscillation period, it is possible to generate continuous oscillations with a near optimum duty cycle. Yet, the amount of active material and the thickness of the cantilever are correlated in this design, not allowing for an independent tuning of mechanical and magnetic properties. Using an integrated microcoil, moving in the magnetic field gradient, contributes to the improved power output compared to the usage of an external pick-up coil. However, the electromagnetic conversion is limited when the cantilever tip is away from the heat source, because of a small magnetic field. This is due to the disadvantageous position of the magnet next to the heat source and due to the magnet geometry, allowing only for relatively small magnetic field gradients. Therefore, it would be very beneficial to increase the magnetic field and the magnetic field gradient by tuning the magnet geometry as well as the magnet position.

## 5.4. FSMA-based Energy Harvesting using a Magnetic Heat Source

### 5.4.1 Operation Principle

Taking into account the knowledge based on previous experiments, described in the chapters before, a modified FSMA-based energy harvesting demonstrator is designed. The FSMA-based energy harvesting device using a magnetic heat source comprises a brass cantilever, a FSMA film attached to its tip, a microcoil, and a magnetic heat source, as shown in Figure 5.23. The FSMA film, fixed on the tip of a non-magnetic cantilever, allows for the independent tuning of magnetic and mechanical properties. The actuation therefore differs from the basic FSMA-based actuation principle, as there is no active SME based reset force, but only a passive elastic reset force, counteracting the magnetic attraction force of the FSMA film.

The magnetic heat source is optimized in order to increase and improve the magnetic field gradient and its distribution. By combining the magnet and the heat source, the movement of the microcoil happens in the highest magnetic field gradient of the external magnet. The overall magnetic field is increased additionally by the longish magnet geometry, which provides a more favorable distribution of the magnetic field gradient. The goal of this setup is to increase the amplitude of oscillation of the electromagnetic conversion, as the microcoil moves in a large magnetic field gradient during its whole actuation period.

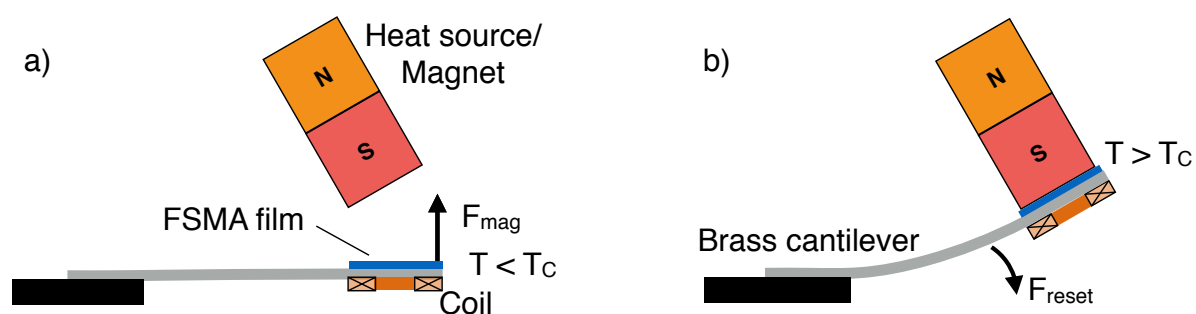


Figure 5.23: FSMA-based Energy Harvesting Concept using a magnetic heat source and a FSMA film attached to a non-magnetic brass cantilever.

### 5.4.2 Fabrication

Similar to the FSMA-based energy harvesting device using an integrated microcoil, also for this energy harvesting demonstrator a microcoil is fabricated according to the method described in Chapter 2.5.5. The size of the coil is slightly larger with an overall dimension of  $2 \times 3 \text{ mm}^2$  and a thickness of approximately  $400 \text{ }\mu\text{m}$ . The number of turns is 200. The microcoil is fixed on the bottom side of a brass cantilever tip, cut from a  $10 \text{ }\mu\text{m}$  thick brass foil. The cantilever size is  $3 \times 5 \text{ mm}^2$ . On the top of the cantilever tip a  $2 \times 2 \text{ mm}^2$   $\text{Ni}_{51.4}\text{Mn}_{28.3}\text{Ga}_{20.3}$  film of  $5 \text{ }\mu\text{m}$  thickness is attached. In Figure 5.24 the setup of the demonstrator is shown. For the magnetic heat source, a  $3 \times 3 \times 8 \text{ mm}^3$  CoSm

magnet with a maximum operation temperature of 350 °C is used. It is equipped with a small resistance heater and a temperature sensor. A good heat transfer coefficient is ensured by polishing the front side, which is in contact with the FSMA film on the cantilever tip.

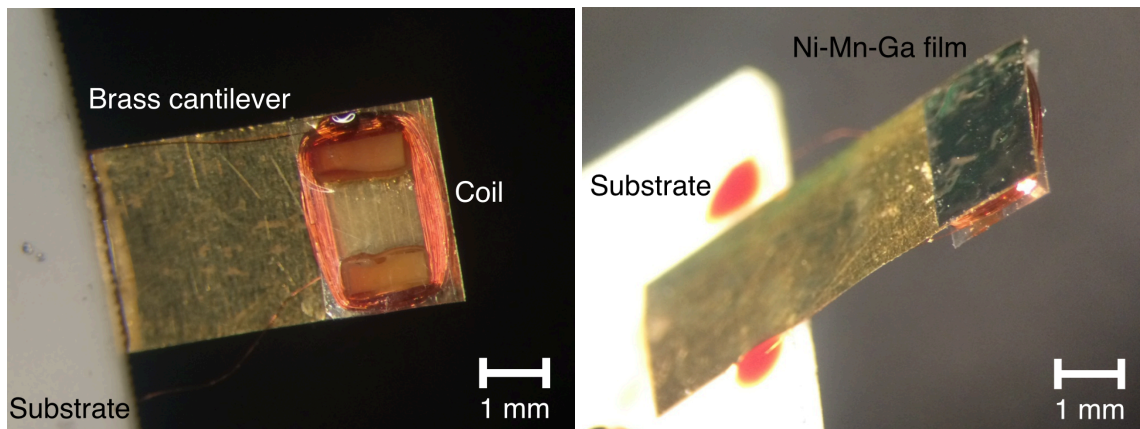


Figure 5.24: Fabrication of the FSMA harvesting demonstrator, based on a brass cantilever and a magnetic heat source.

### 5.4.3 Mechanical Characterization

First, the free oscillation of the cantilever is investigated, as shown in Figure 5.25. The negative displacement at the beginning of the oscillation is not complete, due to a misalignment of the laser beam and the large deflections of the cantilever tip. Therefore, the measurable maximum negative displacement is limited to -2.5 mm. For the decaying oscillation, a strong damping at high amplitudes, and a much lower damping at amplitudes below 1 mm can be identified. The quality factor is determined by

$$Q = 2 \cdot \pi \cdot \frac{E_{Cycle}}{E_{Loss}}, \quad (10)$$

whereas  $E_{Cycle}$  is the energy stored at a certain amplitude, and  $E_{Loss}$  is the energy loss, calculated from the amplitude decrease.

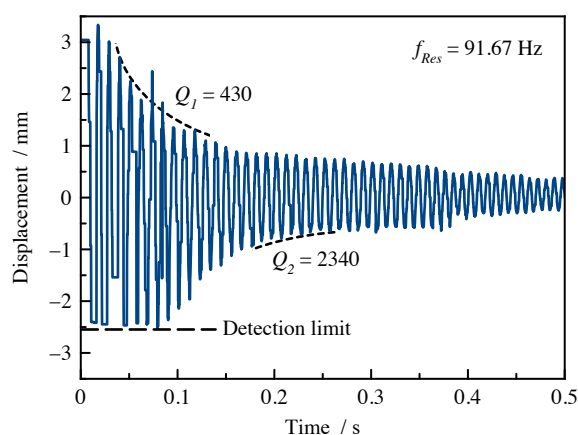


Figure 5.25: Decrease of the free oscillation of the brass cantilever with a microcoil at the tip. The resolution is limited at the lower maximum displacement due to a misalignment of the laser beam.

The quality factor  $Q_1$  for the fast decay is 430, while the oscillation at about 1 mm amplitude has a quality factor  $Q_2$  of 2340. The eigenfrequency is measured by Fast Fourier Transformation to be 91.67 Hz.

When actuated with the magnetic heat source near the optimum position, one millimeter above the neutral position of the cantilever, the oscillation of the cantilever tip becomes almost harmonic, as can be seen in Figure 5.26. The positive and negative displacement are almost the same and the frequency of 84 Hz is close to the eigenfrequency of the cantilever. At the heat source temperature of approximately 150 °C, no distinct heating time can be identified. It seems that a short impact on the heat source, not visible in the displacement measurement, is enough to transfer a sufficient amount of heat in order to keep the oscillation going.

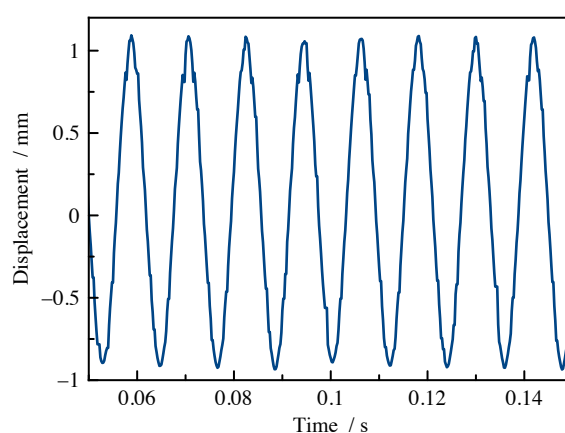


Figure 5.26: Mechanical displacement, measured with the laser distance sensor.

#### 5.4.4 Thermal Characterization

Thermal characterization of high frequency temperature changes with thermography becomes very challenging and partly impossible with the available measurement setup, described in Chapter 2.4.8. Therefore, a new technique, using a thin thermoelectric element of  $4.4 \times 4.4 \times 0.5 \text{ mm}^3$  size, is implemented to determine the heat flux through the sensor element. It is mounted directly on the magnetic heat source. The open circuit voltage of the thermoelectric sensor is measured with a high definition measurement unit, being capable of measuring very small changes in voltage and current. The sensing mechanism behind this principle is explained in more detail in Chapter 3.2.1. With the measurement setup it is possible to determine the heat flux through the heat source during actuation with a rate of 5000 Hz.

Figure 5.27 shows the combination of the measured heat flux, calculated from the thermoelectric sensor data, the open circuit voltage of the harvesting demonstrator, and the displacement, measured with the laser distance sensor. It can be seen that the heat flux increases abruptly at the maximum displacement of the cantilever (closest to the heat source), until the cantilever moves away. The heat flux then decreases to a base level until the cantilever touches the heat source again.

The change of heat flux is about 1.5 mW. Integrating the signal without the base level leads to the result that a net-heat of about 15  $\mu\text{J}$  per cycle is transferred. This value is a lower limit of heat transferred to the energy harvesting system and would account for a temperature change of the FSMA tip of only 0.19 K. The calculation does not take into account the parasitic heat loss, which is released during the whole time to the surrounding. This heat flux is about 90 mW, corresponding to the base level of the measured voltage on the thermoelectric sensor. Additionally, the time constant of the heat flux sensor may be too slow for an accurate measurement of the highly dynamic heat exchange at the magnetic heat source.

The electrical output and the mechanical oscillation amplitude (stroke) are not as high as in the setup without thermoelectric sensor because the sensor has a finite thickness of 0.5 mm and thus limits the actuation range of the cantilever. Only half of the amplitude is possible. In addition, the heat transfer coefficient is affected. It is therefore not possible to measure the heat flux during optimal actuation, limiting the interpretation of the results to a qualitative description of the harvesting system.

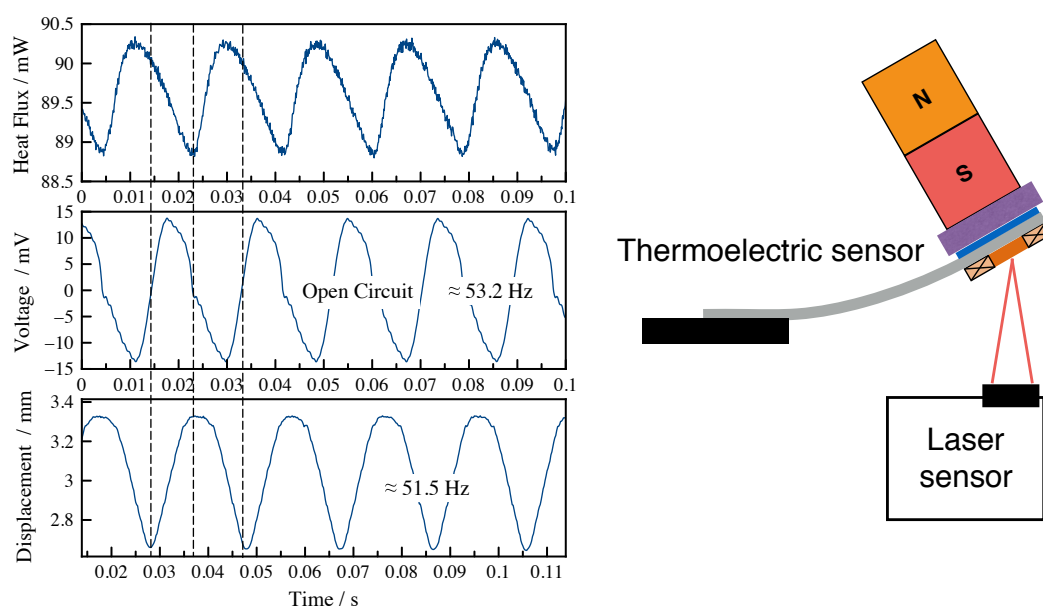


Figure 5.27: Heat flux measurement combined with the open circuit voltage of the harvester and its displacement.

#### 5.4.5 Electrical Output

The electrical output of the FSMA-based energy harvesting demonstrator using a magnetic heat source shows even higher duty cycles than the FSMA-based energy harvesting demonstrator using an integrated microcoil and an individual heat source. This is because the amplitude is not reduced as strongly, when the microcoil is at its turning point away from the magnet due to the larger magnetic field. The current signal for actuation at a heat source temperature of 150  $^{\circ}\text{C}$  is shown in Figure 5.28.

Besides the very high current amplitude of above 150  $\mu\text{A}$  at 220  $\Omega$  load resistance, the

induced current signal is very smooth and no break at the turning points of the cantilever can be identified. Only a slight decline in slope at the turning point away from the heat source is visible. This improvement is due to the integrated magnetic heat source, which facilitates a much more homogeneous magnetic field gradient during the complete actuation of the cantilever tip. The frequency of the induced current signal is 84.7 Hz. The average power, which can be calculated from the current signal, is found to be 2.38  $\mu\text{W}$  and the power density, derived from the used  $2 \times 2 \times 0.005 \text{ mm}^3$   $\text{Ni}_{51.4}\text{Mn}_{28.3}\text{Ga}_{20.3}$  film, is  $118.5 \text{ mW}\cdot\text{cm}^{-3}$ . This is a further significant increase by two orders of magnitude in average power and power density compared to the previous FSMA -based energy harvesting principles. A comparison to thermoelectric state-of-the-art energy harvesting devices is made in Chapter 8.3 to underline the importance of this result.

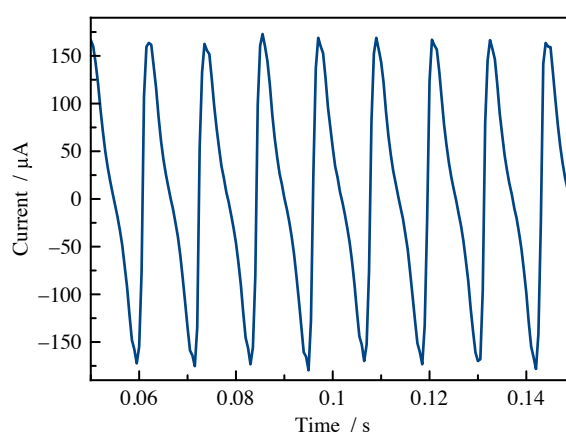


Figure 5.28: Electrical output of the FSMA harvesting device based on a brass cantilever and a magnetic heat source.

#### 5.4.6 Performance at Different Ambient Temperatures

The applicable temperature range of the FSMA-based energy harvesting device using a magnetic heat source is investigated by measuring the performance at different temperature differences  $\Delta T$  between ambient ( $T_{air}$ ) and heat source temperature ( $T_{source}$ ). As the heat source temperature has to remain above  $T_C$ , the temperature difference is reduced by increasing the ambient temperature. In order to do so, the whole setup is placed in an oven, where a temperature sensor close to the FSMA-based energy harvesting device measures the air temperature, while a second sensor monitors the heat source temperature. The ambient temperature is increased from 25 to a maximum of 70  $^{\circ}\text{C}$ , while the heat source temperature is adjusted between 135 and 100  $^{\circ}\text{C}$ . At high ambient temperatures, the heat source temperature had to be decreased to allow actuation, as otherwise the heat transfer and cooling time would not match sufficiently and actuation becomes non-periodic. Figure 5.29 shows the results of the measurement series. The electrical power decreases strongly by two orders of magnitude when the temperature difference  $\Delta T$  is below 30 K. For  $\Delta T$  below 50 K, no continuous actua-

tion is observed, as the heating and cooling times are increased strongly compared to larger temperature differences. For  $\Delta T > 50$  K, however, a continuous periodic oscillation can be measured. The frequencies are determined with Fast Fourier Transformation. From a temperature difference of 50 K on, frequencies of above 60 Hz are found in a wide temperature range. The system also shows the effect of self-tuning, allowing for a broad operation range with much larger temperature differences. The power output remains almost constant at about  $1 \mu\text{W}$  at  $\Delta T > 70$  K. It seems that larger temperature differences only have a minor effect on the oscillation frequency and heat transfer times. Therefore, it seems that for optimal actuation a temperature difference of about 70 K is sufficient and no direct correlation of temperature difference and power output is existent.

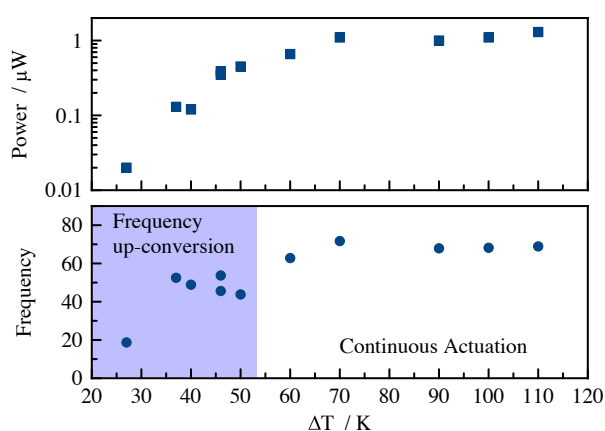


Figure 5.29: Electrical power output at different temperature differences.

#### 5.4.7 Conclusion

By adjusting the magnet geometry and individually tuning the mechanical properties of the cantilever and the active material, significant improvements in the overall power output can be achieved. Thereby, the tuning of the magnetic field had the largest influence on the enhanced electrical power output. The results of the demonstrator device of the FSMA-based energy harvesting device using a magnetic heat source show the importance of the optimization of magnetic and mechanical design in order to get an efficient conversion of ferromagnetic transitions to electrical energy, competitive to state-of-the-art thermal energy harvesting devices.

Further improvements of the material, especially the ratio of  $\Delta M/\Delta T$  would allow even more efficient FSMA-based energy harvesting devices. Besides the ferromagnetic transitions, also first order phase transformations show large abrupt changes in magnetization on heating and cooling. If hysteresis-widths decrease to a minimum, it is expected that similar actuation and energy harvesting can be realized, as will be discussed in the next chapter.

## 6. MSMA-based Energy Harvesting

This chapter presents MSMA-based thermal energy harvesting devices, which use the thermomagnetic properties of the materials for energy harvesting and self-actuation. As for FSMA-based energy harvesting systems, three design categories can be differentiated:

- thermal actuation principle to provide periodic heating/cooling,
- thermo- or mechanomagnetic transducing effect,
- method of energy conversion.

Table 6.1 lists possible design options for each category in order to create MSMA-based energy harvesting systems.

Table 6.1: Summary of actuation mechanisms, effects, and methods of energy conversion for MSMA-based energy harvesting. [90] © 2014 WILEY-VCH

Material	Thermal actuation / reset mechanism	Transducing-effect	Method of energy conversion
MSMA films	Direct harvesting - no actuation	T-induced change of magnetization	Faraday's law
	Magnetostatic attraction / elastic resetting	T-induced ferromagnetic transition	
	One-way SME / elastic resetting	Actuation induced induction	
	Two-way SME		

This chapter describes operation principles, fabrication, and properties of MSMA-based energy harvesting demonstrators, using the direct conversion of stationary MSMA film specimen as well as the magnetostatic attraction actuation mechanism. All three transducing effects listed in Table 6.1 are considered. Also, both methods of energy conversion are validated by energy harvesting demonstrator devices.

For all experiments, the  $\text{Ni}_{50.4}\text{Co}_{3.7}\text{Mn}_{32.8}\text{In}_{13.1}$  MSMA film material is used, as it shows superior thermomagnetic properties, as discussed in Chapter 4.2.

### 6.1. Basic Operation Principle of MSMA-based Energy Harvesting

MSMA materials are either in non-magnetic martensitic state below the transformation temperature  $A_s$  or in ferromagnetic austenite state above  $A_r$ . A schematic thermomagnetic characteristic is shown in Figure 6.1. At the transformation, a large, abrupt magnetization change ( $\Delta M$ ) in a small temperature range  $\Delta T$  happens. This effect of high  $\Delta M/\Delta T$  can be used directly by using the energy-transducing mechanism of tempera-

ture induced change of magnetization. It requires a dynamic heat source, showing a time-dependent change of  $T$ . The principle was first shown by [82] for bulk metamagnetic Ni-Co-Mn-Sn material. If no time-dependent heat source is available, an external actuation can be used to periodically heat and cool the material by moving the material between heat source and sink.

The change of magnetization, however, can also be used for self-actuation between a stationary heat source and a heat sink. By using this actuation mechanism, similar to the self-actuation presented in Chapter 5.1, MSMA-based energy harvesting is also applicable for most of common thermal energy harvesting applications. Possible implementations of working principles of the mentioned MSMA-based energy harvesting methods are described below.

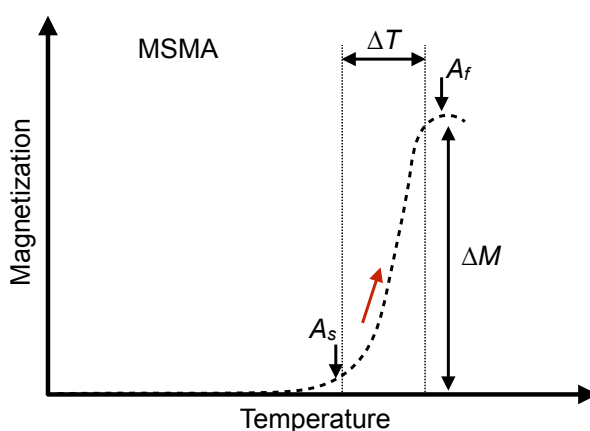


Figure 6.1: Schematic thermomagnetic characteristic of MSMA material. For clarity, only the characteristic upon heating is shown.

## 6.2. MSMA-based Direct Energy Harvesting by Laser Heating

### 6.2.1 Operation Principle

The principle of direct generation of electricity by heating a MSMA material comprises bulk MSMA material, a biasing permanent magnet, and a pick-up coil, as presented in ref. [82]. The MSMA material is placed above the magnet and inside the coil. Heating the sample induces a phase change in the material, leading to an abrupt change of magnetization. This change of magnetization in a biasing magnetic field induces a current in the coil according to Faraday's law.

In order to increase the electrical output of the MSMA-based direct energy harvesting, proposed by ref. [82], an important step is to increase the duty cycle. The heating time was about 40 seconds for the described sample, having a volume of about  $0.35 \text{ cm}^3$ . However, by using thin films, the heat transfer time can be improved significantly down to 10 ms for a sample of  $0.001 \text{ cm}^3$ , as it increases with the specimen thickness [82]. In order to heat the sample periodically, a laser is used as depicted in Figure 6.2. This en-

ables very fast cycling times. The adapted setup for thin films comprises the MSMA film, a microcoil, and a permanent magnet. The components are stacked onto each other. The MSMA film is coated with black carbon to guarantee a good absorption of the laser beam. Heating the MSMA film leads to a change of magnetization. This influences the magnetic flux through the microcoil, inducing a current according to Faraday's law.

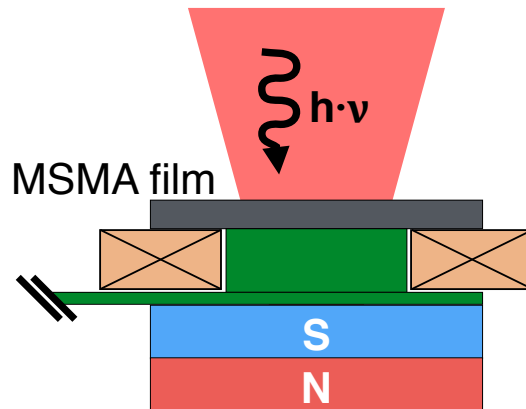


Figure 6.2: Schematic of MSMA-based direct energy harvesting using a laser heat source. [90] © 2014 WILEY-VCH

### 6.2.2 Fabrication

In order to investigate the direct conversion of heat to electricity of MSMA thin films, a demonstrator is build up consisting of a magnet, a pick-up coil, and a stack of MSMA thin films, coated with an absorption layer. The simulation software COMSOL 4.3 is used to optimize the position of the pick-up coil. The highest magnetization change within the pick-up coil is achieved for a setup in which the coil is placed in between the magnet and the MSMA film. Figure 6.3 shows the magnetic field density for a cold, non-magnetic MSMA film and a hot, ferromagnetic MSMA film.

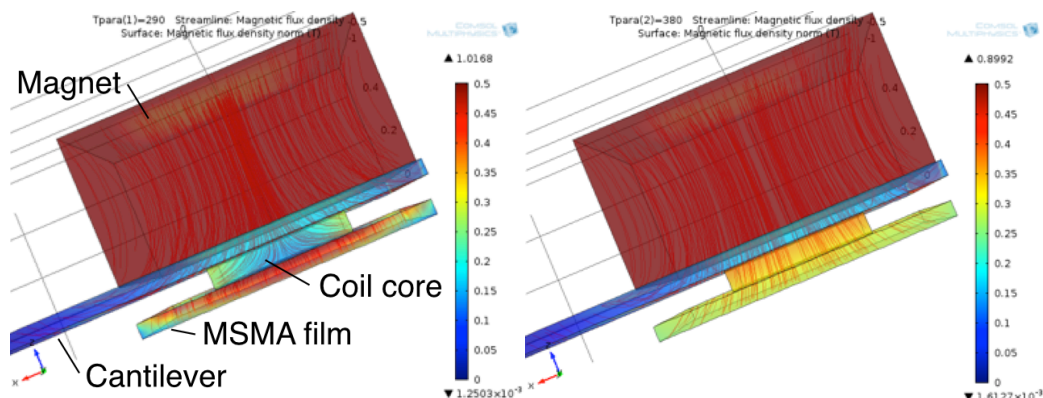


Figure 6.3: Simulation of magnetic field for a cold MSMA film (left) and a hot MSMA film (right).

The red cuboid is the permanent magnet. Below is a polyimide film, followed by a polyimide spacer with the pick-up coil placed around (not depicted), and the MSMA film. It can be seen that the magnetization in z-direction inside the coil core (polyimide spacer)

increases strongly from 0.18 to 0.33 T when the magnetization of the MSMA film increases by heating.

The MSMA film is first laser cut to  $2 \times 2 \text{ mm}^2$  pieces to fabricate the simulated setup. Because a single film of  $5 \text{ }\mu\text{m}$  thickness did not evoke a sufficient magnetization change for a measurable current signal, ten pieces are stacked using an epoxy adhesive. One side of the stack is coated with black carbon, dissolved in the epoxy adhesive. It is then fixed by adhesive bonding to the pick-up coil. A  $2 \times 2 \times 0.5 \text{ mm}^3$  magnet is mounted on the other side of the coil. Figure 6.4 shows the energy harvesting device for direct conversion. This setup is then placed below a heating laser. The Nd-YAG laser operates at 532 nm with a maximum power of 1.06 W, controlled by a LabView program. The surface-temperature of the black carbon coated MSMA film stack is measured by an infrared camera as described in Chapter 2.4.8.

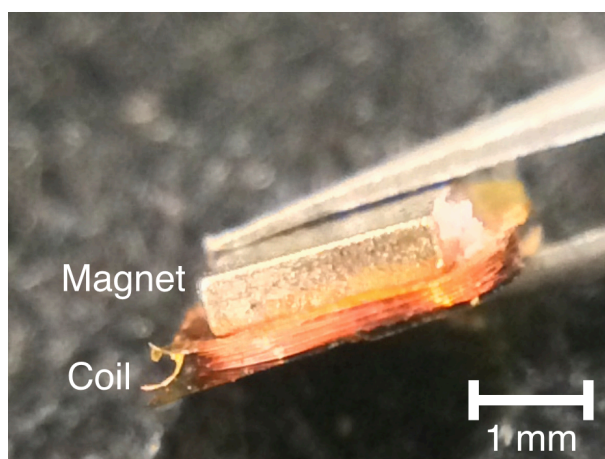


Figure 6.4: Demonstrator of the MSMA-based direct energy harvesting principle.

### 6.2.3 Results

Figure 6.5 shows the temperature change of the surface temperature and the corresponding induced current. Additionally, the magnetization change for the critical temperatures of martensitic and reverse phase transformation is depicted. The sample is first heated by low laser power for 500 ms. During a time of 1 s, the sample cools down by natural convection. Four different time phases can be differentiated. In phase I, the phase transformation from non-magnetic martensite to the ferromagnetic austenite takes place. This increase of magnetization leads to a first peak in the induced current signal. Further heating in phase II leads to a decreasing magnetization due to the ferro- to paramagnetic transition at  $T_C$ , leading to an opposite peak in the current signal. On cooling in phase III, the magnetization increases strongly, corresponding to the pronounced current peak. The last peak in the induced current is due to decrease of magnetization, while the MSMA material transforms back from ferromagnetic austenite to non-magnetic martensite in phase IV. On cooling, the martensitic transformation can be identified not only by the peak in the current signal, but also by a change of slope in the temperature curve, due to the latent heat released during the phase transformation.

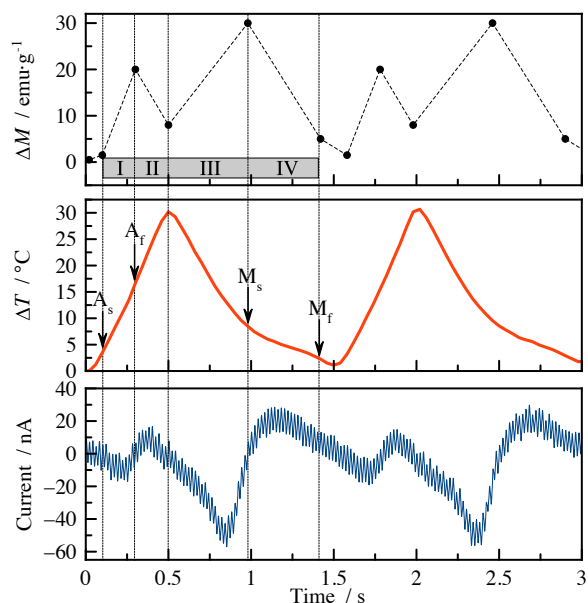


Figure 6.5: Correlation of magnetization change, measured surface temperature and the induced current for the demonstrator device shown in Figure 6.4, excited by laser heating. [90] © 2014 WILEY-VCH

Taking full advantage of the speed of laser heating, further experiments with a faster heating and cooling cycle are performed. The left graph in Figure 6.6 shows a cycle with 15 ms heating time and 85 ms cooling by convection. The right graph shows the experiment for an even shorter duration of heating and cooling of 5 and 45 ms, respectively.

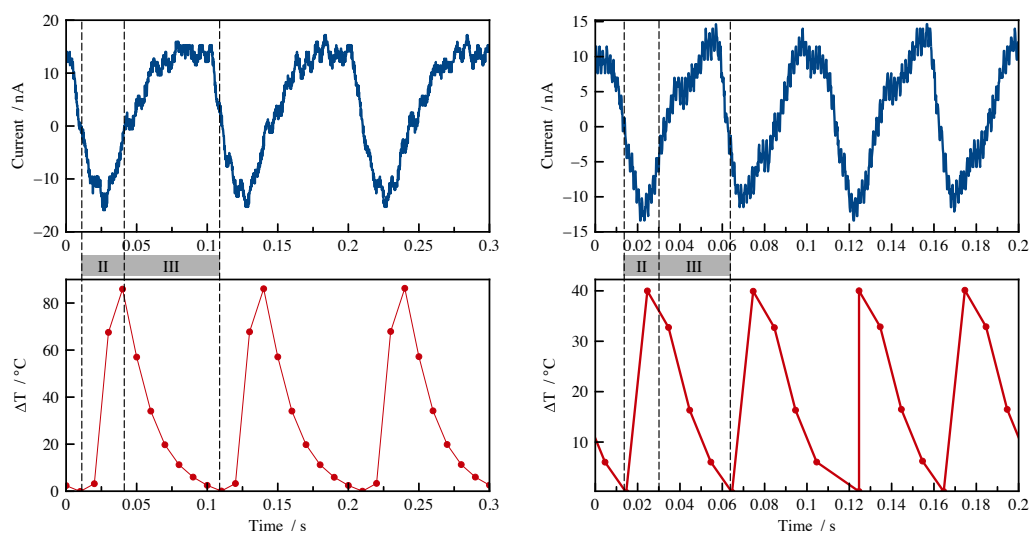


Figure 6.6: Current signal and corresponding surface temperature change at 10 Hz heating rate (left) and 20 Hz heating rate (right).

At these heating and cooling rates, the material does not undergo the complete cycle from phase I to IV as described above, but only from phase II to III, as the sample rests in austenitic state and the temperature changes only between  $M_S < T < T_C$ .

The current output of all laser heating experiments is very low, not exceeding peaks of

60 nA at maximum. This leads to corresponding average power densities below  $15 \text{ nW}\cdot\text{cm}^{-3}$  even for fast heating cycles. Still, the power densities are two orders of magnitude higher than for the reported experimental results of [82], which did not exceed  $0.1 \text{ nW}\cdot\text{cm}^{-3}$  for the presented demonstrator device.

### 6.2.4 Conclusions

The principle of direct energy harvesting by laser heating and cooling in air of MSMA material is shown. However, the experimental results show a very small electrical output. The output could possibly be increased slightly by optimizing the magnetic setup, but will remain at low power densities.

Additionally, the use of a laser based dynamic heat source is not feasible for energy harvesting applications. A stationary heat source, heating the MSMA material by direct contact is a more realistic assumption for the investigation of MSMA-based energy harvesting.

## 6.3. MSMA-based Direct Energy Harvesting by External Actuation

### 6.3.1 Operation Principle

The presented concept of MSMA-based direct energy harvesting can also be applied to an externally actuated system, which moves the MSMA-based energy harvesting device between a heat source and sink. Figure 6.7 depicts such a principle where a polyimide cantilever, acting as a reset spring, is carrying the magnet, pick-up coil, and the MSMA material. The tip is deflected from the heat source by an external force. While in contact to the heat source, the temperature induced phase transformation of the MSMA material, and the corresponding magnetization change induces a current in the pick-up coil, as shown for the laser heated MSMA-based energy harvesting device in Chapter 6.2.1.

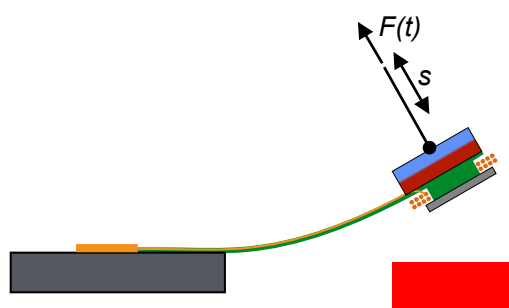


Figure 6.7: Schematic of an externally actuated MSMA-based energy harvesting device, working by direct conversion of heat change to electricity.

### 6.3.2 Fabrication

The setup of the externally actuated MSMA-based energy harvesting device is very similar to the device for the direct energy harvesting by laser heating, described before.

The device consisting of magnet, pick-up coil, and MSMA film stack is fixed on an elastic reset spring, which could be a polyimide cantilever or a silicone foil bridge. The reset spring pushes the device against a copper heat source. It is deflected by an external linear actuator, pulling the reset actuator away from the heat source. Figure 6.8 shows the setup. At the bottom, the copper heat source is visible. Above, the MSMA-based direct energy harvesting device with a MSMA film stack, pick-up coil, and magnet can be seen. The device is fixed on a silicone foil double bridge of 50  $\mu\text{m}$  thickness, which is deflected by a cord, pulling it away from the heat source. The external linear actuator is controlled by LabView, moving the energy harvesting device to a maximum distance from the heat source of about 3 mm.

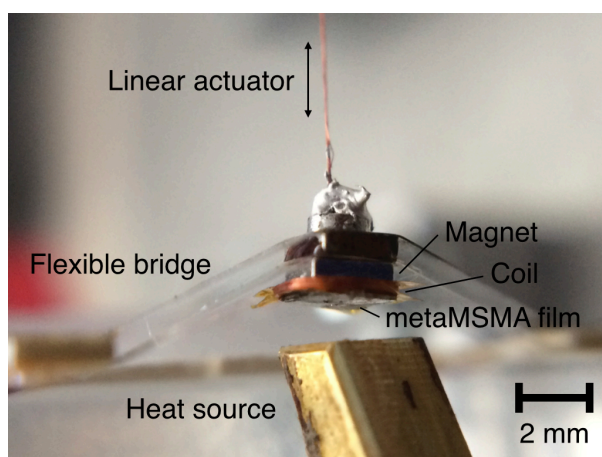


Figure 6.8: Photo of a MSMA-based energy harvesting device using direct conversion of heat to electricity by external actuation.

### 6.3.3 Results

Figure 6.9 shows a typical current signal, measured for the externally actuated setup. The figure also depicts the displacement of the MSMA-based energy harvesting device.

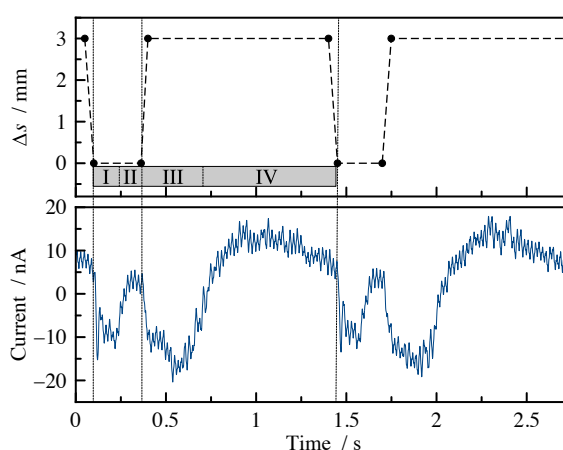


Figure 6.9: Induced current and the preset displacement for the externally actuated MSMA-based direct energy harvesting. [90] © 2014 WILEY-VCH

The overall cycle takes 1.5 s, including heating by direct contact to the copper heat

source (phases I and II), as well as cooling by convection (phases III and IV). The heating time is 0.3 s and the heat source temperature is 160 °C.

The induced current signal is similar to the full cycle shown in Figure 6.5. This is due to the full martensitic transformation and ferro- to paramagnetic transition in the phases I to IV. The two small peaks in phase I and II indicate the first and second order transition from non-magnetic martensite to ferromagnetic austenite and to paramagnetic austenite at  $T_C$ , respectively. The larger peaks indicate the ferromagnetic transition and the reverse transformation to non-magnetic martensite. The maximum induced current peaks reach about 20 nA.

By tailoring the heating and cooling times, the power output can be strongly increased. In Figure 6.10, the sample temperature range is reduced to  $M_s < T < T_C$  by shortening the heating and cooling time to approximately 0.1 and 0.3 s, respectively. Thereby, only phase II and III are passed, but with an increasing effect in phase II, as the decreasing magnetization does not start from the relatively low magnetization at  $A_r$ , but the higher magnetization close to  $M_s$ . This leads to current peaks of almost 100 nA at a relatively high operation frequency of approximately 2.5 Hz. The corresponding maximum power density is about  $1.25 \text{ nW}\cdot\text{cm}^{-3}$ .

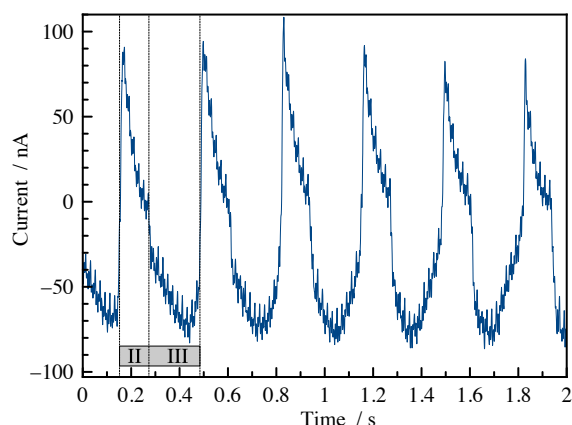


Figure 6.10: Reduced heating and cooling times for the MSMA-based direct energy harvesting device, leading to higher current peaks by only passing phase II and III. [90] © 2014 WILEY-VCH

### 6.3.4 Conclusions

The results of the externally actuated MSMA-based direct energy harvesting device show that the use of stationary heat sources is possible. However, the electrical power output remains low. Because of the slower heating and cooling times, the power density is even lower than for the MSMA-based energy harvesting device heated by laser pulses. For thin films it is challenging to design a magnetic setup with small losses. As already stated in [82], a coil around thin rods would be more beneficial for electromagnetic conversion. However, such rods would be very disadvantageous for fast heating and cooling. Therefore, indirect electromagnetic conversion should be considered, similar to the FSMA-based energy harvesting device shown in Chapter 5.3.

Another limitation of the presented energy harvesting device is the use of external actuation. Self-actuated harvesting principles can be much more efficient, as no external energy for actuation is needed. It is therefore beneficial to make use of the self-actuation capability of MSMA films.

## 6.4. Self-Actuated MSMA-based Energy Harvesting

### 6.4.1 Operation Principle

As the most common available heat sources for energy harvesting are stable in time and space, providing a stationary temperature gradient, it is beneficial to develop a self-actuated energy harvesting system in order to subject the MSMA material to a changing temperature. Such a principle is shown in Figure 6.11. Similar to the externally actuated device, the MSMA material is attached as a stack of MSMA films to a pick-up coil on the tip of a polyimide cantilever. The cantilever, working as a reset spring, brings the film into contact with a heat source. On heating up, the magnetization change induces the magnetic attraction force, leading to a deflection of the cantilever towards a magnet, placed above. On cooling below the transformation temperature  $T_0$ , the cantilever is reset back to the heat source where the MSMA film heats up again.

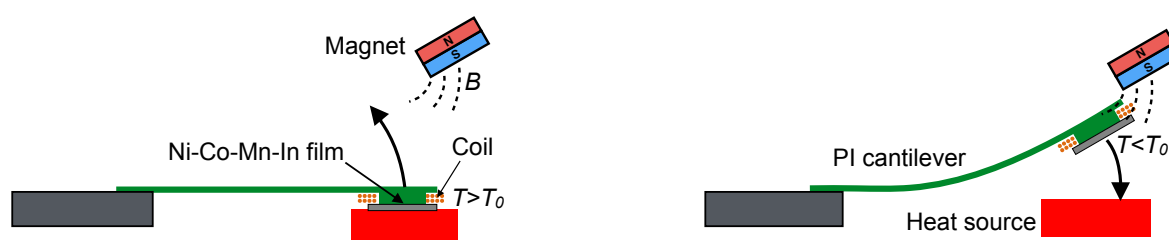


Figure 6.11: Schematic of the self-actuated MSMA-based energy harvesting device.

This principle not only uses the direct conversion of heat to electricity by magnetization change of the material. The change of magnetic attraction force, switched on and off by the first order phase transformation, induces a mechanical motion, which then can be used to generate electricity: the microcoil, attached to the cantilever tip, moves in the magnetic field gradient generated by the external magnet, inducing an electrical current according to Faraday's law.

### 6.4.2 Fabrication

The fabrication is similar to the MSMA-based direct energy harvesting device described in Chapter 6.2.2. The device consists of a stack of MSMA films, microcoil, and magnet, as can be seen in Figure 6.12. Instead of applying the magnet directly to the pick-up coil, it is placed externally above the magnet. MSMA film stack and microcoil are fixed to the tip of a polyimide cantilever by adhesive bonding. The cantilever is cut out of a 25  $\mu\text{m}$  thick polyimide foil. The copper wires are wound around the cantilever and fixed on the substrate.

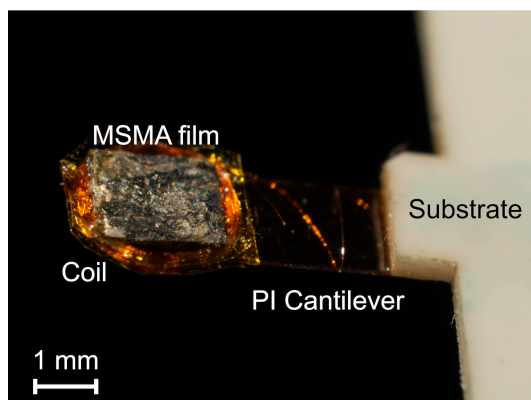


Figure 6.12: Picture of self-actuated MSMA-based energy harvesting device. [90] © 2014 WILEY-VCH

### 6.4.3 Mechanical Characterization

Because of the limitations of the setup, consisting of a heat source on one side and the magnet on the other side, an image tracking system is used to investigate the time-dependent cantilever tip displacement. The result of one actuation period is shown in Figure 6.13. The tip is first touching the heat source at  $\Delta s = 0$ , heating up above the transformation temperature  $A_s$ . In ferromagnetic state the tip is attracted by the magnetic attraction force of the permanent magnet. The magnet is located approximately 0.4 mm above the heat source. Therefore, the cantilever is deflected away from the heat source. At the edge of the magnet, the tip oscillates with a frequency of above 160 Hz for about 0.3 s. The maximum amplitude of above 200  $\mu\text{m}$  is not displayed fully because of the limited time resolution of the image tracking system. After the decay of the oscillation due to air damping, the tip moves slightly closer to the edge of the magnet until it is reset to the heat source after 0.7 s of cooling.

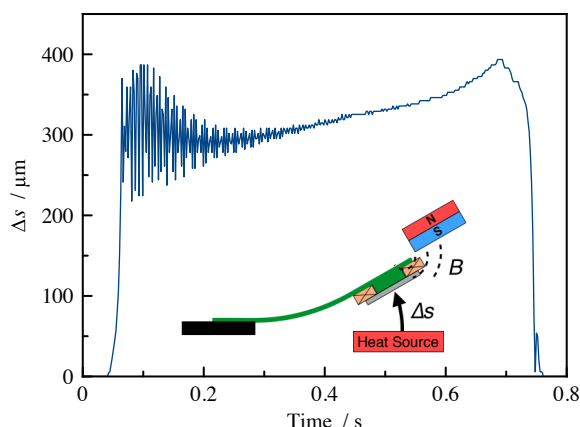


Figure 6.13: Displacement of the tip of the self-actuated MSMA-based energy harvesting device with respect to its original position at the heat source ( $\Delta s=0$ ). [90] © 2014 WILEY-VCH

The oscillation at the edge of the magnet is due to the kinetic energy, stored in the MSMA cantilever tip on approaching the magnet. Reaching its edge, the cantilever oscillates around its equilibrium position and cools down. The cooling down to  $M_s$  first in-

creates the magnetization of the MSMA material at the tip, which causes the subsequent deflection of the cantilever closer towards the magnet. As soon as the martensitic transformation starts, the magnetization of the MSMA film decreases strongly. Consequently, the reset force of the cantilever becomes predominant, pulling the tip back to its original position at the magnet. The small peak at 0.75 s is due to an elastic impact of the tip on the heat source.

#### 6.4.4 Thermal Characterization

In order to investigate the thermal behavior of the MSMA-based energy harvesting device, infrared thermography measurements are performed. The temperature of the oscillating cantilever cannot be measured correctly, due to fuzziness of infrared thermography images. Therefore, the magnet is positioned in a way that the cantilever touches it on cooling and rests in a stationary position. Thus, the average tip temperature can be measured at the two extreme states for heating and cooling at the heat source and the magnet. Figure 6.14 shows infrared pictures of the cantilever on heating and cooling, respectively. A SMD resistor works as a heat source, heated to approximately 135 °C. The magnet is at room temperature and also acts as heat sink.

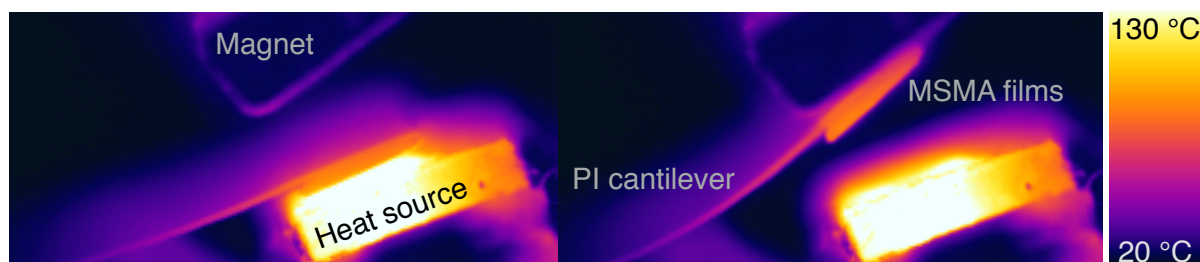


Figure 6.14: Infrared thermography of the self-actuated MSMA-based energy harvesting system with a SMD resistor as heat source. [92] © 2015 The Authors CC BY NC ND

The measured time resolved temperature development of the MSMA tip is shown in Figure 6.15.

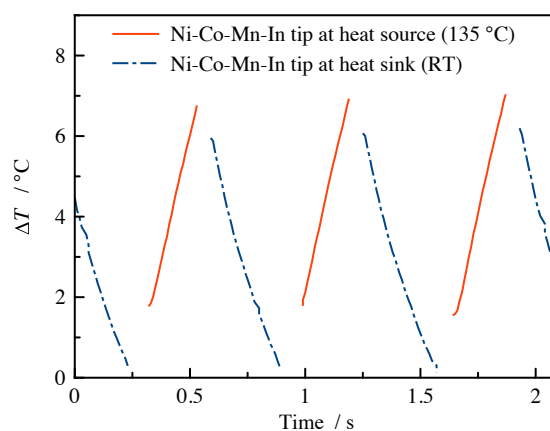


Figure 6.15: Time resolved average temperature of the MSMA tip at the heat source and the magnet, indicating temperature changes in the range of  $\Delta T = 7$  K. [92] © 2015 The Authors CC BY NC ND

The temperature is only plotted for the time when the tip is either resting on the heat source or the heat sink. The overall temperature change can be determined to be about 7 K, indicating that not the whole transformation takes place, as  $A_f - M_f = 14$  K. Still, it matches well the hysteresis of  $\text{Ni}_{50.4}\text{Co}_{3.7}\text{Mn}_{32.8}\text{In}_{13.1}$ , which is measured by DSC and resistance measurements, to be only about 6 K. The heating and cooling rates are calculated to be 24.57 and  $-19.37 \text{ K}\cdot\text{s}^{-1}$ , respectively.

#### 6.4.5 Electrical Output

The current signal of the self-actuated MSMA-based energy harvesting device strongly differs from the MSMA-based direct energy harvesting. Besides the direct induction of a current due to magnetization change, an additional current due to the movement of the coil in the magnetic field gradient of the external permanent magnet is induced. This indirect use of the magnetization change by using the changing magnetic attraction force leads to a much higher current signal, as shown in Figure 6.16. Peaks of approximately  $10 \mu\text{A}$  and a declining oscillation, similar to the first FSMA-based energy harvesting devices, can be seen.

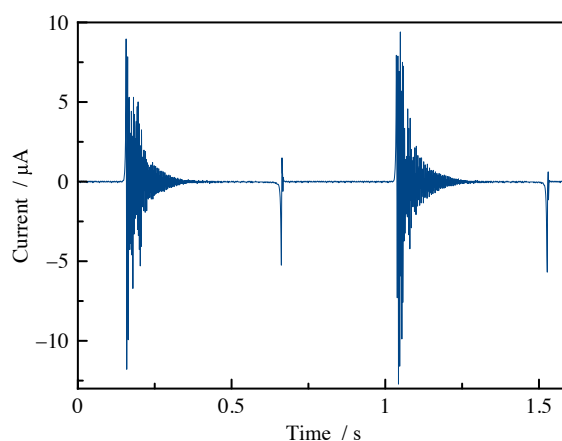


Figure 6.16: Typical current signal of the self-actuated MSMA-based energy harvesting device with frequency up-conversion on oscillating at the magnet edge. [90] © 2014 WILEY-VCH

The oscillation frequency, determined from the current signal in Figure 6.16, is above 200 Hz, fast declining, corresponding to the mechanical behavior shown in Figure 6.13. The impact on the heat source is accompanied by a current peak, which corresponds to the elastic impact in the deflection signal. The average power output of the harvesting device is 0.12 nW, resulting in a power density of  $1.6 \mu\text{W}\cdot\text{cm}^{-3}$ . The peak power and the resulting peak power density are 10 nW and  $0.13 \text{ mW}\cdot\text{cm}^{-3}$ , respectively. This is a significant increase compared to the MSMA-based direct energy harvesting devices.

By using the magnet as a heat sink, restricting a free cantilever oscillation around its edge, the elastic impact of the cantilever tip on the magnet gives rise to very high current peaks of approximately  $60 \mu\text{A}$ . Figure 6.17 shows on the left side two full cycles

with first the elastic impact on the magnet and second the impact on the heat source. The right side shows only the elastic impact of the cantilever tip on the magnet, revealing that the frequency of the oscillation due to the impact is 1 kHz. Taking into account a large magnetic field gradient because of the proximity to the magnet, this leads to high current peaks. However, the oscillation is damped very quickly and therefore the duty cycle is extremely low. The maximum peak power densities achieved by this actuation are  $5 \text{ mW}\cdot\text{cm}^{-3}$ .

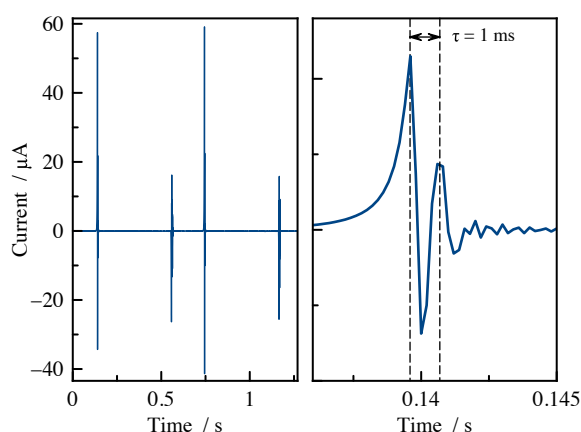


Figure 6.17: Current signal of the self-actuated MSMA-based energy harvesting device, using the elastic impact on the external permanent magnet.

#### 6.4.6 Conclusions

The experimental results of the self-actuated MSMA-based energy harvesting demonstrator show the feasibility of the indirect conversion of magnetization change to electricity, making use of an external magnetic field gradient. The average power density of  $1.6 \text{ }\mu\text{W}\cdot\text{cm}^{-3}$  is almost three orders of magnitude higher than for the MSMA-based direct energy harvesting conversion principles. The peak power density of the energy harvesting device using the elastic impact on the magnet, which is  $5 \text{ mW}\cdot\text{cm}^{-3}$ , even compares well to the FSMA-based energy harvesting devices using an integrated microcoil (Chapter 5.3).

However, the thermal operation frequencies of the self-actuated MSMA-based energy harvesting devices are relatively low. This can be compensated by frequency up-conversion only in part. A narrower hysteresis of the first order phase transformation could decrease the thermal cycle time. This would enable higher duty cycles, eventually comparable to the FSMA-based energy harvesting devices using a magnetic heat source (Chapter 5.4). By further optimizing the magnetic design and tuning of mechanical and thermal masses, a substantial improvement in power output and power density is expected for future devices.

In particular, as the change of magnetization  $\Delta M/\Delta T$  of the first order phase transformation in the investigated MSMA material is larger compared to the ferro- to paramagnetic transition in FSMA material, a similar or even higher power output should be

possible.

## 6.5. Pyroelectric Energy Harvesting by MSMA-based Actuation

Besides the electromagnetic induction based principles also pyroelectricity can be used in combination with self-actuated MSMA-based energy harvesting devices for energy conversion.

### 6.5.1 Operation Principle

Similar to MSMA-based direct energy harvesting, pyroelectric energy harvesting needs changing temperatures in order to generate a voltage, as described in Chapter 2.2. A combination of the two techniques is therefore proposed in the schematic shown in Figure 6.18. Like the self-actuated MSMA-based energy harvesting principle, the system consists of a polyimide cantilever with a MSMA plate attached to the front end. Additionally, a thin plate of pyroelectric material is added in between or below the MSMA plate. A magnet above and a heat source below the cantilever are put in place. As described in Chapter 6.4.1, this leads to a periodic movement of the cantilever tip. The pyroelectric material, which is electrically connected to the substrate, generates a voltage every time it heats up and cools down.

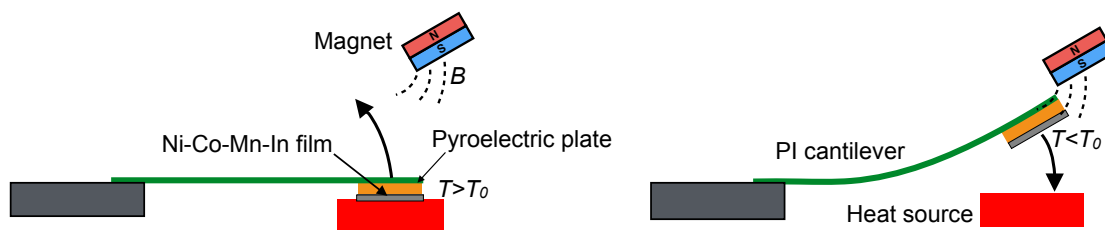


Figure 6.18: Schematic of pyroelectric energy harvesting by MSMA self-actuation.

### 6.5.2 Fabrication

Figure 6.19 shows the pyroelectric energy harvesting device, consisting of polyimide cantilever for resetting, pyroelectric plate, and MSMA plate.

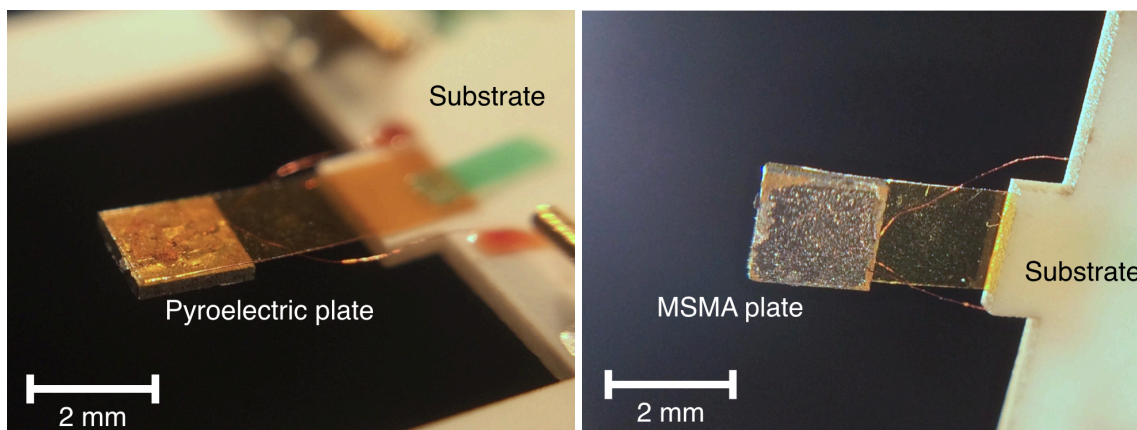


Figure 6.19: Picture of the pyroelectric MSMA-based energy harvesting device.

The cantilever of  $2 \times 4 \text{ mm}^2$  size is cut out from a  $25 \text{ }\mu\text{m}$  thick polyimide foil. A  $200 \text{ }\mu\text{m}$  thick pyroelectric plate (PZT) is laser cut to  $2 \times 2 \text{ mm}^2$  and attached to the cantilever tip by adhesive bonding. On the pyroelectric material a  $2 \times 2 \times 0.05 \text{ mm}^3$  MSMA plate is fixed.  $15 \text{ }\mu\text{m}$  thick copper wires are attached to the electrodes on the top and bottom face of the pyroelectric plate, using silver adhesive. The copper wires are then connected to the substrate. In order to electrically isolate heat source and cantilever tip with respect to each other, the heat source is covered by a thin film of epoxy adhesive.

### 6.5.3 Results

The mechanical actuation is similar to the self-actuated MSMA-based energy harvesting device, as the same material is used to trigger the self-actuation. As a  $200 \text{ }\mu\text{m}$  thick pyroelectric ceramic is added additionally to the MSMA material, the heating and cooling times increase strongly. Also, the overall temperature change increases, as is shown in Figure 6.20.  $\Delta T$  increases to about 25 K and the heating and cooling rates are  $41.8$  and  $-17.44 \text{ K}\cdot\text{s}^{-1}$ , respectively.

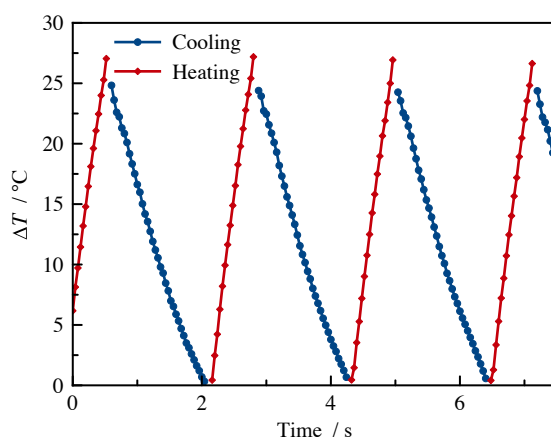


Figure 6.20: Time resolved measurement of the temperature change at the pyroelectric cantilever tip.

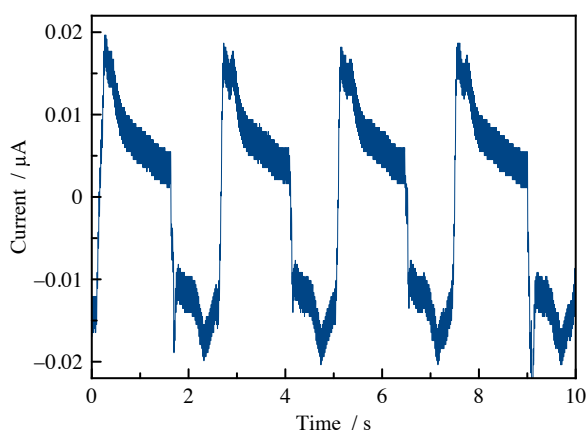


Figure 6.21: Current signal of the pyroelectric energy harvesting device based on MSMA self-actuation.

The current signal is measured using a  $300 \text{ k}\Omega$  resistor as load resistance. The result is depicted in Figure 6.21. Current peaks of approximately  $20 \text{ nA}$  are induced, corre-

sponding to voltages of 6 mV. The electrical peak power output and the peak power density are 0.12 nW and  $0.15 \mu\text{W}\cdot\text{cm}^{-3}$ , respectively.

#### 6.5.4 Conclusions

The results of the pyroelectric energy harvesting demonstrator based on MSMA self-actuation show the feasibility of using pyroelectric material in combination with the intrinsic self-actuation capabilities of MSMA material. The resulting power density of  $0.15 \mu\text{W}\cdot\text{cm}^{-3}$  is much higher than for the MSMA-based direct energy harvesting devices, and only one order of magnitude below the self-actuated MSMA-based energy harvesting device. This is due to the larger amount of active material, as the average electrical power output of 0.12 nW is the same.

As for the MSMA-based energy harvesting using self-actuation, there is a large potential in optimization of the pyroelectric energy harvesting principle. The duty cycle can be increased by better MSMA material showing a narrower hysteresis. Another important point is the increase of the heating and cooling rates. In the present setup, the epoxy coated heat source is limiting the heating rate. If a direct contact to the heat source can be established, the heating rate should increase strongly. For cooling, a more direct thermal contact to the heat sink could increase the cooling rate substantially. The polyimide cantilever hinders a good thermal contact, therefore a metallic reset-cantilever would be beneficial. The heating and cooling rates influence the induced voltage directly as the voltage generation depends proportionately on temperature change. As the electrical power increases exponentially with the induced voltage, better heating and cooling performances would strongly affect the electrical output.

Additionally, pyroelectric material with higher pyroelectric coefficients can be used, improving the overall efficiency and power, as stated for example in [56].

## 7. Design Parameters and Theoretical Discussion

The performance of the demonstrators, described in the previous chapters, depend on various design parameters. Thus there are a variety of options in tuning and adjusting them to optimize the overall performance. The design parameters can be organized into four categories:

- heat transfer,
- actuation forces,
- kinetic energy,
- energy conversion (thermo- and magnetomechanic, electromagnetic).

They will be discussed in detail in this chapter, including the design parameters for each category.

### 7.1. Heat Transfer

Heat transfer takes place on heating and cooling of the magnetic SMA materials. Heating happens at the heat source, where the cantilever and cantilever tip are heated up by direct contact or by laser irradiation. Cooling is achieved by either natural or forced convection through an oscillatory motion in air.

In order to describe the heating process, an equation for the time-dependent temperature is formulated. For simplification, in the first step the phase transformation is not considered, as is the case for FSMA-based energy harvesting. The tip temperature  $T$  depends on the heat  $Q_{heat}$ , which is introduced into the magnetic SMA material. This can be expressed as

$$Q_{heat} = \Delta T \cdot m \cdot c_p = (T - T_{start}) \cdot m \cdot c_p. \quad (11)$$

$T_{start}$  is the tip temperature at the beginning of heating,  $m$  is the mass of the heated material and  $c_p$  is the specific heat capacity. The heat flow from heat source to cantilever is given by

$$\dot{Q}_{heat} = \alpha \cdot A \cdot (T_{source} - T), \quad (12)$$

with the heat transfer coefficient  $\alpha$ , the contact area  $A$ , and the heat source temperature  $T_{source}$ . As the heat flow and the temperature are dependent upon each other, the two equations can be combined to a differential equation by solving Equation (11) for  $T$  and inserting in Equation (12):

$$\dot{Q}_{heat} + \frac{\alpha \cdot A}{m \cdot c_p} \cdot Q_{heat} = \alpha \cdot A \cdot (T_{source} - T_{start}). \quad (13)$$

Integrating this equation by taking into account that  $Q_{heat}(t=0) = 0$ , gives

$$Q_{heat} = m \cdot c_p \cdot (T_{source} - T_{start}) \cdot \left(1 - e^{-\frac{\alpha \cdot A}{m \cdot c_p} t}\right). \quad (14)$$

Inserting this to Equation (11) and solving for  $T$  results in

$$T = T_{start} + (T_{source} - T_{start}) \cdot \left(1 - e^{-\frac{\alpha_{heat} \cdot A}{m \cdot c_p} t}\right). \quad (15)$$

As can be seen in Equation (15), the result is an exponential temperature development, approaching the heat source temperature.

The heat transfer stops as soon as the cantilever leaves the heat source. This happens, when  $T$  increases and the reset or SME force (for FSMA-based principles) exceeds the magnetic force at a critical temperature  $T_{crit}$ . The heat transfer times can be calculated if  $T_{crit}$  as well as the amount of material, and heat transfer parameters are known.

For cooling, a similar equation as for heating can be derived:

$$T = T_{start} - (T_{start} - T_{air}) \cdot \left(1 - e^{-\frac{\alpha_{cool} \cdot A}{m \cdot c_p} t}\right). \quad (16)$$

The difference in heating and cooling rates is mainly due to a different heat transfer coefficient  $\alpha$ . For cooling through convection ( $\alpha_{cool}$ ) it is several orders of magnitude smaller than for direct contact to the heat source ( $\alpha_{heat}$ ). In general, the heat transfer times, or the speed at which the temperature changes, is highly dependent on the surface to volume ratio  $A/v$ . Therefore, thin films are favorable for fast heating and cooling cycles.

If the latent heat  $Q_L$  of the first order phase transformation in the MSMA-based energy harvesting principles is taken into account as well, the equation for heating changes to

$$T = T_{source} - \left( (T_{source} - T_{start}) + \frac{Q_L}{m \cdot c_p} \right) \cdot e^{-\frac{\alpha \cdot A}{m \cdot c_p} t}. \quad (17)$$

The design parameters which can be derived from this consideration are:

- mass  $m$ ,
- contact surface  $A$ ,
- heat transfer coefficient  $\alpha$ :
  - $\alpha_{heat}$  for direct contact,
  - $\alpha_{cool}$  for cooling by convection.

Short heating and cooling times can be achieved by a small mass, a large heat transfer coefficient, and a large contact surface. Contact surface and mass are defined by the energy harvesting demonstrator's geometry. The thermal interface, where the cantilever

is in direct contact to the heat source, can be optimized in order to decrease the heat transfer coefficient. This is achieved for instance by materials with smooth contact surfaces and very low roughness. It ensures the best heat transfer and is, depending on the material, more favorable than introducing additional heat transfer layers which may increase the thermal resistance [93]. Typical values for heat transfer coefficients for direct contact and forced convection are 400 to 2000  $\text{W}\cdot(\text{m}^2 \text{K})^{-1}$  [72, 93, 94] and 20 to 100  $\text{W}\cdot(\text{m}^2 \text{K})^{-1}$  [95-97], respectively.

Table 7.1 shows typical heat transfer times for the investigated energy harvesting demonstrator devices as well as the volume of active magnetic material.

Table 7.1: Typical heat transfer times for the investigated energy harvesting devices and volume of active magnetic SMA material.

Demonstrator	Heating time	Cooling time	Volume of active material
FSMA external coil	100 ms	400 ms	2 x 1.5 x 0.2 mm <sup>3</sup>
FSMA microcoil	1-2 ms	9-10 ms	2 x 4 x 0.005 mm <sup>3</sup>
FSMA magnetic heat source	1-2 ms	9-10 ms	2 x 2 x 0.005 mm <sup>3</sup>
MSMA direct laser heating	5-15 ms	45-85 ms	
MSMA external actuation	300 ms	1200 ms	2 x 2 x 0.05 mm <sup>3</sup>
MSMA self-actuation	300-400 ms	500 ms	

## 7.2. Actuation Forces

The actuation method of self-actuated energy harvesting principles, described in previous chapters, is based on a freely movable cantilever with a mass attached to its tip. During the actuation cycle, magnetic and reset forces play an important role for the overall system performance. These actuation forces and the corresponding design parameters are described in detail for FSMA-based energy harvesting in this section.

The first step is the magnetic attraction of the cantilever towards the magnet. The cantilever has a linear reset force, which depends on its geometry (thickness  $t$ , length  $l$ , and width  $w$ ) and the Young's modulus  $E_Y$  of the material. It can be expressed in dependence of the distance  $d$  from the magnet and the initial position  $d_0$  as followed:

$$F_{reset} = (d - d_0) \cdot \frac{E_Y \cdot w \cdot t^3}{4 \cdot l^3}. \quad (18)$$

The magnetic force for a magnetizable body can be expressed by a volume integral of the magnetic material and the gradient of magnetic flux density  $B$  and magnetization  $M$  as shown in Equation (19) [98].

$$\mathbf{F}_{mag} = \mu_0 \int (\mathbf{M} \cdot \nabla) \mathbf{H} dV. \quad (19)$$

This can be simplified for the case that the magnetic film sample, of volume  $V_{mag}$ , is perpendicular to the symmetry axis of the permanent magnet:

$$F_{mag} = (\mathbf{F})_x = V_{mag} \cdot \left( M_x \cdot \frac{\partial B}{\partial x} + M_x \cdot \frac{\partial B}{\partial y} + M_x \cdot \frac{\partial B}{\partial z} \right) \approx V_{mag} \cdot M \cdot \frac{\partial B(x)}{\partial x}. \quad (20)$$

As only the x component is needed, the variable  $d$  is introduced for the distance from the magnet. For a simplified approach, the magnetic flux density is approximated by an exponential fit using the fit parameters  $a$  and  $b$  [72]:

$$B(d) \approx a \cdot e^{-b \cdot d}. \quad (21)$$

The magnetic attraction force  $F_{mag}$  can therefore be expressed as

$$F_{mag} \approx V_{mag} \cdot M \cdot a \cdot b \cdot e^{-b \cdot d}. \quad (22)$$

For complete deflection of the cantilever by the magnetic attraction force, the sum of  $F_{mag}$  and  $F_{reset}$  has to be positive for the entire deflection movement. A schematic of this relation is shown in Figure 7.1. If the initial position of the cantilever tip  $d_0$  is fixed, the maximum stiffness can be calculated, as the absolute values of force and slope of  $F_{mag}$  and  $F_{reset}$  are equal at distance  $d_1$ .

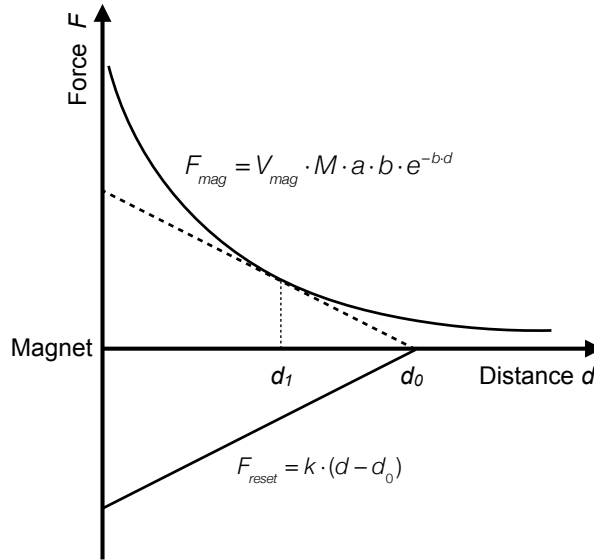


Figure 7.1: Schematic of magnetic attraction and reset force in dependence of the distance from the magnet.

By equating  $F_{mag}$  and  $F_{reset}$  and their first derivatives at  $d_1$ , the cantilever stiffness  $k$  is obtained, dependent on the initial position  $d_0$ :

$$k = V_{mag} \cdot M \cdot a \cdot b^2 \cdot e^{1-b \cdot d_0}. \quad (23)$$

This equation shows the dependency of the cantilever design on the amount of magnetic material  $V_{mag}$ , the material magnetization  $M$ , and the initial position  $d_0$ . A larger magnetization and volume allow for a larger stiffness. If the initial distance  $d_0$  is in-

creased, the maximum stiffness decreases. This correlation also allows for tuning the demonstrator design for a given stiffness by adjusting the initial position  $d_0$ .

From the considerations on attraction and reset forces, several design parameters can be identified:

- geometric parameters of cantilever and magnetic material,
- initial position of cantilever tip  $d_0$ ,
- Young's modulus  $E_Y$  of the cantilever,
- external magnetic field  $H$
- magnetic field gradient  $dB/dx$ ,
- magnetization  $M$  of the magnetic material.

While in some operation principles the Young's modulus cannot be changed individually, in other demonstrator layouts the cantilever material can be chosen independently, allowing for optimized adjustments. The geometric parameters have to be carefully tuned to match the constraints given by the magnetization characteristics of the used material, as they do not only influence the mechanical properties, but also the magnetic attraction force. The external magnetic field as a design parameter should be chosen to be as high as possible as this is favorable for large actuation forces. Ensuring a large magnetic field gradient, a relatively large reset cantilever stiffness can be chosen, which will enable a high resonant frequency, beneficial for high frequency energy harvesting as will be shown in the next section.

Table 7.2 shows several design parameters, important for actuation forces, which are implemented in the energy harvesting devices presented in this work.

Table 7.2: Typical design parameters for the investigated energy harvesting devices, including maximum magnetization, cantilever dimensions, Young's Modulus and initial magnet position.

Demonstrator	Max. material magnetization, $M$	Cantilever dimension	Cantilever material, $E_Y$	Initial position, $d_0$
FSMA external coil	$50 \text{ emu}\cdot\text{g}^{-1}$	$2 \times 4 \times 0.01 \text{ mm}^3$	Ni-Mn-Ga, 120 GPa [99]	
FSMA microcoil	$26 \text{ emu}\cdot\text{g}^{-1}$	$2 \times 4 \times 0.005 \text{ mm}^3$	Ni-Co-Mn-Ga, 38.3 GPa	1-1.5 mm
FSMA magnetic heat source	$50 \text{ emu}\cdot\text{g}^{-1}$	$3 \times 5 \times 0.01 \text{ mm}^3$	Brass, 110 GPa [100]	
MSMA self-actuation	$26 \text{ emu}\cdot\text{g}^{-1}$	$2 \times 4 \times 0.025 \text{ mm}^3$	Polyimide, 2.5 GPa [101]	0.5 mm

### 7.3. Kinetic Energy and Resonance

Heat is transduced to kinetic energy in most of the presented harvesting principles. For these principles a simple equation of motion can be formulated, comprising the mass

$m$ , the deflection  $x$  from the equilibrium position, damping  $D$ , the cantilever stiffness  $k$ , and  $F(x, T)$ , describing the magnetic and reset forces:

$$m \cdot \ddot{x} + D \cdot \dot{x} + k \cdot x = F(x, T). \quad (24)$$

Damping can be distinguished in structural, air, and electromagnetic damping. Electromagnetic damping  $D_{em}$  can be described using the number of coil turns  $N$ , the area of the coil  $A_{coil}$ , and the load resistance  $R_{load}$  as

$$D_{em} = \frac{\left( N \cdot A_{coil} \cdot \frac{\delta B}{\delta x} \right)^2}{R_{load}}. \quad (25)$$

After an initial startup time, when the system is in a stable oscillation, the potential energy stored in the elastic reset cantilever at maximum deflection can be expressed as

$$E_{spring} = \frac{1}{2} \cdot k_{spring} \cdot d^2 = \frac{1}{2} \cdot \frac{E_Y \cdot w \cdot t^3}{4 \cdot l^3} \cdot d^2. \quad (26)$$

$E_Y$  is the Young's modulus,  $w$ ,  $t$ , and  $l$  are the width, thickness, and length of the cantilever, respectively. When moving away from the heat source, the energy stored in the spring is converted to kinetic energy. At zero deflection no more energy is stored in the spring and the whole energy is in the form of kinetic energy:

$$E_{kin} = \frac{1}{2} \cdot m \cdot v^2. \quad (27)$$

If the cantilever can move freely or when the heat transfer times match the mechanical oscillations, the cantilever tip moves at resonance frequency  $f_{res}$ . If damping is neglected, the frequency can be calculated by

$$f_{res} = \frac{1}{2 \cdot \pi} \cdot \sqrt{\frac{k_{spring}}{m}} = \frac{1}{2 \cdot \pi} \cdot \sqrt{\frac{E_Y \cdot w \cdot t^3}{m \cdot 4 \cdot l^3}}. \quad (28)$$

If a magnetic SMA based demonstrator device works as oscillator at resonance, described by Equation (24), losses are only caused by damping. In order to keep the system running, these losses need to be compensated by an external force. In resonance, this force may be relatively small, which is favorable for thermomagnetic self-actuation at small temperature differences.

The design parameters, which can be derived from these considerations are:

- geometric parameters of the cantilever,
- Young's modulus  $E_Y$ ,
- moving mass  $m$ ,
- damping constants  $D_i$  for structural, air, and electrical damping.

The geometric design parameters as well as the Young's modulus should be chosen to match closely the heat transfer times of the energy harvesting system, allowing for a resonant operation. As has been demonstrated in this thesis, the resulting resonant oscillation enables very efficient kinetic to electric energy conversion. If the structural

damping is small, the input energy matches closely the electrical damping, ensuring high conversion efficiencies. Therefore, cantilever material with a high quality factor should be chosen to minimize losses.

Table 7.3 shows typical values for kinetic behavior and coil design parameters for the energy harvesting devices investigated.

Table 7.3: Kinetic measurement values and coil parameters of investigated energy harvesting devices.

Demonstrator	Oscillation-frequency	Max. stroke	Type of coil, number of turns	Coil dimension, wire thickness
FSMA external coil	82 Hz	0.8 mm	external coil, 250-1000	5 x 5 mm <sup>2</sup> , 40 μm
FSMA microcoil	80-125 Hz	2.3 mm	microcoil, 100-200	2 x 1.5 mm <sup>2</sup> , 15 μm
FSMA magnetic heat source	85 Hz	2.1 mm	microcoil, 200	3 x 2 mm <sup>2</sup> , 15 μm
MSMA self-actuation	200 Hz	0.4 mm	microcoil, 50	2 x 2 mm <sup>2</sup> , 15 μm

## 7.4. Energy Conversion

Energy conversion takes place in several steps. First, the heat introduced into the system changes the magnetization of the magnetic SMA material. After thermomagnetic conversion, the magnetic energy is converted to mechanical energy (potential and kinetic). Using this mechanical energy, electrical energy is gained by electromagnetic conversion according to Faraday's law.

The thermomagnetic energy conversion is strongly dependent on the change of magnetization  $\Delta M/\Delta T$ . A simplified general definition of thermomagnetic efficiency is found in [73] and [102]:

$$\eta \approx \frac{\oint_{\text{Cycle}} H dM(T, H)}{\rho \int_{T_{\text{cold}}}^{T_{\text{hot}}} c_p(T) dT} \approx \frac{\frac{1}{2} \cdot \mu_0 \cdot H_{\text{max}} \cdot \Delta M}{\rho \cdot c_p \cdot \Delta T}. \quad (29)$$

In literature, the maximum thermomagnetic conversion efficiency is found by simulations to be about 0.2% [72, 73, 84], relating to large relative efficiencies  $\eta_{\text{rel}}$ , with respect to the Carnot efficiency, of up to 20% [73].

After thermomagnetic conversion, magneto-mechanic conversion takes place by inducing periodic magnetic attraction forces. As described in the section before, the most beneficial operation mode is a resonant oscillation, as the thermomagnetic input energy needed is minimized in this case. Only damping losses due to structural, air, im-

pact, and electromagnetic damping have to be compensated in resonant state. The quality of resonant oscillation can be rated by the Q factor as is shown in Chapter 5.4.3, Equation (10). It is found to be in the range of 400 to 2000.

The electrical energy generated in the resonant energy harvesting device is proportional to the electromagnetic damping. In order to maximize the electromagnetic conversion efficiency, the electromagnetic damping  $D_{em}$  has therefore to be increased, while the other damping losses need to be minimized. This can be achieved by using high quality factor materials for the cantilever and by tuning the design of the pick-up coil. As shown in Equation (25),  $D_{em}$  increases proportionately by the coil area and the number of turns. It is also strongly dependent on the magnetic field gradient. A large magnetic field gradient  $\delta B/\delta x$  is beneficial for a high electromagnetic conversion efficiency. The load resistance  $R_{load}$  is chosen to match the internal coil resistance, ensuring the highest power output according to the maximum power transfer theorem.

Taking into account these considerations, the following design parameters can be derived:

- temperature-dependent change of magnetization in the material ( $\Delta M/\Delta T$ ),
- structural and air damping losses,
- coil geometry (area and number of turns),
- external magnetic field gradient.

Therefore, a material has to be chosen which shows large changes of magnetization in small temperature differences. For the cantilever material, high quality factor materials are beneficial. Pick-up coils covering relatively large areas are advantageous because the electromagnetic damping increases without decreasing the resonance frequency to the same extent, as by increasing the number of coil turns. Finally, also the magnetic field gradient of the external magnet should be maximized to ensure a high overall conversion efficiency.

Table 7.4 shows the maximum temperature-dependent change of magnetization in the magnetic SMA materials used in this work as well as achievable values, found in literature. Also, the magnetic field gradient of the external magnet, implemented for the FSMA-based energy harvesting device using a magnetic heat source, and an optimized magnet geometry is denoted. It shows that further potential exists in tuning the magnetic design.

Table 7.4: Magnetization changes and magnetic field gradient used in this work and possibly achievable.

	1 <sup>st</sup> order transformation $\Delta M/\Delta T$	2 <sup>nd</sup> order transformation $\Delta M/\Delta T$	Magnetic field gradient
This work	3.17 emu·(g K) <sup>-1</sup>	2.33 emu·(g K) <sup>-1</sup>	0.23 T·mm <sup>-1</sup>
Possible	> 6 emu·(g K) <sup>-1</sup> [26]	~ 4 emu·(g K) <sup>-1</sup>	0.44 T·mm <sup>-1</sup> [103]

## 7.5. Design Parameters

For each operation principle, shown in Chapter 5 and Chapter 6, specific design parameters, which are described in detail above, can be adjusted individually, or are dependent on each other. Table 7.5 shows an overview of the parameters which can be tuned for each energy harvesting principle. The optimization of material properties is not mentioned here, as this would be beneficial for all operation principles.

Table 7.5: Overview on adjustable design parameters in the proposed energy harvesting operation principles. x: adjustable, o: dependent on other parameters, -: not applicable.

Operation principle	Geometry	Tip mass	Young's modulus	Ext. magnetic field	Heat transfer coeff.	Contact surface	Coil
FSMA external coil	x	x	o	x	x	x	x
FSMA microcoil	x	o	o	x	x	x	x
FSMA magnetic heat source	x	o	x	x	x	x	x
MSMA direct laser heating	x	-	-	x	x	x	x
MSMA ext. actuation	x	-	-	x	x	x	x
MSMA self-actuation	x	x	x	x	x	x	x
Pyroelectric	x	x	x	x	x	x	-



## 8. Comparison and Discussion

In this chapter, the results of the experiments, presented in Chapter 5 and Chapter 6, will be discussed and a comparison of the different energy harvesting techniques, investigated within this work, will be presented. The pyroelectric energy harvesting device with MSMA actuation will be excluded here, as it is not easily comparable with the other more similar magnetic SMA-based energy harvesting principles using an electromagnetic energy transducing mechanism.

### 8.1. Comparison of Energy Harvesting Principles

To compare the results of the presented energy harvesting principles, the main parameters and results are given in Table 8.1. All demonstrators are build up with a very similar overall size, as can be seen in the cantilever dimensions. They differ mainly in the cantilever material, and especially in the tip material and thickness.

Table 8.1: Comparison of the different energy harvesting principles, investigated in this work.

	FSMA external coil	FSMA microcoil	FSMA magnetic heat source	MSMA microcoil
Cantilever dimensions	2 x 4 mm <sup>2</sup>	2 x 4 mm <sup>2</sup>	3 x 5 mm <sup>2</sup>	2 x 4 mm <sup>2</sup>
Cantilever mater- ial, thickness	FSMA, 10 μm	FSMA, 5 μm	Brass, 10 μm	PI, 25 μm
Cantilever tip ma- terial, thickness	FSMA, 200 μm	-	FSMA, 5 μm	MSMA, 50 μm
Coil windings	1000	100	200	50
Therm. actuation frequency	up to 6 Hz	<b>82 - 125 Hz</b>	85 Hz	< 2 Hz
Mech. oscillation frequency	82 Hz	82 - 125 Hz	85 Hz	<b>200 Hz</b>
Power output	0.54 nW	0.12 μW	<b>2.4 μW</b>	0.12 nW
Power density	0.8 μW·cm <sup>-3</sup>	3 mW·cm <sup>-3</sup>	<b>&gt; 100 mW·cm<sup>-3</sup></b>	1.6 μW·cm <sup>-3</sup>

While the FSMA-based energy harvesting principle using an external coil, as well as the MSMA-based demonstrator have a quite large tip mass of FSMA or MSMA material, the other two principles have only a 5 μm thick active FSMA film, which is used for actuation. This difference in active material tip mass can be directly correlated to a large difference in thermal actuation frequencies. The low thermal actuation frequency of the MSMA demonstrator could additionally be explained by the lower thermal conductivity

of the PI cantilever, the use of a stack of MSMA films instead of bulk material, and the hysteresis due to first order phase transformation. While the two principles with relatively low thermal frequencies rely on frequency up-conversion, reaching oscillation frequencies of 80 to 200 Hz, the mechanical oscillations of the principles based on only 5  $\mu\text{m}$  thick active material match the increased thermal frequencies at above 80 Hz. This facilitates a much higher duty cycle close to 100%, resulting in power densities which are 3 to 5 orders of magnitude higher compared to the operating principles with a larger active material tip mass.

Another big difference between the principles presented in this work is the change from a stationary pick-up coil, situated around the moving cantilever, to a moving pick-up coil, mounted directly onto the moving cantilever front end. At first, this leads to a substantial decrease of coil windings because the size and mass of the coil are limited by the cantilever actuation capabilities. By using a much thinner copper wire this problem can be overcome and coils with up to 400 windings have been attached to the cantilever front end. The advantage of having the pick-up coil move in the large magnetic field gradient of the permanent magnet, compared to the moving FSMA tip with relatively low magnetization, leads to a considerable increase in electrical power output. Comparing the demonstrator with a magnetic heat source and the FSMA-based energy harvesting device using an integrated microcoil, shows that optimizing the magnetic field gradient by choosing the right magnet geometry leads to a further considerable increase of output power. Another advantage of the energy harvesting demonstrator design using a magnetic heat source is the independence of cantilever design and the amount of active material. Here, a non-magnetic metal is used as cantilever material and the FSMA film is mounted at the front end. Thereby, matching of the resonance frequency of the cantilever and the thermal frequency can be achieved, leading to an optimized system.

## 8.2. Discussion

The results of the presented magnetic SMA-based demonstrators show that it is possible to use the unique multifunctional properties of FSMA and MSMA materials to design novel thermal energy harvesting devices. By using the actuation capability and the magnetic properties of ferro- to paramagnetic transitions in FSMA or 1st order phase transformations in MSMA, new options are exploited to convert low grade waste heat to electricity on a miniature scale. The requirement for this energy conversion is a large change of magnetization  $\Delta M$  in small temperature differences  $\Delta T$ . However, reaching high magnetization changes by using a large amount of material, conflicts with short heat transfer times, which are needed in order to have high thermal frequencies and therefore a high power output. Therefore, at miniature scale, FSMA and MSMA thin films, with a large surface to volume ratio, pose a promising alternative to conventional

bulk material. Because of their low thermal mass and the large contact areas between active material and heat source, nearly instantaneous heating in few milliseconds can be achieved.

As there are mainly stationary heat sources available in the environment, it is crucial that energy harvesting concepts based on magnetic transitions show an intrinsic actuation to ensure fast periodic heating and cooling. This is achieved in the four principles presented by using the multifunctional properties of FSMA and MSMA materials. Different routes for energy conversion are shown, including direct conversion and external actuation with MSMA material, self-actuated frequency up-conversion, and matched resonant oscillation with large amplitudes and maximum duty cycle. A very efficient energy conversion is shown by using a pick-up coil moving through a magnetic field gradient at high velocities, exploiting the resonant mechanical actuation due to fast changes of magnetostatic attraction forces.

Looking at the results, it becomes clear that tailoring the material properties of the FSMA and MSMA material is crucial for further optimization and increased power output. Especially a large ratio of  $\Delta M/\Delta T$  is important to obtain competitive energy harvesting devices. On the other hand, the Curie temperature  $T_C$  has to be adapted to the desired application temperature range. It also becomes clear that besides the material also the design aspects need to be addressed in detail. This includes the geometry of the cantilever, the size of the pick-up coil, and the magnet, as explained in detail in Chapter 7.

### 8.3. Comparison with Thermoelectrics

To compare the presented energy harvesting principles with thermoelectric devices, it is not sufficient to just consider power density or efficiency figures because of the very different design. A fair comparison with thermoelectric generators (TEG) requires to take into account a similar size and similar temperature differences. Only microTEGs allow a high density of thermocouples and therefore noteworthy voltages at miniature size. An example for commercially available microTEGs are electroplated TEGs with sizes of  $4.4 \times 4.4 \times 0.5 \text{ mm}^3$  from GreenTEG [104] or sputter deposited TEGs with an overall size of  $3.3 \times 2.43 \times 1.1 \text{ mm}^3$  from micropelt [105]. For the sake of completeness, also a conventional bulk material based TEG is considered.

Besides the size of the TEG itself, also the size of the heat sink has to be taken into account. For a maximum efficiency and power output, the thermal resistance of the heat sink has to be matched to the thermal resistance of the TEG [48]. In order to do so, the microTEGs need heat sinks a hundred times larger than the actual TEG-area (200x to 500x) and thousand times larger than the active TEG-volume. To guarantee a fair comparison between the microTEGs and the energy harvester presented in this work, TEGs with a heat sink of a dimension of the actual TEG-size are considered.

Table 8.2 summarizes the data of the microTEGs and a representative bulk TEG. For evaluation of their actual power, a heat source temperature of 170 °C and an ambient temperature of 30 °C is considered, matching approximately the operational conditions of the FSMA-based energy harvesting device using a magnetic heat source. For the microTEGs two cases are investigated. For operation without any specially designed heat source, a natural convection heat transfer coefficient  $h$  of  $20 \text{ W}\cdot(\text{m}^2 \text{ K})^{-1}$  is assumed. By implementing an additional heat source of the area of the TEG, the heat transfer coefficient of  $80 \text{ W}\cdot(\text{m}^2 \text{ K})^{-1}$  is assumed. One has to keep in mind that such a heat source would increase the volume of the microTEG-based energy harvesting system substantially. For the bulk TEG a standard heat sink of  $25 \times 25 \text{ mm}^2$  size is assumed, having a matched thermal resistance of  $20 \text{ K}\cdot\text{W}^{-1}$ .

Table 8.2: Parameters of TEGs.

	micropelt DPG-655	greenTEG gSKIN	bulk TEG
Volume	$3.3 \times 2.43 \times 1.1 \text{ mm}^3$	$4.4 \times 4.4 \times 0.5 \text{ mm}^3$	$20 \times 20 \times 4 \text{ mm}^3$
Thermal resistance $\Theta_{TEG}$	$22 \text{ K}\cdot\text{W}^{-1}$	$18 \text{ K}\cdot\text{W}^{-1}$	$20 \text{ K}\cdot\text{W}^{-1}$
Electric resistance $R_{TEG}$	$210 \Omega$	$13 \Omega$	$11 \Omega$
Open circuit voltage $v_{OC}$	$80 \text{ mV}\cdot\text{K}^{-1}$	$4.3 \text{ mV}\cdot\text{K}^{-1}$	$28.6 \text{ mV}\cdot\text{K}^{-1}$

To evaluate the thermal resistances of the microTEG heat sinks, the area of the microTEGs  $A$  and the heat transfer coefficient are used:

$$\Theta_{sink} = \frac{1}{h \cdot A}. \quad (30)$$

Because of the difference of the thermal resistances of the microTEGs and the heat sinks, the temperature difference across the microTEGs  $\Delta T_{TEG}$  is only part of the overall temperature difference  $\Delta T$ , proportional to the ratio of thermal resistances:

$$\frac{\Delta T_{TEG}}{\Delta T} = \frac{\Theta_{TEG}}{\Theta_{sink} + \Theta_{TEG}}. \quad (31)$$

For the bulk TEG, the temperature difference is exactly 0.5, as the thermal resistance of the TEG and the heat sink are matched perfectly.

In order to calculate the electrical power, it is supposed that the load resistance matches the electric resistance of the microTEG. The voltage output is then half of the open circuit voltage due to the linear electric behavior of TEGs. Then, the power can be calculated as follows:

$$P = \frac{\left(\frac{v_{OC}}{2} \cdot \Delta T_{TEG}\right)^2}{R_{TEG}}. \quad (32)$$

The efficiency of the microTEG system is calculated by dividing the electrical power by the heat flux through the system:

$$\eta = \frac{P}{Q} = \frac{P}{\frac{\Delta T_{TEG}}{\theta_{TEG}}}. \quad (33)$$

For the bulk TEG, the formula of the efficiency at maximum electric power is used, which can also be found in [48]:

$$\eta_{mp} = \eta_C \cdot \frac{1}{2 + \frac{4}{ZT} - \frac{\eta_C}{4}}. \quad (34)$$

For the calculation of power density, only the volume of the active TEG material is used, which has a thickness of only 40  $\mu\text{m}$  in case of the microTEGs.

The results of the calculations are given in Table 8.3. It is important to note that the temperature difference achievable along the microTEGs is very small, even using a specially designed heat source with a high heat transfer coefficient of  $80 \text{ W}\cdot(\text{m}^2 \text{ K})^{-1}$ . Therefore, the resulting overall power output, power density, efficiencies of the microTEGs are small.

Table 8.3: Characterization of TEGs at an overall  $\Delta T = 140 \text{ K}$ , considering power, efficiency, and power density.

	micropelt, $h_{min}$	micropelt, $h_{max}$	greenTEG, $h_{min}$	greenTEG, $h_{max}$	Bulk TEG
$\theta_{sink}$	$6235 \text{ K}\cdot\text{W}^{-1}$	$1559 \text{ K}\cdot\text{W}^{-1}$	$2583 \text{ K}\cdot\text{W}^{-1}$	$646 \text{ K}\cdot\text{W}^{-1}$	$20 \text{ K}\cdot\text{W}^{-1}$
$\Delta T_{TEG}$	0.49 K	1.95 K	0.97 K	3.8 K	70 K
$P$	$1.83 \mu\text{W}$	$29 \mu\text{W}$	$0.34 \mu\text{W}$	$5.14 \mu\text{W}$	93.4 mW
$\eta$	0.0082%	0.032%	0.0006%	0.0024%	2.67%
$P/V$	$7.9 \text{ mW}\cdot\text{cm}^{-3}$	$125 \text{ mW}\cdot\text{cm}^{-3}$	$0.9 \text{ mW}\cdot\text{cm}^{-3}$	$13.3 \text{ mW}\cdot\text{cm}^{-3}$	$194 \text{ mW}\cdot\text{cm}^{-3}$

When comparing these numbers with the results on the magnetic SMA-based energy harvesting devices investigated in this work, most of the presented demonstrators cannot compete with the microTEG results, which have been developed and optimized over a long time. However, the FSMA-based energy harvesting device using a magnetic heat source already shows competitive results with an average electrical power of  $2.4 \mu\text{W}$  and a very high power density of up to  $118 \text{ mW}\cdot\text{cm}^{-3}$ , being on par with the best microTEG and almost reaching the power density of conventional bulk TEGs. The lack of need for additional heat sinking is also a key for the competitiveness of magnetic SMA-based energy harvesting devices. Heat is transferred only in a discrete and restricted manner, ensuring a sufficient temperature difference instead of steadily flowing through the TEG.

Therefore, a continuous optimization of the design and the material of magnetic SMA-based energy harvesting devices could lead to competitive alternatives to TEGs especially on miniature scale.



## 9. Conclusion and Outlook

This chapter concludes the thesis on energy harvesting with magnetic shape memory alloys (SMA) by a short summary and an outlook on further work, necessary to optimize and improve thermomagnetic energy harvesting demonstrators.

### 9.1. Conclusion

Making use of the multifunctional properties of magnetic SMA films, this work shows different approaches to generate electricity from a thermal gradient. Ferromagnetic and metamagnetic SMA (FSMA and MSMA) films are distinguished, as the basic material effects as well as the corresponding working principles are different.

For MSMA materials, the change of magnetization during a first order phase transformation is used, giving rise to large magnetization changes of up to  $3.17 \text{ emu}\cdot(\text{g K})^{-1}$ . However, first order phase transformations exhibit hysteresis and, thus, a considerable amount of latent heat that limits the actuation speed and efficiency. Nonetheless, a considerable improvement over state-of-the-art thermomagnetic energy harvesting by first order phase transformation is shown. A self-actuated MSMA energy harvesting demonstrator is build up consisting of elastic reset cantilever, MSMA tip, and microcoil which is attached to the front end. By moving between the heat source and a miniature magnet, the demonstrator shows a power density of  $1.6 \mu\text{W}\cdot\text{cm}^{-3}$  at a thermal operation frequency of 2 Hz.

FSMA-based energy harvesting devices, which use the ferro- to paramagnetic transition, a second order phase transformation, show also very promising results. Because of zero hysteresis and strong changes of magnetization of the investigated FSMA films in small temperature intervals of up to  $2.33 \text{ emu}\cdot(\text{g K})^{-1}$ , the ferro- to paramagnetic transition is very favorable for thermal energy harvesting.

The first demonstrator is based on an external pick-up coil, a FSMA cantilever, and a ferromagnetic tip of  $200 \mu\text{m}$  thickness, diving into the coil to induce an electric current. Because of relatively slow thermal actuation frequencies of about 2 Hz, frequency up-conversion is established to achieve oscillation frequencies of approximately 80 Hz, feasible for electromagnetic conversion. The power density of this demonstrator is measured to be about  $0.8 \mu\text{W}\cdot\text{cm}^{-3}$ .

A second generation demonstrator uses a microcoil, directly attached to the tip of the FSMA cantilever, omitting additional FSMA tip material. Because of the lower heat capacity of the FSMA film of just  $5 \mu\text{m}$  thickness, the thermal frequencies are improved more than tenfold to above 80 Hz. An electric current is generated by the coil moving in the magnetic field gradient of the external magnet. This second generation harvester is

able to generate an average electric power output of  $0.2 \mu\text{W}$ , resulting in a power density of approximately  $3 \text{ mW}\cdot\text{cm}^{-3}$ . The boost in power output is achieved by matching of thermal heat transfer times and oscillation behavior, leading to a resonant movement of the cantilever tip with an almost maximum mechanical duty cycle.

The third generation of FSMA-based energy harvesting demonstrators on the one hand combines the heat source with the external magnet to an integrated magnetic heat source, delivering a strong, almost spatially constant magnetic field gradient. This enables a higher electrical duty cycle. On the other hand, a brass cantilever of  $10 \mu\text{m}$  thickness is used in order to tune the eigenfrequency of the system independently from the magnetic attraction force and the heat transfer times, which are influenced by the amount of FSMA material on the tip. This setup allows for a resonant oscillation at approximately  $85 \text{ Hz}$  with large amplitudes of induced current of up to  $160 \mu\text{A}$ . The average power of the device is  $2.38 \mu\text{W}$ , at a heat source temperature of  $150 \text{ }^\circ\text{C}$ , resulting in an unprecedented large power density in thermomagnetic energy harvesting of  $118 \text{ mW}\cdot\text{cm}^{-3}$ . This challenges state of the art thermoelectrics on miniature scale.

Important design parameters are identified and discussed in detail for the developed MSMA and FSMA-based thermal energy harvesting devices. The design of an energy harvesting system comprises heat transfer, magnetic actuation forces, kinetic characteristics, and energy conversion. Many design parameters of these categories correlate strongly, making the optimization of the overall system a challenge. However, the most important design rule, identified in this work, is the matching of heat transfer times and mechanical oscillation. By implementing this concept, a new generation of miniature thermomagnetic energy harvesting devices can be developed, feasible for a broad range of thermal energy harvesting applications.

## 9.2. Outlook

Optimization of the presented energy harvesting devices by improving the different essential parameters, identified in this thesis, should be the topic of further studies. As mentioned above, many design parameters correlate and therefore a theoretical model should be developed for a detailed investigation of parameter space. In particular, the following steps have to be considered for optimization:

- tailoring of the temperature-dependent magnetization change  $\Delta M/\Delta T$ ,
  - at the ferro- to paramagnetic transition,
  - at zero hysteresis first order phase transformations,
- thermal contact optimization for decreasing heat transfer times,
- improving quality factor of cantilever oscillation to reduce structural damping,
- optimization of pick-up coil design (area, light-weight wire material like aluminum),
- providing a large magnetic field gradient by optimized magnet design.

By an in-depth research of ferromagnetic thin films with a high magnetization change in

a small temperature difference  $\Delta M/\Delta T$  and a Curie temperature  $T_C$  close or below 100 °C, new materials, better suitable for thermomagnetic energy harvesting, could be identified. Epitaxial films could provide favorable properties. A larger  $\Delta M/\Delta T$  leads to larger possible amplitudes, higher oscillation frequencies, and thereby higher induced voltages. By decreasing  $T_C$  [23] or  $T_0$ , the range of possible applications could be increased. When adjusting material properties, special attention should be paid to low functional fatigue. The goal of a long lifetime can be achieved by matching the lattice parameters of austenite and martensite such that  $\lambda_2 = 1$ . In addition, the cofactors of the transformation matrix should be close to zero [81]. This ensures a narrow hysteresis, favorable for thermomagnetic energy harvesting at small temperature differences.

The thermal contact has to be improved further by ensuring, e.g., a very flat contact surface [93], [106], [107]. The thermal contact is essential to provide short heat-transfer times, enabling high frequency thermal energy harvesting.

By improving the mechanical quality factor of the cantilever oscillation, a smaller change of temperature  $\Delta T$  is needed to overcome the damping, leading to shorter heat transfer times and improving the mechanical efficiency.

The optimization of the pick-up coil design by maximizing the coil area and increasing the number of coil windings leads to higher induced voltages and therefore a higher output power. However, the reduced eigenfrequency of a cantilever with larger tip mass due to the coil needs to be taken into account. This can be addressed by using aluminum based wires, having a much lower density than copper based wires, allowing for more lightweight coils on the cantilever tip. The fabrication of the coil also needs to be changed to an automatic process, e.g., by using wire bonding machines [108], or conventional winding methods, suited for miniature coil fabrication.

At last, the design of the magnetic field gradient is very important for large electro-mechanical efficiencies. Choosing an optimal magnet design, having a high internal flux and a large external magnetic field gradient in the actuation range of the cantilever, leads to an optimum electromagnetic conversion.

The above mentioned improvements will enable an even higher power output, making the thermomagnetic energy harvesting principle competitive to microTEG devices, especially in applications where only small space is available and batteries need to be avoided. In order to make use of the electricity generated by the harvester, also an electrical interface has to be developed. This should include a transformation of the generated voltage to above 1 V and charging of a capacitor or a battery to enable a continuous power supply for, e.g., a sensor node at a waste heat pipe.

For further development also a particular application has to be taken into account and the whole energy harvesting system has to be designed for the intended use. The assembly and fabrication for the thermomagnetic energy harvesting should be optimized as well regarding a competitiveness in costs.



## 10. Literature

1. D Miorandi, S Sicari, F De Pellegrini, I Chlamtac, "Internet of things: Vision, applications and research challenges" *Ad Hoc Networks* 10, 1497-1516 **(2012)**.
2. V Raghunathan, S Ganeriwal, M Srivastava, "Emerging techniques for long lived wireless sensor networks" *Communications Magazine, IEEE* 44, 108-114 **(2006)**.
3. JW Matiko, NJ Grabham, SP Beeby, MJ Tudor, "Review of the application of energy harvesting in buildings" *Measurement Science & Technology* 25 **(2014)**.
4. K Bhattacharya, RD James, "The Material is the Machine" *Science* 307, 53-54 **(2005)**.
5. K Ullakko, JK Huang, C Kantner, "Large magnetic-field-induced strains in Ni<sub>2</sub>MnGa single crystals" *Applied Physics Letters* 69, 1966-1968 **(1996)**.
6. P Müllner, VA Chernenko, G Kostorz, "Stress-induced twin rearrangement resulting in change of magnetization in a Ni-Mn-Ga ferromagnetic martensite" *Scripta Materialia* 49, 129-133 **(2003)**.
7. L Mañosa, D González-Alonso, A Planes, E Bonnot, M Barrio, J-L Tamarit, S Aksoy, M Acet, "Giant solid-state barocaloric effect in the NiMnIn magnetic shape-memory alloy" *Nature Materials* 9, 478-481 **(2010)**.
8. A Planes, L Mañosa, M Acet, "Magnetocaloric effect and its relation to shape-memory properties in ferromagnetic Heusler alloys" *Journal of Physics: Condensed Matter* 21, 233201 **(2009)**.
9. I Takeuchi, OO Famodu, JC Read, MA Aronova, KS Chang, C Craciunescu, SE Lofland, M Wuttig, FC Wellstood, L Knauss, A Orozco, "Identification of novel compositions of ferromagnetic shape-memory alloys using composition spreads" *Nature Materials* 2, 180-184 **(2003)**.
10. M Kohl, D Dittmann, E Quandt, B Winzek, S Miyazaki, DM Allen, "Shape memory microvalves based on thin films or rolled sheets" *Materials Science and Engineering A* 273-275, 784-788 **(1999)**.
11. D Brugger, M Kohl, B Krevet, "Ferromagnetic shape memory microscanner with large deflection angles" *International Journal of Applied Electromagnetics and Mechanics* 23, 99-105 **(2006)**.
12. M Kohl, E Just, W Pfleging, S Miyazaki, "SMA microgripper with integrated antagonism" *Sensors and Actuators A: Physical* 83, 208-213 **(2000)**.
13. M Kohl, M Gueltig, V Pinneker, R Yin, F Wendler, B Krevet, "Magnetic Shape Memory Microactuators" *Micromachines* 5, 1135-1160 **(2014)**.

10: Literature

14. T Grund, R Guerre, M Despont, M Kohl, "Transfer bonding technology for batch fabrication of SMA microactuators" *The European Physical Journal Special Topics* 158, 237-242 **(2008)**.
15. C Megnin, M Kohl, "Shape memory alloy microvalves for a fluidic control system" *Journal of Micromechanics and Microengineering* 24, 025001 **(2014)**.
16. WJ Buehler, JV Gilfrich, RC Wiley, "Effect of Low-Temperature Phase Changes on Mechanical Properties of Alloys near Composition TiNi" *Journal of Applied Physics* 34, 1475-1477 **(1963)**.
17. A Sozinov, N Lanska, A Soroka, W Zou, "12% magnetic field-induced strain in Ni-Mn-Ga-based non-modulated martensite" *Applied Physics Letters* 102, 021902 **(2013)**.
18. Z Zhang, RD James, S Müller, "Energy barriers and hysteresis in martensitic phase transformations" *Acta Materialia* 57, 4332-4352 **(2009)**.
19. H Ossmer, F Lambrecht, M Gültig, C Chluba, E Quandt, M Kohl, "Evolution of temperature profiles in TiNi films for elastocaloric cooling" *Acta Materialia* 81, 9-20 **(2014)**.
20. PJ Webster, KRA Ziebeck, Heusler Alloys in *Alloys and Compounds of d-Elements with Main Group Elements. Part 2* (Springer-Verlag, Berlin/Heidelberg), 75-79 **(1988)**.
21. O Heczko, "Magnetic shape memory effect and magnetization reversal" *Journal of Magnetism and Magnetic Materials* 290, 787-794 **(2005)**.
22. P Ranzieri, M Campanini, S Fabbri, L Nasi, F Casoli, R Cabassi, E Buffagni, V Grillo, C Magén, F Celegato, G Barrera, P Tiberto, F Albertini, "Achieving Giant Magnetically Induced Reorientation of Martensitic Variants in Magnetic Shape-Memory Ni-Mn-Ga Films by Microstructure Engineering" *Advanced Materials* 27, 4760-4766 **(2015)**.
23. VV Khovailo, VA Chernenko, AA Cherechukin, T Takagi, T Abe, "An efficient control of Curie temperature TC in Ni-Mn-Ga alloys" *Journal of Magnetism and Magnetic Materials* 272-276, 2067-2068 **(2004)**.
24. Y Sutou, Y Imano, N Koeda, T Omori, K Ishida, K Oikawa, R Kainuma, "Magnetic and martensitic transformations of NiMnX(X=In,Sn,Sb) ferromagnetic shape memory alloys" *Applied Physics Letters* 85, 4358-4360 **(2004)**.
25. V Srivastava, X Chen, RD James, "Hysteresis and unusual magnetic properties in the singular Heusler alloy Ni<sub>45</sub>Co<sub>5</sub>Mn<sub>40</sub>Sn<sub>10</sub>" *Applied Physics Letters* 97, 014101 **(2010)**.
26. R Kainuma, Y Imano, W Ito, Y Sutou, H Morito, S Okamoto, O Kitakami, K Oikawa, A Fujita, T Kanomata, K Ishida, "Magnetic-field-induced shape recovery by reverse phase transformation" *Nature* 439, 957-960 **(2006)**.

27. LB Kong, T Li, HH Hng, F Boey, T Zhang, S Li, Waste Thermal Energy Harvesting (II): Pyroelectric Effect and Others in *Waste Energy Harvesting* (Springer, Heidelberg), 405-480 **(2014)**.
28. SP Beeby, T O'Donnell, Electromagnetic Energy Harvesting in *Energy Harvesting Technologies* (Springer US, Boston, MA), 129-161 **(2009)**.
29. *Springer Handbook of Materials Measurement Methods*, H. Czichos, T. Saito, L. E. Smith, Eds. (Springer Science & Business Media, Heidelberg) **(2007)**.
30. JA Shaw, CB Churchill, MA Iadicola, "Tips and Tricks for Characterizing Shape Memory Alloy Wire: Part 1 - Differential Scanning Calorimetry and Basic Phenomena" *Experimental Techniques* 32, 55-62 **(2008)**.
31. M Ohtsuka, M Matsumoto, K Itagaki, "Effect of iron and cobalt addition on magnetic and shape memory properties of Ni<sub>2</sub>MnGa sputtered films" *Materials Science and Engineering A* 438-440, 935-939 **(2006)**.
32. M Ohtsuka, K Itagaki, "Effect of heat treatment on properties of Ni-Mn-Ga films prepared by a sputtering method" *International Journal of Applied Electromagnetics and Mechanics* 12, 49-59 **(2000)**.
33. E Makino, T Mitsuya, T Shibata, "Micromachining of TiNi shape memory thin film for fabrication of micropump" *Sensors and Actuators A: Physical* 79, 251-259 **(2000)**.
34. RJM Vullers, R van Schaijk, HJ Visser, J Penders, C Van Hoof, "Energy Harvesting for Autonomous Wireless Sensor Networks" *IEEE Solid-State Circuits Magazine* 2, 29-38 **(2010)**.
35. S Beeby, NM White, *Energy Harvesting for Autonomous Systems* (Artech House) **(2010)**.
36. A Toprak, O Tigli, "Piezoelectric energy harvesting: State-of-the-art and challenges" *Applied Physics Reviews* 1 **(2014)**.
37. C Cepnik, R Lausecker, U Wallrabe, "Review on Electrodynamic Energy Harvesters-A Classification Approach" *Micromachines* 4, 168-196 **(2013)**.
38. S Boisseau, G Despesse, BA Seddik, Electrostatic Conversion for Vibration Energy Harvesting in *Small-Scale Energy Harvesting* (InTech) **(2012)**.
39. G Zhu, B Peng, J Chen, Q Jing, ZL Wang, "Trieboelectric nanogenerators as a new energy technology: From fundamentals, devices, to applications" *Nano Energy* 14, 126-138 **(2015)**.
40. P Wang, X Dai, X Miao, X Zhao, J Liu, "A microelectroplated magnetic vibration energy scavenger for wireless sensor microsystems" *NEMS, 5th IEEE International Conference on Nano/Micro Engineered and Molecular Systems*, Xiamen, China, 383-386 **(2010)**.

10: Literature

41. L Tang, Y Yang, CK Soh, "Toward Broadband Vibration-based Energy Harvesting" *Journal of Intelligent Material Systems and Structures* 21, 1867-1897 **(2010)**.
42. I Suorsa, J Tellinen, K Ullakko, E Pagounis, "Voltage generation induced by mechanical straining in magnetic shape memory materials" *Journal of Applied Physics* 95, 8054 **(2004)**.
43. I Karaman, HE Karaca, "Energy harvesting using martensite variant reorientation mechanism in a NiMnGa magnetic shape memory alloy" *Applied Physics Letters* 90, 172505 **(2007)**.
44. M Kohl, R Yin, V Pinneker, Y Ezer, A Sozinov, "A Miniature Energy Harvesting Device Using Martensite Variant Reorientation" *Materials Science Forum* 738-739, 411-415 **(2013)**.
45. S Percy, C Knight, S McGarry, A Post, T Moore, K Cavanagh, "Thermal Energy Harvesting for Application at MEMS Scale" **(2014)**.
46. R Pelster, R Pieper, I Hüttl, "Thermospannungen - viel genutzt und fast immer falsch erklärt" *PhyDid A - Physik und Didaktik in Schule und Hochschule* 1, 10-22 **(2005)**.
47. GJ Snyder, Thermoelectric Energy Harvesting in *Energy Harvesting Technologies* (Springer, Boston, MA), 325-336 **(2009)**.
48. J Bierschenk, Optimized Thermoelectrics For Energy Harvesting Applications in *Energy Harvesting Technologies*, S. Priya, D. Inman, D. J. Inman, Eds. (Springer US, Boston, MA), 337-351 **(2009)**.
49. L-D Zhao, S-H Lo, Y Zhang, H Sun, G Tan, C Uher, C Wolverton, VP Dravid, MG Kanatzidis, "Ultralow thermal conductivity and high thermoelectric figure of merit in SnSe crystals" *Nature* 508, 373-377 **(2014)**.
50. J-F Li, W-S Liu, L-D Zhao, M Zhou, "High-performance nanostructured thermoelectric materials" *Npg Asia Materials* 2, 152-158 **(2010)**.
51. Gueltig, M, "Auslegung und Gestaltung eines organischen thermoelektrischen Generators mittels Siebdruck" Thesis, Karlsruhe Institute of Technology (KIT) **(2012)**.
52. Y Ta, *Action of radiations on pyroelectric crystals* (Compt. Rend) **(1938)**.
53. G Sebald, D Guyomar, A Agbossou, "On thermoelectric and pyroelectric energy harvesting" *Smart Materials and Structures* 18, 125006 **(2009)**.
54. T Huesgen, J Ruhhammer, G Biancuzzi, P Woias, "Detailed study of a micro heat engine for thermal energy harvesting" *Journal of Micromechanics and Microengineering* 20, 104004 **(2010)**.
55. SKT Ravindran, T Huesgen, M Kroener, P Woias, "A self-sustaining micro thermomechanic-pyroelectric generator" *Applied Physics Letters* 99, 104102 **(2011)**.

56. SKT Ravindran, M Kroener, P Woias, "A bimetallic micro heat engine for pyroelectric energy conversion" 47, 33-36 **(2012)**.
57. N Tesla, "Thermo Magnetic Motor" Patent **(1889)**.
58. L Brillouin, HP Iskenderian, "Thermodynamics of a Thermomagnetic Generator" *Physical Review* 75, 1325-1325 **(1949)**.
59. HE Stauss, "Efficiency of Thermomagnetic Generator" *Journal of Applied Physics* 30, 1622-1623 **(1959)**.
60. JF Elliott, "Thermomagnetic Generator" *Journal of Applied Physics* 30, 1774-1777 **(1959)**.
61. RE Rosensweig, "Theory of an improved thermomagnetic generator" *Electrical Engineers, Proceedings of the Institution of* 114, 405-409 **(1967)**.
62. SY Dan'kov, AM Tishin, VK Pecharsky, KA Gschneidner, "Magnetic phase transitions and the magnetothermal properties of gadolinium" *Physical Review B* 57, 3478-3490 **(1998)**.
63. LD Kirol, JI Mills, "Numerical analysis of thermomagnetic generators" *Journal of Applied Physics* 56, 824-828 **(1984)**.
64. D Solomon, "Improving the Performance of a Thermomagnetic Generator by Cycling the Magnetic-Field" *Journal of Applied Physics* 63, 915-921 **(1988)**.
65. A Karle, "The thermomagnetic Curie-motor for the conversion of heat into mechanical energy" *International journal of thermal sciences* **(2001)**.
66. CS Alves, FC Colman, GL Foleiss, GTF Vieira, W Szpak, "Numerical simulation and design of a thermomagnetic motor" *Applied Thermal Engineering* 61, 616-622 **(2013)**.
67. LDR Ferreira, CVX Bessa, I da Silva, S Gama, "A heat transfer study aiming optimization of magnetic heat exchangers of thermomagnetic motors" *International Journal of Refrigeration* 37, 209-214 **(2014)**.
68. M Trapanese, G Cipriani, V Di Dio, V Franzitta, A Viola, "Optimization of a thermomagnetic motor" *Journal of Applied Physics* 117, 17A750 **(2015)**.
69. AG Kvirikadze, MD Zviadadze, VA Barnov, GG Kiknadze, LA Zamtaradze, "The Efficiency of Ideal Thermomagnetic Engine" *arXiv.org* **(2012)**.
70. M Ujihara, GP Carman, DG Lee, "Thermal energy harvesting device using ferromagnetic materials" *Applied Physics Letters* 91, 093508 **(2007)**.
71. M Ujihara, DG Lee, GP Carman, "Energy harvesting by means of thermo-mechanical device utilizing bistable ferromagnets" Patent **(2010)**.
72. KE Bulgrin, YS Ju, GP Carman, AS Lavine, "A Coupled Thermal and Mechanical Model of a Thermal Energy Harvesting Device" *ASME 2009 Idots* , 327-335 **(2009)**.
73. C-J Hsu, SM Sandoval, KP Wetzlar, GP Carman, "Thermomagnetic conversion efficiencies for ferromagnetic materials" *Journal of Applied Physics* 110 **(2011)**.

74. SM Sandoval, AE Sepulveda, SM Keller, "On the thermodynamic efficiency of a nickel-based multiferroic thermomagnetic generator: From bulk to atomic scale" *Journal of Applied Physics* 117, 163920 **(2015)**.
75. L Zhou, Y Xuan, Q Li, W Lian, "A new miniaturized engine based on thermomagnetic effect of magnetic fluids" *Frontiers of Energy and Power Engineering in China* 3, 160-166 **(2009)**.
76. KB Joshi, S Priya, "Multi-physics model of a thermo-magnetic energy harvester" *Smart Materials and Structures* 22 **(2013)**.
77. T-K Chung, U Shukla, C-Y Tseng, C-C Chen, C-M Wang, "A magnetic/piezoelectric-based thermal energy harvester" *SPIE Smart Idots* , 86880M **(2013)**.
78. C-C Chen, T-K Chung, C-C Cheng, C-Y Tseng, "A novel miniature thermomagnetic energy harvester" *SPIE Smart Structures and Materials + Nondestructive Evaluation and Health Monitoring* 9057, 90570X **(2014)**.
79. RD James, Z Zhang, A Way to Search for Multiferroic Materials with "Unlikely" Combinations of Physical Properties in *Magnetism and Structure in Functional Materials* (Springer, Berlin, Heidelberg), 159-175 **(2005)**.
80. R Zarnetta, R Takahashi, ML Young, A Savan, Y Furuya, S Thienhaus, B Maaß, M Rahim, J Frenzel, H Brunken, YS Chu, V Srivastava, RD James, I Takeuchi, G Eggeler, A Ludwig, "Identification of Quaternary Shape Memory Alloys with Near-Zero Thermal Hysteresis and Unprecedented Functional Stability" *Advanced Functional Materials* 20, 1917-1923 **(2010)**.
81. C Chluba, W Ge, RL de Miranda, J Strobel, L Kienle, E Quandt, M Wuttig, "Ultralow-fatigue shape memory alloy films" *Science* 348, 1004-1007 **(2015)**.
82. V Srivastava, Y Song, K Bhatti, RD James, "The Direct Conversion of Heat to Electricity Using Multiferroic Alloys" *Advanced Energy Materials* 1, 97-104 **(2011)**.
83. Y Song, KP Bhatti, V Srivastava, C Leighton, RD James, "Thermodynamics of energy conversion via first order phase transformation in low hysteresis magnetic materials" *Energy & Environmental Science* 6, 1315 **(2013)**.
84. A Post, C Knight, E Kisi, "Thermomagnetic energy harvesting with first order phase change materials" *Journal of Applied Physics* 114, 033915 **(2013)**.
85. M Kohl, D Brugger, M Ohtsuka, T Takagi, "A novel actuation mechanism on the basis of ferromagnetic SMA thin films" *Sensors and Actuators A: Physical* 114, 445-450 **(2004)**.
86. D Brugger, M Kohl, U Hollenbach, A Kapp, C Stiller, "Ferromagnetic shape memory microscanner system for automotive applications" *International Journal of Applied Electromagnetics and Mechanics* 23, 107-112 **(2006)**.

87. M Gueltig, M Ohtsuka, H Miki, T Takagi, M Kohl, "Thermal energy harvesting by high frequency actuation of magnetic shape memory alloy films" *TRANSDUCERS 2015 - 18th International Solid-State Sensors, Actuators and Microsystems Conference*, Anchorage, Alaska, USA, 718-721 **(2015)**.
88. K Oikawa, W Ito, Y Imano, Y Sutou, R Kainuma, K Ishida, H Okada, O Kitakami, T Kanomata, "Effect of magnetic field on martensitic transition of Ni<sub>46</sub>Mn<sub>41</sub>In<sub>13</sub> Heusler alloy" *Applied Physics Letters* 88, 122507 **(2006)**.
89. S Aksoy, M Acet, PP Deen, L Mañosa, A Planes, "Magnetic correlations in martensitic Ni-Mn-based Heusler shape-memory alloys: Neutron polarization analysis" *Physical Review B* 79, 212401 **(2009)**.
90. M Gueltig, H Ossmer, M Ohtsuka, H Miki, K Tsuchiya, T Takagi, M Kohl, "High Frequency Thermal Energy Harvesting Using Magnetic Shape Memory Films" *Advanced Energy Materials* 4, 1400751 **(2014)**.
91. M Gueltig, B Haefner, M Ohtsuka, M Kohl, "Thermal energy harvesting based on ferromagnetic shape memory alloy microactuation" *Transducers & Eurosensors XXVII*, Barcelona, Spain, 2803-2806 **(2013)**.
92. M Gueltig, M Ohtsuka, H Miki, "Thermomagnetic Actuation by Low Hysteresis Metamagnetic Ni-Co-Mn-In Films" *Materials Today: Proceedings* 2, S883-S886 **(2015)**.
93. B Gotsmann, MA Lantz, "Quantized thermal transport across contacts of rough surfaces" *Nature Materials* 12, 59-65 **(2012)**.
94. LS Fletcher, "Recent Developments in Contact Conductance Heat-Transfer" *Journal of Heat Transfer-Transactions of the Asme* 110, 1059-1070 **(1988)**.
95. MA Bidakhvidi, R Shirzadeh, S Vanlanduit, "Study of the Cooling Performance of Oscillating Piezoelectric Fans" *Proceedings of the ASME International Mechanical Engineering Conference and Exposition IMECE 2013*, San Diego, California, USA, **(2013)**.
96. M Kimber, SV Garimella, A Raman, "Local Heat Transfer Coefficients Induced by Piezoelectrically Actuated Vibrating Cantilevers" *Journal of Heat Transfer* 129, 1168-1110 **(2007)**.
97. SF Sufian, MZ Abdullah, MK Abdullah, JJ Mohamed, "Effect of Side and Tip Gaps of a Piezoelectric Fan on Microelectronic Cooling" *IEEE Transactions on Components, Packaging and Manufacturing Technology* 3, 1545-1553 **(2013)**.
98. A Engel, R Friedrichs, "On the electromagnetic force on a polarizable body" *American Journal of Physics* 70, 428-432 **(2002)**.
99. D Brugger, "Miniatur-Laserscanner für mobile Anwendungen" Thesis, Forschungszentrum Karlsruhe **(2006)**.
100. *Brass foil Datasheet* (Goodfellows) **(2016)**.
101. *Kapton HN polyimide film Datasheet* (DuPont) **(2011)**.

10: Literature

102. SM Sandoval, "On the thermodynamic efficiency of a multiferroic thermomagnetic generator: From bulk to atomic scale" Thesis, UCLA **(2014)**.
103. *Q02x02x10EP-N35 Datasheet* (HKCM Engineering) **(2016)**.
104. *gSKIN Heat-Flux-Sensors for R&D Datasheet* (greenTEG AG) **(2015)**.
105. *MPG-D655 Thin-film Thermogenerator Chip Datasheet* (Micropelt GmbH) **(2012)**.
106. M Bahrami, MM Yovanovich, JR Culham, "Thermal contact resistance at low contact pressure: Effect of elastic deformation" *International Journal of Heat and Mass Transfer* 48, 3284-3293 **(2005)**.
107. MG Cooper, BB Mikic, MM Yovanovich, "Thermal contact conductance" *International Journal of Heat and Mass Transfer* 12, 279-300 **(1969)**.
108. K Kratt, V Badilita, T Burger, JG Korvink, U Wallrabe, "A fully MEMS-compatible process for 3D high aspect ratio micro coils obtained with an automatic wire bonder" *Journal of Micromechanics and Microengineering* 20, 015021 **(2010)**.



# 11. Curriculum Vitae

## Personal Information:

Name: Marcel Gültig  
Nationality: German



## Contact Information:

E-mail: marcel.gueltig@kit.edu

## Education:

3/2012 - 5/2016: *PhD*, Faculty of Mechanical Engineering  
Karlsruhe Institute of Technology (KIT), Germany

10/2007 - 2/2012: *Dipl.-Ing.* in Mechanical Engineering,  
Mechatronics and Microsystem Technology,  
Karlsruhe Institute of Technology (KIT), Germany

Research project (2010): Development of an intelligent drinking assistance, helping elderly people to monitor their drinking behavior  
Participant of the international student competition *iCan* in Beijing, China in 2011 (*3rd prize*)

Diploma Thesis (2012): Development and realization of a thermoelectric generator based on screen printing (*patented*)

## Professional Experience:

3/2012 - 3/2016: *Phd Researcher*  
Institute of Microstructure Technology (IMT),  
Karlsruhe Institute of Technology (KIT), Germany



---

I declare that I have developed and written the enclosed thesis completely by myself, and have not used sources or means without declaration in the text.

**Karlsruhe 16.11.16**

---

Marcel Gültig